THE UNIVERSITY OF CHICAGO

UNDERSTANDING THE ROLE OF MOLECULAR ORDER AND MICROSTRUCTURE OF DOPED SEMICONDUCTING POLYMERS ON CHARGE TRANSPORT

A DISSERTATION SUBMITTED TO

THE FACULTY OF THE DIVISION OF THE PHYSICAL SCIENCES

IN CANDIDACY FOR THE DEGREE OF

DOCTOR OF PHILOSOPHY

DEPARTMENT OF PHYSICS

BY

MARK FEUER DITUSA

CHICAGO, ILLINOIS

JUNE 2022

To my wife and family, without whose tireless encouragement I wouldn’t still be fighting

Contents

List of Tables

List of Figures

Acknowledgements

I know that more than most people, I tend to wear my struggles on my sleeve. Graduate school brought out my insecurities and my immaturities, and it was very often not pretty. Despite that, I've been lucky throughout graduate school to have many patient people who have helped me confront my flaws and grow into the man I am today.

First and foremost, it starts with Shrayesh Patel. I do not believe I would have survived without his constant guidance and encouragement. As a mentor, one of his best qualities is understanding how to best motivate each student. His empathy coupled with an expectation for excellence has truly pushed me to be the best researcher I can be. It has not gone unnoticed, too, that he goes out of his way to make sure that his door, both physical and metaphorical, is always open to discuss whatever is on your mind. He has made himself the perfect professional and personal mentor during my time in his lab. I just hope I have made him proud.

I don't know where either I or the Patel Lab would be without Garrett Grocke. That is not hyperbole. In a very material way, Garrett put together and designed many of the instruments and stations that make up the Patel laboratory space, and this dissertation would literally have not happened without his work. On top of this, Garrett is intimately knowledgeable with the projects of everyone going on in the Patel lab and has been a great scientific resource when something just isn't making sense. But most of all, Garrett has been the emotional support for the whole of the Patel lab. I can't count the number of times I've gone to him for advice on how to pick through my feelings, and he does the same for anyone that asks. Garrett, you've been an amazing coworker and friend, and I'm so thankful that I could be your friend, too.

I want to also thank all the wonderful people that are a part of the Patel lab. Tengzhou's straight man to my funny man made the workdays bearable. Zhongyang's patience and teaching has been

invaluable. Peter's deep insight has pushed me scientifically. Nick's and Hongyi's work ethic never cease to amaze me. Sam's inquiring mind and knowledge of his field inspires me to want to know more. Andrea, Mincheol, and Jie-Hao, you all make me excited for the future of the Patel group, and I can't wait to see how things grow with your input. You all have been close friends, and all of you at one point or another has had to deal with whatever insanity was coming from my corner of the office, and for that I am infinitely grateful.

For my close-knit group of friends whose encouragement and friendship has kept me going, I am also supremely thankful. Kyle and Matt, you were two of the best friends and roommates I could have asked for. Without your teaching, help, and encouragement, I wouldn't have made it past candidacy. D&D with y'all and Jody, Chih-Kai, and Nick has given me life. I know we'll stay in touch.

Finally, I am having trouble putting into words how thankful I am for my family, which I'll freely admit is something I don't do enough. To my sisters, Chloe and Rebecca, your strength to fight through adversity and your intelligence to thrive in whatever you do inspires me daily. I love you. Mom and Dad, your advice and care have kept me going, and you both do so much to make sure I can succeed. I love you. For my wife, Qi Li, I am grateful that I found you. You have pushed me to grow and be the best boyfriend, husband, and person I can be, and your support and love has kept me going in my darkest moments. I love you. I can't wait to see what our life together will be.

Abstract

Molecular doping is a method used to increase the charge carrier concentration within organic semiconductors to increase their conductivity. In an analogue to atomistic doping of inorganic semiconductors, in which an atom of the host material is replaced by an atom with one more or one fewer electron, molecular doping introduces larger molecules that react with the semiconducting backbone, typically by a redox reaction, which either introduces a hole or electron into the semiconducting system. A large class of organic semiconductors are conjugated polymers, which self-assemble into aggregate domains of higher order, where charge carriers can more easily hop interchain in their journey across the material. However, the analogue to atomistic doping breaks when considering the frequency of impurities: for efficient introduction of charge carriers, impurities are added in a ratio on the order of 10^{-3} to 10^{-6} to the host material, whereas molecular dopants, and hence impurities, are typically introduced on the order of 10^{-1}. This high frequency of impurities threatens to disrupt features that lead to high mobility of charge carriers, such as polymer "tie" chains that connect domains of high mobility through domains of low mobility. There are methods that can minimize the damage of dopant to the underlying structure, such as the method of dopant introduction, as well as optimizing the amount of dopant to increase charge concentration without overwhelming the polymer with impurities.

In Chapter 2, we study one such method of dopant introduction, vapor sequential doping, and how it introduces charge carriers while impacting the conjugated polymer structure, for the archetypical polymer-dopant pairing of poly(3-hexylthiophene-2,5-diyl) (P3HT) and 2,3,5,6-tetrafluoro-7,7,8,8-tetracyanoquinodimethane (F4TCNQ). We find that the aggregate domains of polymer are doped first and are responsible for the rapid rise in conductivity over six orders of magnitude, whereas the less mobile amorphous domains are doped second, and only increase the

conductivity within an order of magnitude. In chapter 3, we investigate using weaker dopants with a similar chemical structure to F4TCNQ, and how changing the dopant strength changes the interplay between polymer structure and the vapor doping process. We find that the dopant strength in relation to the electron affinity of the aggregate and amorphous domains of the polymer determines whether the dopant is capable of effectively doping that domain, with our weakest dopant (TCNQ) not able to effectively dope either domain. Chapter 4 details a study using poly(3-(methoxyethoxyethoxymethyl)thiophene, which has the same backbone as P3HT but polar sidechains that allow for the solvation of ions for ionic transport. Using thermal treatments identified from the differential scanning calorimetry of this material, we see that we are able to control the local and long-range order both by the thermal treatment of the film as well as the addition of LiTFSI salt. Due to this material's promise as a dual ionic and electronic conductor, we find that for this material that the best ionic and electronic conduction comes when the material is annealed just below its aggregate domain melting transition, leading to the largest aggregate domains with good alignment between the domains.

Chapter 1: Introduction

1.1 Application of polymer semiconductors

Semiconductors are the fundamental building block of modern electronics. Their usage powers all kinds of devices that we are used to using day to day, notably computing, digital memory, light emitting diodes (LEDs), and photovoltaics. Their connection to computing power leads to packing more and more as densely as possible on microprocessors, and famously the rate of this density increase is referred to as Moore's law. Electrical conductivity is defined as a material's ability to conduct an electrical current and is linearly proportional to the material's concentration of charge carriers (n) and the ease at which a charge carrier can move throughout the material, or mobility (μ). Semiconductors are defined as materials with an energy gap between states filled by electrons (the valence band) and those without (the conduction band), known as a band gap, that isn't too wide. Another way to define the bandgap is the difference between the state with the highest energy that has electrons is known as the highest occupied molecular orbital, or HOMO, and the state with the lowest energy without electrons is known as the lowest unoccupied molecular orbital, or LUMO. Metals have a bandgap in metals is so small that ambient energy at room temperature can bridge the gap, whereas insulators have a width is too large to easily overcome for charge transport (typically defined as 3 to 4 eV).[1,2]

Most transistors are made from inorganic materials, such as silicon and gallium arsenide, which have defined the market since the first truly mass-producible and compact transistor was invented in 1959. However, despite the longevity of their dominance, there remains some challenges for inorganic transistors that appear inherent to the technology. Firstly, they remain energy-intensive to produce, requiring high temperatures, which makes them less attractive for large-area

applications that desire low cost. Secondly, the ability to tune their band gaps for displays and lighting remains difficult.[3]

Organic semiconductors offer solutions to these inorganic shortcomings, along with adding a whole host of other beneficial properties. The synthesis methods of organic materials already allows for chemical tailoring of properties, leading to optimization of electronic properties such as the band gap and charge carrier mobility, as well as properties aiding ease of processing and viability of commercial use such as their solubility, toxicity, and biocompatibility.[4–7] Organic semiconductors also can exhibit properties that inorganic semiconductors cannot, notably their mechanical flexibility, their relative light weight, and the ability to be processed at low temperatures and at high throughput.[8] Briefly, let's touch on some of the applications that organic semiconductors have been developed for.

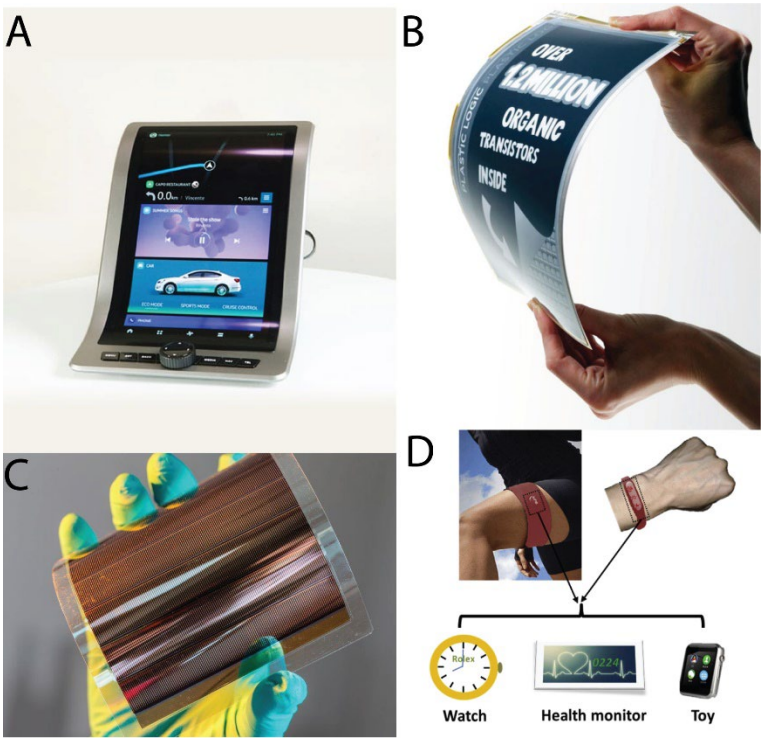

Figure 1. Examples of applications of organic semiconductors.
(A) A mockup of a flexible OLED display within a car by Samsung, 2020.[9] (B) Flexible screen driven by a matrix of 1.2 million organic field effect transistors on a OTFT.[10] (C) An organic solar

(Figure 1. Examples of applications continued) cell module with six interconnected solar cells, developed by Fraunhofer.[11] (D) An illustration of potential applications of organic thermoelectrics, including a heat-harvesting watch, health monitors, and toys.[12]

1.1.1 Organic light-emitting diodes (OLEDs)

Light-emitting diodes (LEDs) are semiconductor light sources that emit light when a current is flowed through it. This light comes from when electrons in the semiconductor recombine with holes and release photons, and the color of the light corresponds to the band gap width.[13] LEDs are often used for electronic displays, and are ideal for portable applications due to their low power consumption that results in high brightness. OLEDs are an attractive target due to the potential for plastic-based flexible displays that are lighter and more durable than conventional displays.[8] OLEDs have already established themselves as a viable technology, appearing in contemporary smart phones and televisions.[14]

1.1.2 Organic thin-film transistors

Thin-film transistors (TFT) are a particular type of transistor where the transistor is thin relative to the plane of the device, and is grown on a supporting and non-conducting substrate, such as glass.[15] The traditional use of the TFT is in liquid-crystal displays, where a separate transistor is used for each pixel on the display, allowing for fast refreshing of pixels on the display with reduced cross-talk between pixels. Traditionally, TFTs have been made from amorphous or polycrystalline silicon, but there are advantages that making TFTs out of organic semiconductors (OTFTs) would give. Utilizing OTFTs as the back-plane material for OLEDs, displays can be created with low-cost and high-throughput printing-based manufacturing that would enable flexible, or even stretchable, displays, sensors, and other electronics.[16–18]

1.1.3 Organic photovoltaics

Photovoltaics is the conversion of photons (light) into electricity in semiconductors. This is just the reverse process seen in OLEDs, which turn electricity into light. Photovoltaic materials are commonly seen commercially within solar panels, which quite literally take sunlight and turn it into electricity for use elsewhere in the electric grid. Although organic photovoltaics were among the first applications thought of for polymer materials exhibiting metallic electrical transport in 1977, silicon photovoltaics have become very cheap in the intervening years, making development of organic photovoltaics for commercial use difficult.[19] There are also difficulties in reaching the efficiency and lifetime of silicon-based photovoltaics. Regardless, there remain excitement towards organic solar cells utilizing organic semiconductors, due to their light weight, flexibility, and transparency.[20]

1.1.4 Organic thermoelectrics

Instead of operating with light to electricity or vice-versa, thermoelectrics operate with the Seebeck effect, which relates how heat can generate electricity (or vice-versa). In specific, a conductor or semiconductor exposed to a temperature gradient accumulates charge carriers via the diffusion from the hot to cold end being balanced by an internal electric field, which results in a potential difference over the material. The relation between the voltage difference generated by the temperature gradient for a specific material is known as its Seebeck coefficient (α). In practical terms, thermoelectrics provide a way to harvest waste heat for electricity, or to use electricity to cool or heat. The current state-of-the art thermoelectrics utilize inorganic materials, such as bismuth telluride, which are highly toxic and expensive to make, and are thus relegated to highly niche uses (such as scientific equipment in our own lab).[21] Like the other organic semiconducting technologies, organic thermoelectrics hope to make use of some of the benchmarks of organic materials: abundant, cheap to process, flexible, biocompatible, and tunable.[21,22] In particular, our

own lab has used the tunability of organic semiconductors to make materials with a gradient in α to increase the efficiency of organic thermoelectrics for power generation.[23]

1.2 Conjugated Polymers

1.2.1 Conjugation

Conjugated systems are a class of organic materials characterized by a molecular structure alternating between single and double bonds.[25] To understand how conjugated systems lead to mobile charge carriers travelling down a conjugated backbone, we need to take a brief diversion into molecular orbital theory. Orbitals are a representation of where electrons have a high probability of being, and when drawn as a 3D shape, the bounds of the shape are typically a representation of a surface of equal probability (*e.g.* there is a 1% chance the electron would be on the shape's surface) and everything within this shape is more probable. Single bonds between two different atoms are made up of a single σ bond, whereas double bonds are made up of a σ and a π bond. The orbital for a π bond is a linear combination of the "$p_{\perp}$" atomic orbitals, which look like dumbbells that are perpendicular to the internuclear axis between the two bonded atoms (see **Figure 2** for a representation**)**. In conjugated systems, more than one $p_{\perp}$ can overlap, leading to delocalization of the electrons within the *p* orbitals. **Figure 2** shows a Benzene molecule, which has six *p* orbitals that combine to allow delocalization of the electrons above and below the plane of the aromatic ring.

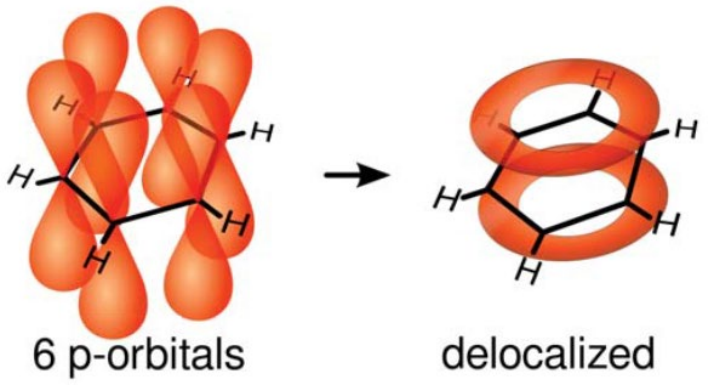

Figure 2. Benzene as an example of a conjugated molecule.
Reproduced from Vladsinger with license CC BY-NC-SA 3.0.

1.2.2 Conjugated polymers are semiconductors

Conjugated polymers are molecules with conjugated systems on their backbones. When this conjugated system is maintained over the course of a polymer backbone, electrons can be delocalized over the whole backbone, given that there is good overlap between *p* orbitals of neighboring atoms. In other words, conjugated polymers provide a high charge carrier mobility throughout their backbone.

There are many polymer chemistries that provide a conjugated system, and thus a wide catalog of conjugated polymers. A small sample of these building blocks and some examples relevant to the content to this dissertation can be seen within **Figure 3**.

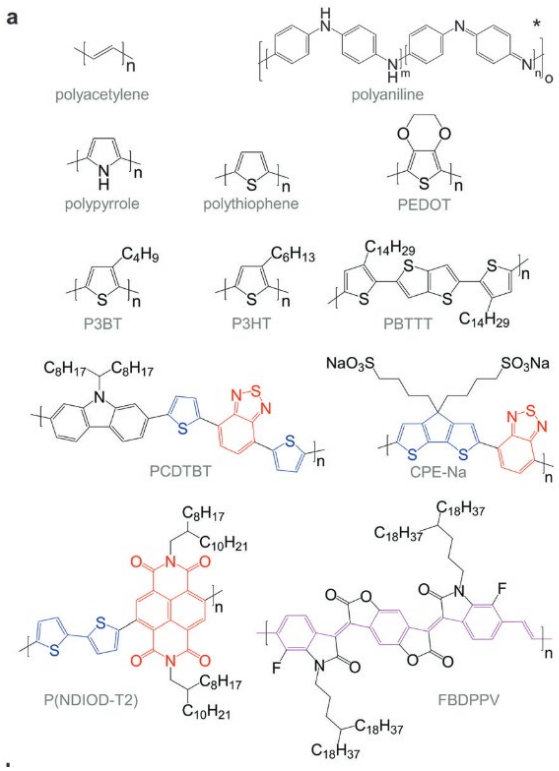

Figure 3. Chemical structure of conjugated polymers.
Reproduced from Kroon *et al.*[21]

A double bond creates both a π bonding orbital and a π* anti-bonding orbital. The π-orbital contains two electrons, and the π*-orbital is empty. The energy gap between these two orbitals is fundamentally a bandgap. As conjugated monomers are lengthened into oligomers and finally polymers, orbital interactions between the constituent atoms lead to an energy level splitting of the π- and π*-orbitals, as seen within **Figure 4**. From the π orbitals, the valence band emerges, topped by the highest occupied molecular orbital, and from the π* orbitals come the conduction band, bordered by the lowest unoccupied molecular orbital.[21]

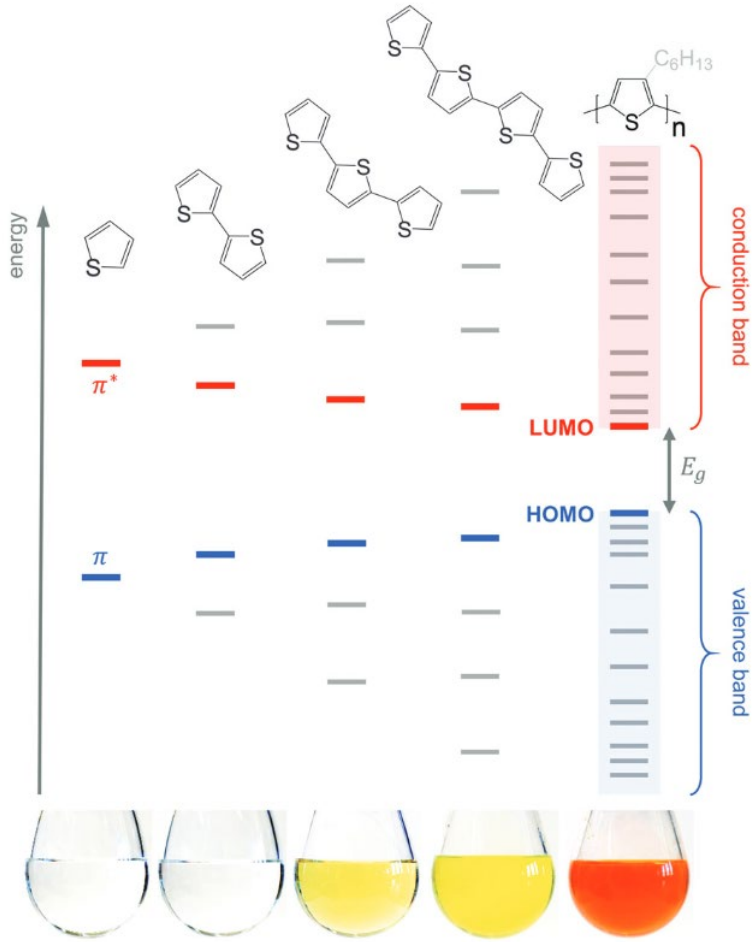

Figure 4. Evolution of the bandgap as the repeat unit number increases.
This image is made with the conjugated unit thiophene in mind, and as the number of repeat units increases, the band gap closes. This is illustrated by the red-shift in absorption of a polythiophene (P3HT) in chloroform. Reproduced from Kroon *et al.*[21]

1.3 Conjugated polymer structure and its relation to conduction

There is a strong connection between the microstructure of the polymer and the polymer material's electrical performance. Conjugated polymers, themselves, sit in an uneasy middle area between crystalline and amorphous materials. They feature a sequence of repeat units that, in theory, can order. For conjugated polymers with a rigid backbone and high molecular weight, which this dissertation focuses on, the microstructure exhibits continuous variation in its order

parameters, switching between semi-ordered aggregate domains and the amorphous, "spaghetti-like" regions that surround them. In the language that we have used so far in this dissertation, the bandgap within the aggregate domains is lessened due to the electron delocalization across adjacent chain segments, and thus the majority of charge transport occurs within the aggregate domains.

Aggregate domains can be described as lamellae of co-facial stacks of polymer segments, which form due to strong π-orbital overlap between neighboring chains. Again returning to our understanding of orbitals as where electrons are most likely to be, these π-orbital overlaps allow for the transfer of charge carriers such as electrons or holes (the lack of electrons) interchain. This phenomenon is called π-π stacking, and the π-π stacking distance is key to providing fast interchain charge transport; any decrease of this distance leads to significant improvements in mobility. Amorphous domains lack this π-π stacking, and hence have poor interchain charge carrier mobility. Therefore, any ability to connect aggregate domains together would allow for efficient transport of a charge carrier throughout the material. This concept is known as a tie chain, which is a single polymer backbone that participates within multiple aggregate domains, and therefore can efficiently bridge the amorphous domains and permit efficient transport of charge carriers over hundreds of microns of a material, rather than just the tens of nanometers of a single aggregate domain.[26] This tie chain phenomenon only occurs if there are chains that are long enough to participate in multiple aggregate domains, and thus molecular weight of the polymer becomes an important parameter. Molecular weight, in general, shows a strong increase in charge carrier mobility, but reaches a plateau; for poly(3-hexylthiophene-2,5-diyl) (P3HT), this crossover in behavior occurs around 25 kg mol^{-1}.[27]

The focus so far for this section has been on local order, or order on the scale of a few chains making up an amorphous or aggregate domain. However, we must also consider the orientation of multiple aggregate domains over the length of the material. Polymer aggregates can be randomly oriented with respect to the orientation of the conjugated backbone, or they can display a tendency or preference. This preference tends to be represented by the relation of the orientation of the polymer backbones in the aggregates to the substrate, whether it's parallel (face-on), perpendicular (edge-on), or somewhere in between (**Figure 5**). Due to interchain transport favorably conducting in the direction of the π-π stacking, the mobility of charge carriers in-plane and out-of-plane is anisotropic. This is relevant for devices that need to transport charge carriers in a specific direction, such as a solar cell. A preferential face-on orientation is preferred in this case, due to a need to transport generated charge carriers in the out-of-plane direction.[28]

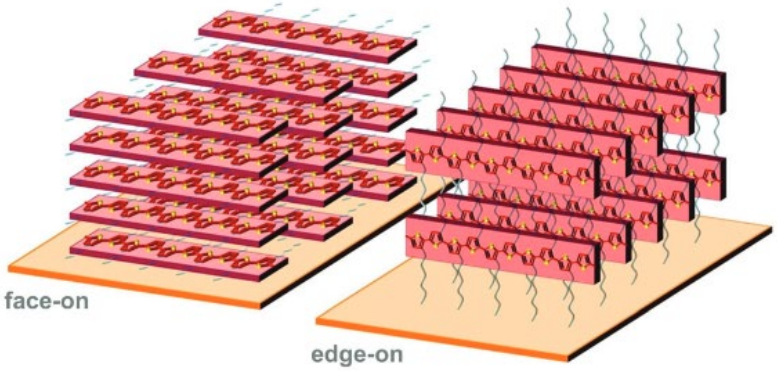

Figure 5. Face-on and edge-on orientation for P3HT aggregates.
The π-π stacking direction lying out-of-plane (face-on) or in-plane (edge-on). Reproduced from Kroon *et al*.[21]

1.4 Molecular doping of conjugated polymers

1.4.1 Doping of inorganic and organic materials

Doping is a technique that aims to increase the charge carrier concentration of a material to make the material more conductive. This technique is typically thought of through the lens of inorganic semiconductors, such as Si, where doping occurs by replacing a host atom by an impurity atom at a concentration of 10^{-6} to 10^{-3}.[3,24] N-type doping occurs when the impurity has one extra electron, such as a phosphorous impurity in silicon, and the electron is the charge carrier. P-type doping when the opposite occurs, and an impurity with one fewer electron is introduced, such as boron in silicon, and holes become the charge carrier. Due to the covalent interaction between the impurity and host atoms and the high dielectric constant of the host material, the doping efficiency (that is how many impurities successfully introduce a charge carrier) is high. Due to this high efficiency, only a low concentration of impurities needs to be introduced. This leads to a very low modification to a structure and hence its mobility, and the increase in conductivity due to doping is proportional to the increase in charge carrier concentration.

Doping within organic semiconductors, however, cannot operate in the same way. There is currently no synthetic equivalent to being able to remove one monomer out of thousands in order to introduce charge carriers. Introducing an atom such as a halide or alkali metal as a dopant in the material to react with the polymer to create charge carriers resulted in loosely bonded materials that diffused, resulting in instability in doping efficiency.[29,30] Hence, larger molecular dopants have been used to dope conjugated polymers. These dopants typically react via redox reaction with the polymer backbone to introduce (n-type) or take (p-type) an electron from the polymer backbone. Charge carriers, by nature, are of the opposite charge of the ion that is created by the reaction, and hence feel a Coulombic attraction to recombine and to not be mobile; screening that is present in inorganic semiconductors is much weaker in polymers due to a low dielectric constant. The size of the molecular dopant, sterically hindering its ability to get too close to the polymer backbone,

helps lead to better mobility of the charge carrier away from its parent ion. There is a long catalog of different molecular dopants of varying strengths, which can be seen for p-type doping in **Figure 6**.

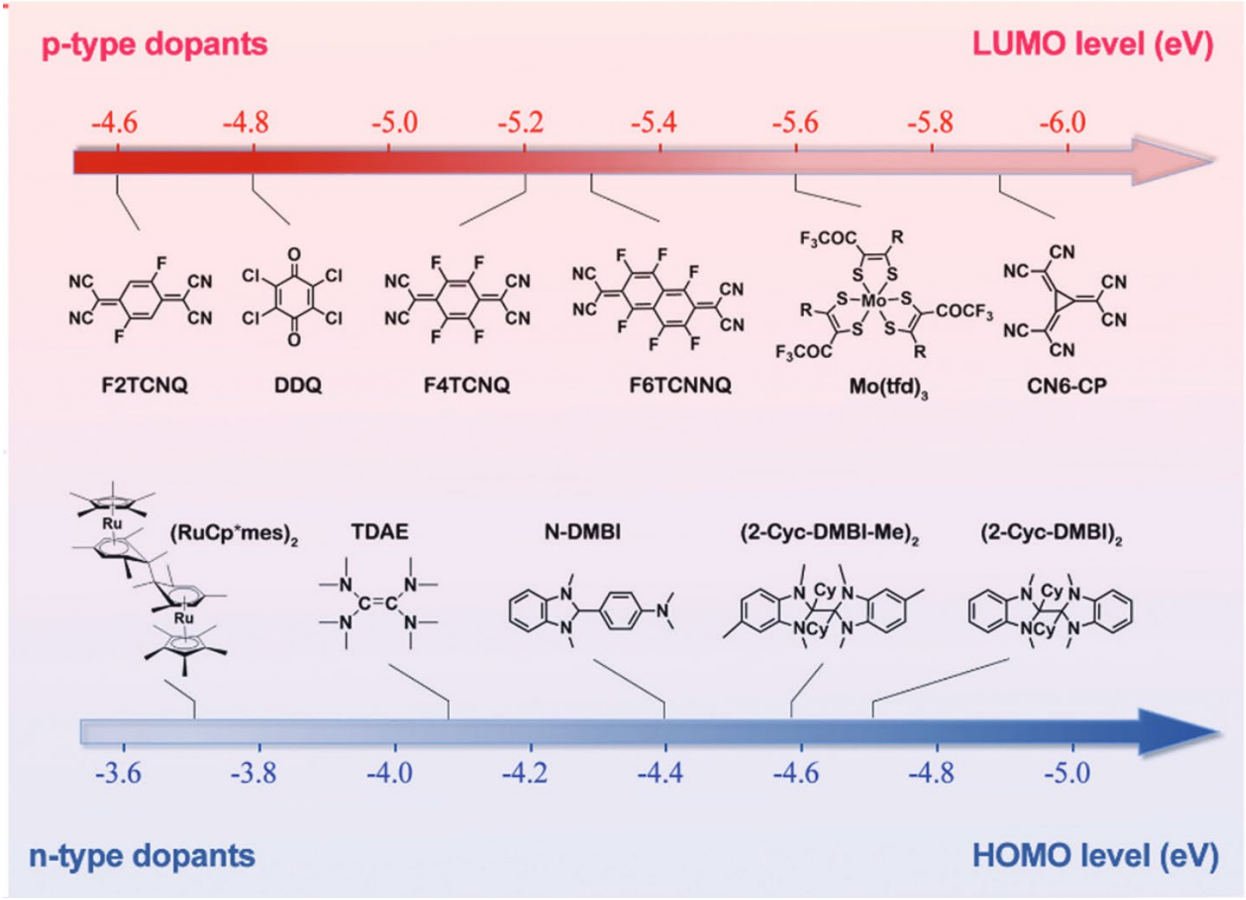

Figure 6. Molecular structure of several p-type and n-type dopants with varying strength. Reproduced from Zhao *et al*.[22]

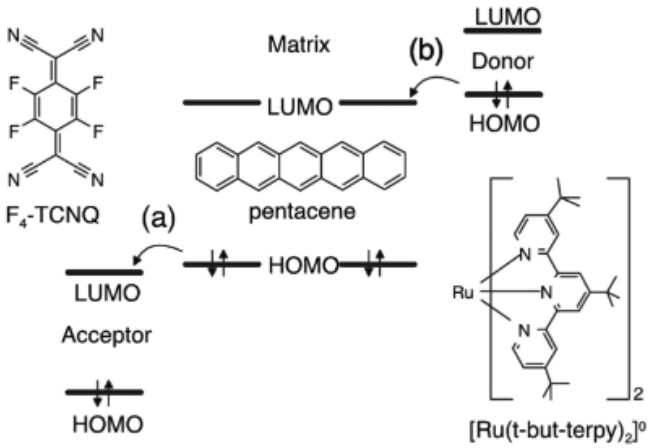

Figure 7. Model of p-type and n-type doping of pentacene by F4TCNQ (p-type doping) and [Ru(t-but-terpy)$_2$]^0 (n-type doping).

In order to introduce a hole/take an electron from pentacene, F4TCNQ's LUMO must be lower in energy relative to pentacene's HOMO. Similarly, for [Ru(t-but-terpy)$_2$]^0 to introduce an electron to pentacene, its HOMO must be higher in energy relative to pentacene's LUMO. Reproduced from Harada *et al*.[31]

From an energy-level perspective, the dopant must either have a LUMO deep enough to extract an electron from the polymer HOMO, or have a HOMO high enough to give an electron to the polymer LUMO.[32] This concept is known as a HOMO-LUMO overlap, and is shown in **Figure 7**. This process creates a negative (radical anion) or positive (radical cation) polaron on the conjugated polymer backbone, which are delocalized over several repeat units, and can lead to bipolarons at higher doping levels (see **Figure 8**). This process in general is called an "ion-pair formation", named after the ionized dopant and ionized repeat unit pairing post-doping, and for this process the degree of charge transfer is equal to 1.

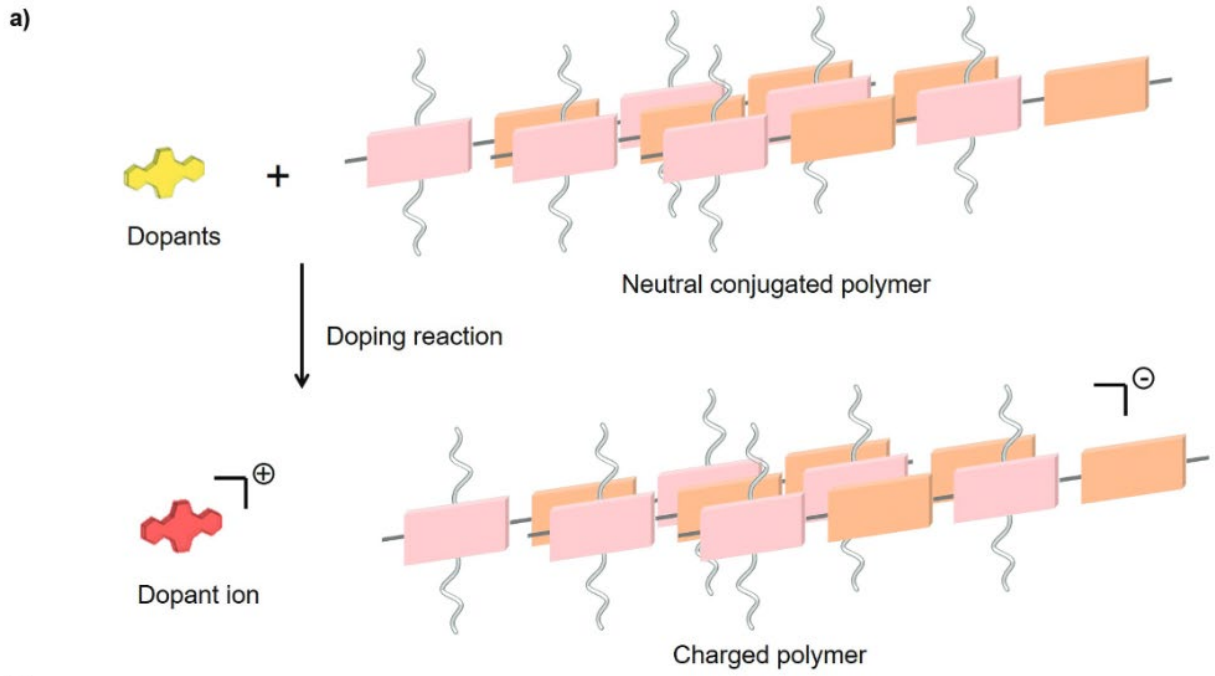

Figure 8. Schematic of n-type doping of a conjugated polymer.
An electron transfer from polymer to dopant leads the formation of a polaron. Reproduced from Xiong *et al*.[33]

However, this is not the only way a charge transfer can occur between molecular dopant and polymer. If the degree of charge transfer is less than 1, then a charge transfer complex (CTX) occurs. This reaction does not require a good HOMO-LUMO overlap, and instead results in a hybridization of the HOMO of the dopant and the LUMO of the polymer for the n-type doping (and vice versa for p-type doping).[32] This is roughly the analogue of a covalent bond formed between the linear combination of orbitals. This is already unideal, since this results in fewer charge carriers than in the ion pair case (integer charge transfer), and in P3HT and other similar molecules, requires the dopant migrate into the π-π stacking, disrupting the morphology of the conjugated polymer aggregate.

There is also the topic of doping efficiency, which was touched upon earlier in a discussion of the attraction of the created charge carrier and the parent ion and was also touched upon in the

discussion of charge transfer complexes. The efficiency of molecular dopants in conjugated polymers is much lower than that of an atomistic dopant in inorganic semiconductors. Not all dopants that infiltrate the film necessarily create charge carriers, not all dopants that create charge carriers create mobile charge carriers, and not all dopants that create mobile charge carriers create a whole charge. At very low doping levels, most charge carriers go towards filling charge traps in the system, which render them non-mobile.[34] The ability of the dopant to actually diffuse into and react with the dopant is a non-trivial aspect of efficiency, since the presence of dopant is sterically hindered in the aggregate domain; charge transfer complexes require specific placement of the dopant orbitals relative to the polymer backbone orbitals, and integer charge transfer still requires the dopant to be close enough to react.[35,36]

1.4.2 The interplay of molecular doping and polymer microstructure

The introduction of large molecular dopants to create charge carriers in a polymer semiconductor will cause modification of the material structure just by the definition of adding new components. Conjugated polymers, selected specifically for their ability to aggregate and have domains of high charge carrier mobility, may have that structure tested by the introduction of molecular dopants. There remains an underlying irony for the diffusion of dopants into the polymer: dopants interacting with the amorphous phase will find more space to diffuse into and therefore may disrupt the polymer's existing microstructure less, but the charge carriers created have low mobility, having little to no impact on the material's conductivity. For dopants to have a real impact, they must diffuse into the tightly packed aggregates, which have high mobility, but also are more susceptible to disruption. Within P3HT, dopants diffusing into the aggregate domains align themselves within the alkyl stacks, between neighboring polymer backbones, but on the sample plane as both backbones.[37] However, as referenced earlier, dopants that are in a

charge transfer complex with P3HT slip into the π-π stacking, whose distance is crucial for interchain transport, and thus charge carrier mobility for the material as a whole.[38] An example of this interaction is provided in **Figure 9**.

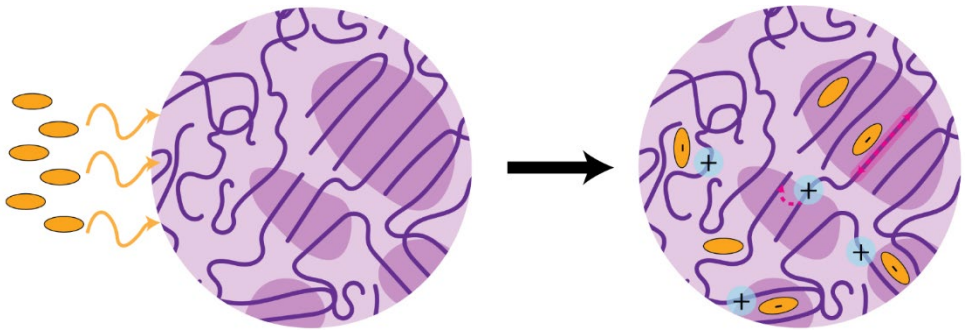

Figure 9. Diffusion and infiltration of dopants into conjugated polymer film.

Dopants can find themselves diffusing into the amorphous or aggregate domains within the polymer microstructure. Within the aggregate domain, however, large molecular dopants will disrupt the ordering of the conjugated backbone. Charge carriers, in this case holes, are introduced by the reaction of the dopant with the polymer backbone and must be able to travel both intrachain and interchain to conduct efficiently from aggregate domain to aggregate domain.

The method of molecular doping plays a large role in whether the microstructure of conjugated polymers, specifically picked for higher mobility, is disrupted. The most prominent of these methods are displayed in **Figure 10**. Mixed-solution doping is seen as a convenient way to introduce the polymer and dopant, as the polymer and dopant solutions are mixed directly and co-deposited on a substrate via a coating method. The method itself is easy to do, control, and is low-cost, which makes it attractive as a method that could be scaled up for industry.[22] However, it has been shown that mixed-solution doping causes several problems that lead to poor conductivity. Firstly, polymers and dopants often have differing solubility in the same solvent. This causes for polymers and dopants to self-aggregate, causing for poor mixing of polymer and dopant.[39] Secondly, too much dopant could be introduced into the film, which will cause phase separation

and poor microstructure for doping.[40] Thirdly, many polymers show reduced solubility when doped, which causes them to crash out of solution and negatively affect the film microstructure.[41]

An alternate method that has shown better preservation of underlying polymer microstructure is known as sequential doping. This method casts the polymer film on substrate before introducing dopant, allowing for the polymer to self-assemble into microstructures conducive for good charge carrier mobility before introducing dopant. Sequential doping is done either one of two ways: solution sequential doping, where the dopant is introduced into the film by a solutional orthogonal to the underlying polymer, and vapor sequential doping, which sublimes the dopant and allows it to diffuse into the polymer as vapor. Jacobs *et al*., comparing mixed solution doping to solution sequential doping of P3HT with a p-type dopant (F4TCNQ), found that mixed solution doping may cause disconnection of aggregates (*i.e.* a lack of tie chains) in the polymer film, increasing trapped charge carriers.[42] They also found that choice of solvent for the dopant was integral to improving performance of the sequential doping method: they found that doping from acetonitrile preserved the underlying structure better, whereas chlorobenzene swelled the aggregate domains and allowed too much dopant in, increasing the π-π stacking distance and lowering the interchain transport, reducing mobility. Patel *et al*. similarly compared vapor sequential doping to mixed solution doping, this time for PBTTT with two different dopants of varying strength (F2TCNQ and F4TCNQ), and found that although the local order was similar between the two methods, that vapor doping allowed for better alignment of aggregate domains, leading to better mobility.[43]

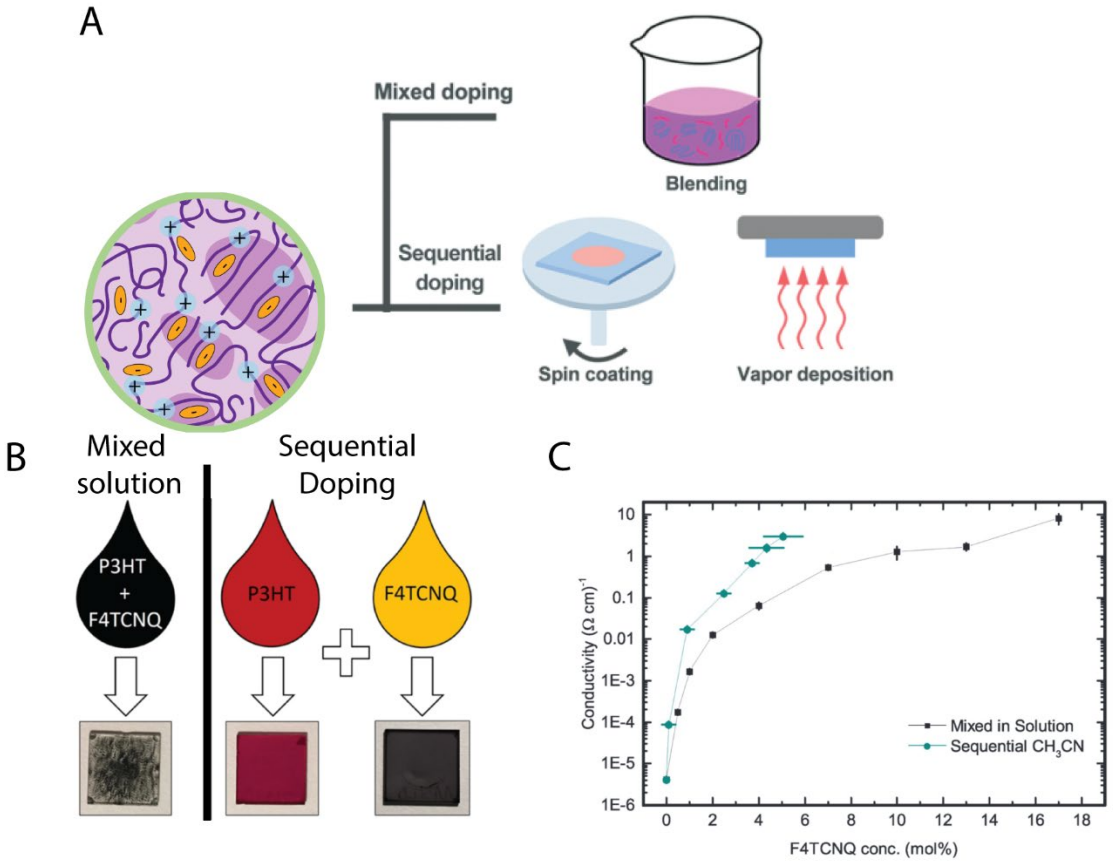

Figure 10. Comparison of molecular doping methods.

(A) Mixed doping blends solutions of polymer with dopant and co-deposits them as a film. Sequential doping introduces dopant post-deposition of the polymer film, whether through deposition in an orthogonal solvent or via sublimation and vapor infiltration. Adapted from Zhao *et al.*[22] (B) Thin films created from mixed solution and sequential doping methods. Reproduced from Scholes *et al.*[44] (C) Comparison of conductivity between mixed solution and molecular doping methods. Adapted from Jacobs *et al.*[42]

1.5 Probing the molecular doping of conjugated polymers

Many techniques and tools are used to give insight into the polymer structure, and how it is affected by processing. Here, we focus on a select few that are utilized more heavily within this dissertation.

1.5.1 UV-Vis-NIR absorption spectroscopy

Absorption spectroscopy is the method of passing a spectrum of light through a material and measuring which wavelengths of light were absorbed and by how much. Absorption occurs when the energy of a photon in a spectrum matches the energy difference between two quantum mechanical states of the material, whether this is electronic, rotational, or vibrational. For light in the ultraviolet (UV), visible (Vis), or near-infrared (NIR), these transitions tend to be of the electronic variety.

With conjugated polymers, the Spano model, named after its creator Frank C. Spano, models how order and disorder affect the absorption spectra for conjugated polymers.[45,46] A basic view of the breakdown between peaks attributed to the polymer aggregates and amorphous polymers can be seen within **Figure 11.** We can track the ratio of aggregate absorption versus amorphous absorption to gain insight into the ratio of each in the film. The ratio of the individual aggregate peaks can also be analyzed to provide information about the conjugation length, or a measure of how long the polymer backbone can extend straight out undisturbed, which plays a role in the delocalization of charge carriers within the system. A deeper look into this analysis can be found in the appendices to chapter 2 or 3 when applied to our own P3HT thin film system.

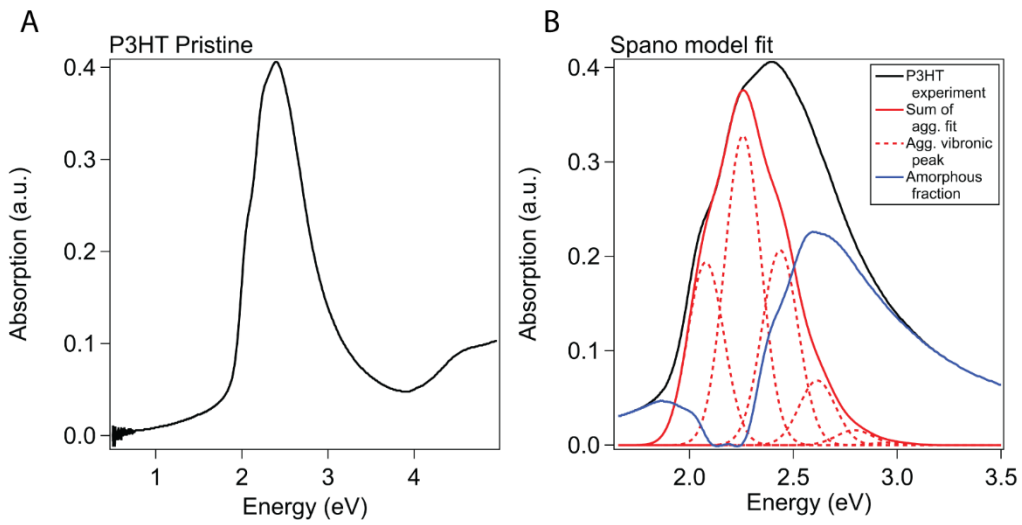

Figure 11. Breakdown of UV-Vis-NIR absorption of P3HT.

(A) An absorption spectra of thin film P3HT. (B) A breakdown of the spectra shown in (A). The lower energy peaks are shown as a collection of peaks attributed to the aggregate domain (red), whereas a broader single peak is attributed to the amorphous domain (blue).

One other set of analyses is dependent on the absorption of the charged conjugated polymer, which is red-shifted from the neutral peak. **Figure 12** shows an example of the conjugated polymer P3HT being doped, in (A) by electrochemical methods, and in (B) by the molecular dopant F4TCNQ. (B) shows us the growth of two sets of peaks as doping occurs: one at 0.5 eV, which is the first polaronic peak, and one at 1.5 eV, which includes both a broader second polaronic peak along with sharper peaks from the anionic dopant. (A) shows us this same transition, but without the dopant; therefore, the peak shown as growing at 800 nm (1.5 eV) is that second polaronic peak. Based upon the ratio of the first polaronic polymer absorption to the neutral polymer absorption (2.3 eV), we can make an estimation of the number of total sites versus the number of sites doped (*i.e.* how much of the polymer is doped).[47]

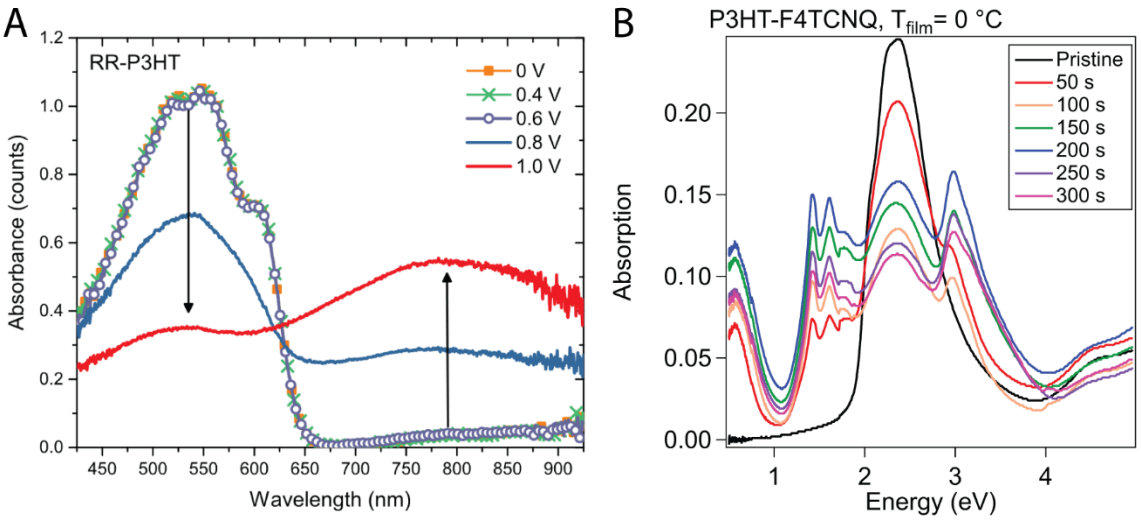

Figure 12. Evolution of P3HT absorption from doping.

(A) Electrochemical doping of P3HT by Nightingale *et al.*, which show the second polaronic peak without the characteristic peaks of dopant anion.[48] (B) Absorption of P3HT-F4TCNQ doped at various concentrations of dopant, which shows the evolution of the P3HT absorption as it's molecularly doped.

1.5.2 (Resonance) Raman spectroscopy

Raman scattering is the inelastic scattering of light. This means that when a monochromatic light source is incident upon a sample, the frequency of the light will be adjusted down or up. This is due to the changes in polarizability of the sample in question and is characteristic of the material. The modes typically being excited that change the polarization of the material are vibrational modes.[49]

In particular, this dissertation is interested in the application of Raman called "Resonance Raman Spectroscopy". This method takes advantage of a coupling between the electronic and vibrational transitions, which enhances the vibrational mode specifically on the group of atoms responsible for the electronic transition.[50] The intensities of certain Raman bands may be greatly increased, up to six magnitudes. In practice, this allows us to select specific wavelengths/energies

for our excitation lasers to select out which features in our material that we wish to study in more detail. For our conjugated polymers, our electronic absorption modes are well characterized by the UV-Vis-NIR absorption. This means that, like explained in the previous section, we can select for lasers with energies that could preferentially probe the neutral or charged parts of the polymer, or even more specifically within the neutral polymer peak, the amorphous or aggregate domains. This kind of insight is important into understanding how different treatments and processes affect the polymer and its structure.

Most of the Raman Resonance analysis used in this dissertation comes from the foundation that a paper by Nightingale *et al.* produced detailing how the conjugated polymer P3HT responded to being charged.[48] In their experiments, they used electrochemical doping, or applying a voltage to induce doping in the material, by utilizing an *in situ* cyclic voltammetry setup for both UV-Vis-NIR and Raman spectroscopy. Using what previous literature has stated about the nature of the resulting peaks in UV-Vis-NIR and to a lesser degree in Raman spectroscopy, they were able to assign identities and relationships to peaks that prove helpful in determining the microstructure of the material. We used this analysis in our own, vapor doped P3HT, as well as apply it to P3MEEMT (with the same conjugated, polythiophene backbone as P3HT) that was thermally treated, in order to better understand how these treatments affected the amorphous and aggregate domains separately.

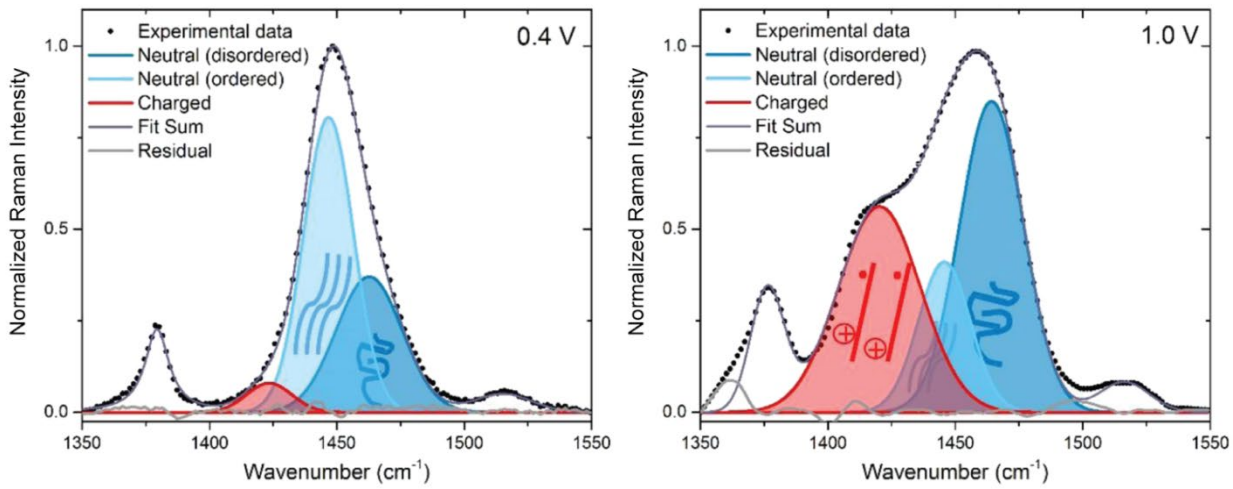

Figure 13. Raman spectroscopy with a 473 nm excitation laser of P3HT being charged electrochemically *in situ*.

Reproduced from Nightingale *et al.*[48]

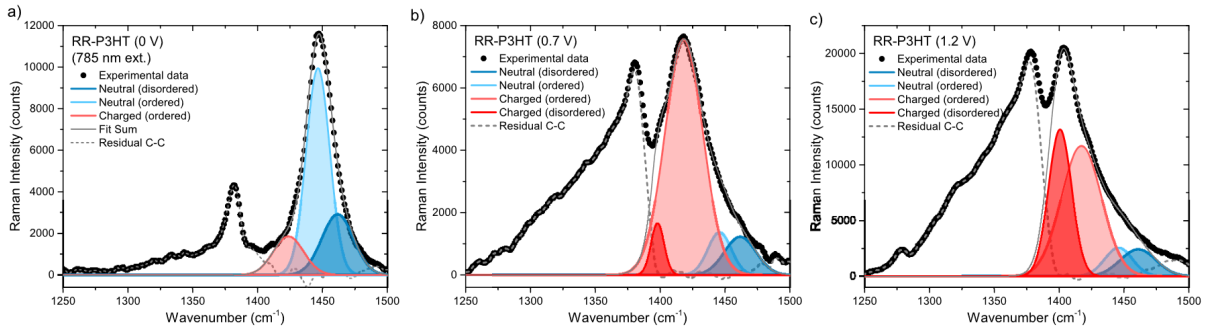

Figure 14. Raman spectroscopy with a 785 nm excitation laser of P3HT being charged electrochemically *in situ*.

Reproduced from Nightingale *et al.*[48]

Figure 13 details Raman spectroscopy of P3HT when using a 473 nm excitation wavelength, which aligns with the amorphous absorption of the neutral P3HT peak as seen in the Spano model fit in **Figure 11**. Similarly, **Figure 14** details Raman spectroscopy when using a 785 nm excitation wavelength, which aligns with the second polaron peak, and hence the charged polymer. Using either excitation wavelength, the main peak displayed ~1450 cm^{-1} is attributed to the symmetric

C=C intraring vibrational mode, and the peak displayed ~1380 cm^{-1} is attributed to the C-C intraring vibrational mode. In general, peaks attributed to the same vibrational mode but with a lower Raman shift (*i.e.* lower wavenumber) are from parts of the polymer that are more rigid.[51] Using previous peak attribution for neutral amorphous, neutral aggregate, charged amorphous, and charged aggregate P3HT, they show how the amorphous and aggregate domains change as the film is electrochemically doped.[51–53] By tracking the changes in these peaks in terms of location, width, and size, we can make detailed assessments on how our processings (in the case of this dissertation, vapor doping or thermally treating) affect our material.

1.5.3 Grazing incidence wide-angle X-ray scattering

Grazing incidence wide-angle X-ray scattering (GIWAXS) is a method for characterizing the ordered domains of conjugated polymers. These experiments often require high flux and photon collimation, and thus are typically performed at synchrotrons. Due to the nature of scattering showing high intensity over periodic elements, GIWAXS is often used to measure characteristic length scales of the ordered domains. By taking a "linecut" of the scattering, or a cross-section of the 2D scattering image plotting scattering intensity versus the radius from (0,0) on the image, the peaks of scattering intensity which mark these characteristic lengths can be converted from the reciprocal space of scattering into real space by using the equation $d = \frac{2\pi}{q}$.

For conjugated polymers, two important characteristic lengths are the alkyl stacking and the π-π stacking distance, as seen in **Figure 15**. The alkyl stacking distance describes the periodicity between individual chains in the plane of the polymer backbone, and π-π stacking distance describes the distance between individual chains out of the plane of the polymer backbone (*i.e.* the principal direction that charge carriers hop interchain).

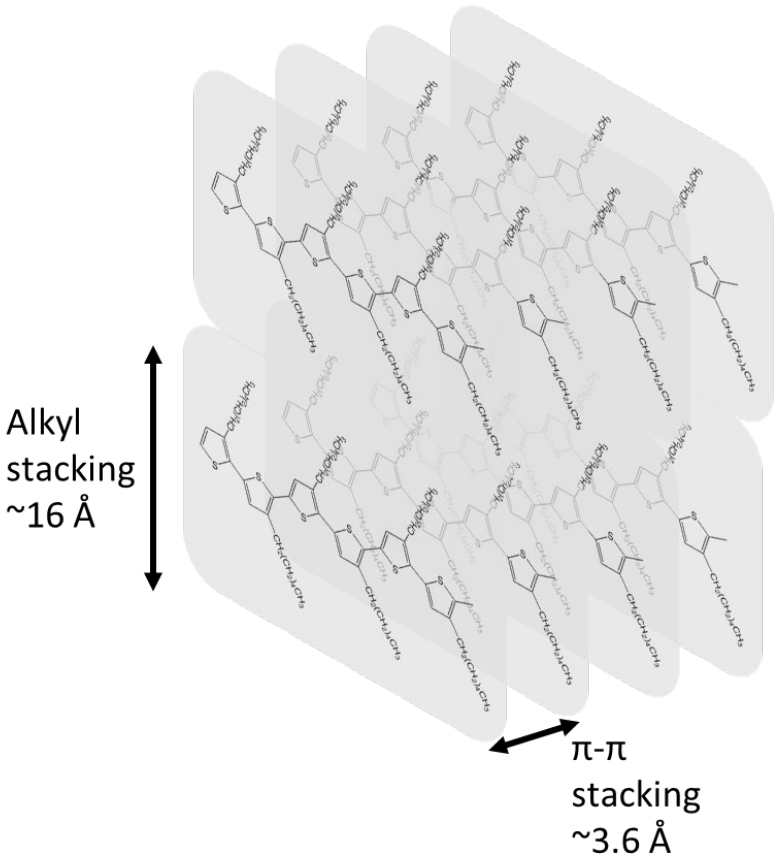

Figure 15. Characteristic lengths of conjugated polymers.
Displayed here for P3HT, the alkyl stacking distance (around 16 Å for P3HT) is in plane of the polymer backbones, whereas the π-π stacking distance goes through the plane of the polymer backbones (around 3.6 Å for P3HT).

GIWAXS can also shed light on longer-range order phenomena, such as alignment of ordered domains and size of ordered domains. **Figure 16** displays 2D GIWAXS scattering of aggregate domains with differing amounts of alignment between domains. Domains whose plane of conjugated backbones is perpendicular to the substrate are "edge-on", and their alkyl stacking peaks appear in the vertical, q_z direction. Domains whose conjugated backbone plane are parallel to the substrate are known as "face-on", and their alkyl stacking peaks appear in the horizontal, q_{xy}

direction. When aggregate domains in a film are well ordered relative to each other, the spread of intensities is much more condensed.

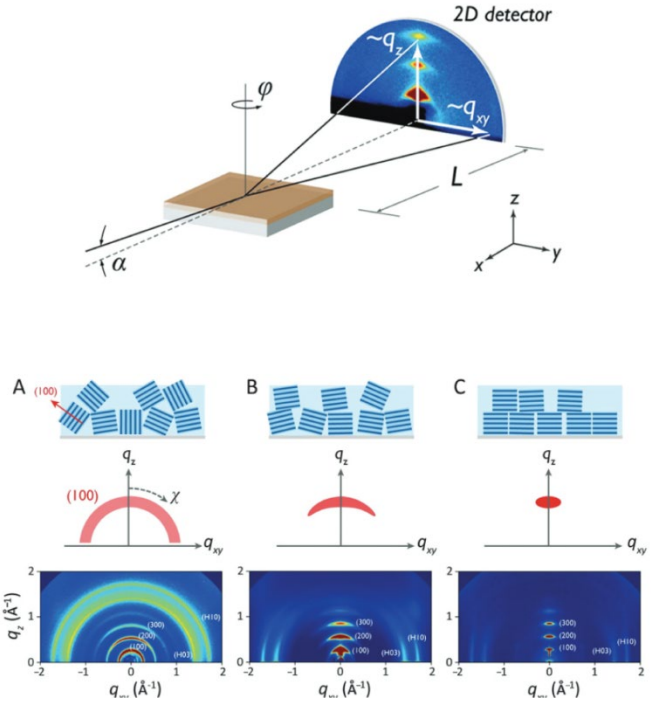

Figure 16. Overview of GIWAXS technique.
(Top) Schematic view of GIWAXS. (Bottom) Example of aggregate domain alignment as shown by GIWAXS. Reproduced from Rivnay *et al.*[54]

The average domain size can be estimated from the full-width-half-max (FWHM) of the alkyl stacking reflection peaks (labeled (100), (200), (300) in Miller Indices in **Figure 17**). Plotting the FWHM of each peak vs the first value of their Miller index description (*i.e.* 1, 2, 3) and fitting a line to find the y-intercept, the average grain size can be calculated as the reciprocal of this y-intercept ($2\pi/q$).

1.6 Objectives of our study on the interplay of polymer structure and vapor molecular doping

Our goal for this dissertation was to study how the polymer structure, both local and long-range, affected how vapor molecular doping progressed, as well as how the progress of vapor molecular doping affected the polymer structure in turn. In Chapter 2, we show how we structured a study of these phenomena, starting with the well documented polymer-dopant pairing of poly(3-hexylthiophene-2,5-diyl) (P3HT) and 2,3,5,6-tetrafluoro-7,7,8,8-tetracyanoquinodimethane (F4TCNQ). We constructed an *in situ* conductivity apparatus which allowed for simultaneous vapor doping and conductivity measurements with control of the rate of doping and the temperature of the polymer film. We then use the guidance of the *in situ* σ experiments to use scattering and spectroscopic techniques to characterize how the process of P3HT being vapor doped by F4TNQ affects the polymer structure as doping progresses. This chapter is written up in a manuscript form that is in revision for publication in a journal, under the title "Probing the evolution of conductivity and structural changes in vapor-F4TCNQ doped P3HT".

After successfully showing how this set of characterizations gave insight into the vapor doping process of a well-known pairing, we decided in Chapter 3 to study how dopant strength changed what we knew about how the polymer and dopant interacted during the vapor doping process. To this end, we used F4TCNQ's weaker cousins, FNTCNQ (N = 0, 1, 2), which had similar molecular structure, but different HOMO-LUMO overlap with P3HT. Using our battery of tests, we found that we could predict how the dopant's strength relative to the polymer's electron affinity in the amorphous and aggregate domains would result in charging of these domains, and how these domains would change due to the presence of charge carriers and dopant.

Lastly, we tried extending our set of analyses towards poly(3-(methoxyethoxyethoxymethyl)thiophene (P3MEEMT), which has the same backbone as P3HT, but polar sidechains with oligoethylene oxide for the purpose of solvating ions for ionic transport. P3MEEMT is a target for mixed electronic-ionic conductivity. We therefore studied the effect of blending LiTFSI salt with P3MEEMT on the structure of the polymer. We found, in combination with the thermal transitions that differential scanning calorimetry indicated that P3MEEMT had, that thermally treating P3MEEMT above these thermal transitions with and without salt had a drastic effect on the resulting polymer structure on both a local and long-range level. We also found that the ionic and electronic conductivity both improved with a thermal treatment that increased the aggregate domain size and edge-on alignment.

1.7 References

1. S. O. Kasap, *Principles of Electronic Materials and Devices*, McGraw Hill, New York, 3rd edn., 2006.
2. R. E. Hummel, *Electronic Properties of Materials*, Springer US, New York, 4th edn., 1993.
3. I. Salzmann, G. Heimel, M. Oehzelt, S. Winkler and N. Koch, *Acc. Chem. Res.*, 2016, **49**, 370–378.
4. A. J. Heeger, N. S. Sariciftci and E. B. Namdas, *Semiconducting and Metallic Polymers*, Oxford Graduate Texts. Oxford University Press, Oxford, UK, 2010.
5. G. Hadziioannou and P. F. van Hutten, *Semiconducting Polymers: Chemistry, Physics and Engineering*, Wiley-VCH, New York, USA, 2000.
6. B. R. Hsieh and Y. Wei, *Am. Chem. Soc.*, 1999, 735.
7. T. A. Skotheim, *Conjugated Polymers: Theory, Synthesis, Properties, and Characterization, Handbook or Conducting Polymers*, CRC Press, Boca Raton, FL, USA, 3rd ed., 2007.
8. S.-M. Lee, J. H. Kwon, S. Kwon and K. C. Choi, *IEEE Trans. Electron Devices*, 2017, **64**, 1922–1931.
9. Samsung, OLED Display, https://www.samsungdisplay.com/eng/tech/oled-display.jsp.
10. Plastic Logic, Signage.
11. M. McGrath, Organic solar cells set ‘remarkable’ energy record, https://www.bbc.com/news/science-environment-45132427.
12. H. Wang and C. Yu, *Joule*, 2019, **3**, 53–80.

13. A. Mills, *III-Vs Rev.*, 2004, **17**, 22–24.

14. J. Song, H. Lee, E. G. Jeong, K. C. Choi and S. Yoo, *Adv. Mater.*, 2020, **32**, 1907539.

15. S. M. Sze and K. K. Ng, *Physics of Semiconductor Devices*, John Wiley & Sons, Inc., Hoboken, NJ, USA, 2006.

16. X. Guo, Y. Xu, S. Ogier, T. N. Ng, M. Caironi, A. Perinot, L. Li, J. Zhao, W. Tang, R. A. Sporea, A. Nejim, J. Carrabina, P. Cain and F. Yan, *IEEE Trans. Electron Devices*, 2017, **64**, 1906–1921.

17. A. C. Arias, J. D. MacKenzie, I. McCulloch, J. Rivnay and A. Salleo, *Chem. Rev.*, , DOI:10.1021/cr900150b.

18. H. Sirringhaus, *Adv. Mater.*, 2014, **26**, 1319–1335.

19. O. Inganäs, *Adv. Mater.*, , DOI:10.1002/adma.201800388.

20. R. Volpi and M. Linares, in *Chemical Modelling*, 2016, vol. 13, pp. 1–26.

21. R. Kroon, D. A. Mengistie, D. Kiefer, J. Hynynen, J. D. Ryan, L. Yu and C. Müller, *Chem. Soc. Rev.*, 2016, **45**, 6147–6164.

22. W. Zhao, J. Ding, Y. Zou, C. Di and D. Zhu, *Chem. Soc. Rev.*, 2020, **49**, 7210–7228.

23. T. Ma, B. X. Dong, G. L. Grocke, J. Strzalka and S. N. Patel, *Macromolecules*, 2020, **53**, 2882–2892.

24. X. Lin, Molecular Doping of Organic Semiconductors, 2018.

25. S. V. Kamath, K. Aruchamy and N. Sanna Kotrappanavar, in *Polymer-Based Advanced Functional Composites for Optoelectronic and Energy Applications*, Elsevier, 2021, pp. 31–49.

26. R. Noriega, J. Rivnay, K. Vandewal, F. P. V. Koch, N. Stingelin, P. Smith, M. F. Toney and A. Salleo, *Nat. Mater.*, 2013, **12**, 1038–1044.

27. F. P. V. Koch, J. Rivnay, S. Foster, C. Müller, J. M. Downing, E. Buchaca-Domingo, P. Westacott, L. Yu, M. Yuan, M. Baklar, Z. Fei, C. Luscombe, M. A. McLachlan, M. Heeney, G. Rumbles, C. Silva, A. Salleo, J. Nelson, P. Smith and N. Stingelin, *Prog. Polym. Sci.*, 2013, **38**, 1978–1989.

28. E. D. Gomez, K. P. Barteau, H. Wang, M. F. Toney and Y.-L. Loo, *Chem. Commun.*, 2011, **47**, 436–438.

29. L. S. Hung, C. W. Tang and M. G. Mason, *Appl. Phys. Lett.*, 1997, **70**, 152–154.

30. G. Parthasarathy, C. Shen, A. Kahn and S. R. Forrest, *J. Appl. Phys.*, 2001, **89**, 4986–4992.

31. K. Harada, M. Riede, K. Leo, O. R. Hild and C. M. Elliott, *Phys. Rev. B*, 2008, **77**, 195212.

32. I. E. Jacobs and A. J. Moulé, *Adv. Mater.*, 2017, **29**, 1703063.

33. M. Xiong, J.-Y. Wang and J. Pei, *Org. Mater.*, 2021, **03**, 001–016.

34. P. Pingel and D. Neher, *Phys. Rev. B*, 2013, **87**, 115209.

35. B. Neelamraju, K. E. Watts, J. E. Pemberton and E. L. Ratcliff, *J. Phys. Chem. Lett.*, 2018, **9**, 6871–6877.

36. K. E. Watts, B. Neelamraju, E. L. Ratcliff and J. E. Pemberton, *Chem. Mater.*, 2019, **31**, 6986–6994.

37. E. Lim, K. A. Peterson, G. M. Su and M. L. Chabinyc, *Chem. Mater.*, 2018, **30**, 998–1010.

38. E. M. Thomas, E. C. Davidson, R. Katsumata, R. A. Segalman and M. L. Chabinyc, *ACS Macro Lett.*, 2018, **7**, 1492–1497.

39. A. R. Chew, R. Ghosh, Z. Shang, F. C. Spano and A. Salleo, *J. Phys. Chem. Lett.*, 2017, **8**, 4974–4980.

40. D. T. Duong, C. Wang, E. Antono, M. F. Toney and A. Salleo, *Org. Electron. physics, Mater. Appl.*, , DOI:10.1016/j.orgel.2013.02.028.

41. M. T. Fontana, D. A. Stanfield, D. T. Scholes, K. J. Winchell, S. H. Tolbert and B. J. Schwartz, *J. Phys. Chem. C*, 2019, **123**, 22711–22724.

42. I. E. Jacobs, E. W. Aasen, J. L. Oliveira, T. N. Fonseca, J. D. Roehling, J. Li, G. Zhang, M. P. Augustine, M. Mascal and A. J. Moulé, *J. Mater. Chem. C*, 2016, **4**, 3454–3466.

43. S. N. Patel, A. M. Glaudell, K. A. Peterson, E. M. Thomas, K. A. O'Hara, E. Lim and M. L. Chabinyc, *Sci. Adv.*, , DOI:10.1126/sciadv.1700434.

44. D. T. Scholes, S. A. Hawks, P. Y. Yee, H. Wu, J. R. Lindemuth, S. H. Tolbert and B. J. Schwartz, *J. Phys. Chem. Lett.*, 2015, **6**, 4786–4793.

45. F. C. Spano, *J. Chem. Phys.*, 2005, **122**, 234701.

46. F. C. Spano, *Chem. Phys.*, 2006, **325**, 22–35.

47. T. L. Murrey, M. A. Riley, G. Gonel, D. D. Antonio, L. Filardi, N. Shevchenko, M. Mascal and A. J. Moulé, *J. Phys. Chem. Lett.*, 2021, **12**, 1284–1289.

48. J. Nightingale, J. Wade, D. Moia, J. Nelson and J.-S. Kim, *J. Phys. Chem. C*, 2018, **122**, 29129–29140.

49. N. John and S. George, in *Spectroscopic Methods for Nanomaterials Characterization*, Elsevier, 2017, pp. 95–127.

50. R. S. Czernuszewicz and M. B. Zaczek, in *Encyclopedia of Inorganic and Bioinorganic Chemistry*, John Wiley & Sons, Ltd, Chichester, UK, 2011.

51. W. C. Tsoi, D. T. James, J. S. Kim, P. G. Nicholson, C. E. Murphy, D. D. C. Bradley, J. Nelson and J.-S. Kim, *J. Am. Chem. Soc.*, 2011, **133**, 9834–9843.

52. J. Razzell-Hollis, S. Limbu and J.-S. Kim, *J. Phys. Chem. C*, 2016, **120**, 10806–10814.

53. S. Wood, J. R. Hollis and J.-S. Kim, *J. Phys. D. Appl. Phys.*, 2017, **50**, 073001.

54. J. Rivnay, S. C. B. Mannsfeld, C. E. Miller, A. Salleo and M. F. Toney, *Chem. Rev.*, 2012, **112**, 5488–5519.

Chapter 2: Probing the evolution of conductivity and structural changes in vapor-F4TCNQ doped P3HT

2.1 Abstract

Vapor molecular doping has been shown to exhibit high conductivity (σ) for conjugated polymer semiconductors, but our understanding on the vapor molecular doping process is still low due to the high complexity of the interaction. Here, we develop an in situ conductivity method to measure σ during the process of vapor doping, which allows for further insight on how the polymer material changes when exposed to gradually higher concentration of dopant. These results were then compared to films doped to times throughout the doping process, which were taken to study their spectroscopy and microscopy. We find that the timing for the maximum σ of our films corresponds heavily to a saturation of effects from vapor doping, including charge concentration and ordered structural changes, while indicating that changes in disordered phases continue to occur past this time. We posit that the instability of the polymer σ past the maximum seen in in situ conductivity measurements is due to the changes in the disordered phases. We also believe in the power of this methodology for more novel polymer-dopant pairings, and the ability of findings from similar studies to find polymer chemistries and structures that are conducive to high, stable conductivities.

2.2 Introduction

Pushing the current limits of electronic conductivity in organic semiconductors is intimately linked to the method of doping. Recently, sequential doping has emerged as an effective method in controlling doping level and ultimately achieving high electronic conductivity.[1–3] The sequential doping method involves taking a pre-cast film and subsequently infiltrating dopant molecules through mass actions either using dopant vapor or dopant in solution. The ability to achieve high

conductivity through this method is related to the resiliency of the host materials to accept a high quantity of dopant molecules (10-30 mol%) while maintaining the underlying morphology that promotes efficient charge mobility.[4–7]

Consequently, leveraging sequential doping is of both technological and fundamental significance. Relative to inorganic semiconductors, organic materials are low-cost to produce and use earth-abundant materials.[4,5] Accessible properties such as their light weight, flexibility, and tunability enable forward-thinking technologies such as curved displays, wearable energy harvesting, and thin, flexible solar cells.[8–11] The sequential doping method allows for unique and powerful processing strategies, such as the functionally graded doping design for polymer thermoelectrics shown by Ma *et al*.[12] This doping method has also been used to make comparisons between the charge transfer mechanisms of conductive polymers.[13] Here, we focus on investigating the vapor doping methodology and its mechanisms.

Electronic conductivity (σ) is directly proportional to the charge carrier concentration (n) and mobility (μ). Molecular dopants are introduced into underlying polymeric material to increase n, yet this may disrupt the high μ that conjugated polymers are selected for.[14,15] The complicated interplay between the polymer and dopant directs these two crucial properties. Multiple factors play into this interaction. One such factor is the chemical reaction between the polymer and dopant. The process of introducing charges into the system occurs through a redox reaction. This can take the form of an integer charge transfer, which, for the case of the conjugated polymer – small molecular dopant system, places the dopant between the polymer sidechains, or a charge transfer complex (introducing only a fractional charge), which situates the dopant between the backbones of the neighboring polymer chains (within the π- π stacking).[16–19] A major factor that determines the type and efficiency of the charge transfer is the relation between the electronic structures of

the polymer and dopant, in particular their HOMO-LUMO overlap.[20–23] For example, planar molecular dopants such as F4TCNQ, F2TCNQ, F1TCNQ, and TCNQ only differ by the number of fluorine atoms substituted in place of hydrogen, yet these dopants' LUMO differ by a range of 0.8 eV, which has a significant effect on the effectiveness of the dopant.[24]

As noted earlier, many of these properties are controlled by the method by which the dopant is introduced into the polymeric material.[25,26] Jacobs *et al*., to our knowledge, first demonstrated the difference between mixing dopant and polymer in solution before casting the polymer as a film (labeled "mixed solution") and casting the polymer as a film before depositing the dopant on top in an orthogonal solution (known as "sequential solution doping").[1] Hynynen *et al*. use sequential vapor doping to show that sequential doping produces higher σ to similar materials doped via the mixed solution method at the same dopant concentration.[27] This effect has been shown through multiple studies to be due to the sequential solution doping method preserving the underlying morphology of the polymer, and in some recent studies, shown to further order the amorphous fractions of the film, leading to higher charge carrier mobility.[1,28–30]

Insights about the structural effects of molecular doping provide a view into the delicate balance in the interaction between dopant and polymer. This intricate interplay is demonstrated by increased ordering in more amorphous regimes and a growth in long-range order at optimal doping concentrations, while too much dopant will start to disorder the backbone π-π overlap necessary for efficient interchain backbone conduction.[3,31]

The complexity of the interactions involved in sequential vapor doping make an exact understanding of the molecular doping mechanism difficult. Dependence of the sequential vapor doping mechanism on film temperature also remains unclear, with proposed changes around the glass transition temperature of the conjugated backbone.[29,31,32] While previous studies have

contributed to a deeper understanding on the sequential vapor doping process, a few targeted characterizations for further elucidation of the structure-transport properties of vapor doped semiconducting polymers remain. First, what is the instantaneous progression of σ with increasing dopant concentration during vapor doping? Second, what is the role of the film temperature on the dynamics of vapor doping? Lastly, what is the evolution of the segregation of dopants between ordered, crystalline domains and disordered, amorphous domains at different doping levels?

To address these questions, we investigate the structure-transport properties of the archetypical conjugated polymer-dopant pairing, P3HT:F4TCNQ. Unique to our study are *in situ* measurements of σ while vapor doping using a custom-fabricated doping apparatus. This approach provides a granular understanding of the evolution of electronic conduction properties as a function of dopant concentration. From this understanding, we probe what effect the temperature of the polymer film has on the dynamics of molecular doping, and we compare the shape of the σ curve to the evolution of the disordered and ordered regimes of the polymer. Our work elucidates how the *in situ* conductivity curve, when considered with targeted physical and electronic characterization, further develops molecular doping as a path to electronic polymeric materials.

2.3 Results and Discussion

2.3.1 Neat P3HT thin film fabrication and properties

Thin films of P3HT were fabricated through a spin coating method (see Methods section for details). A single processing condition was applied in this study to ensure consistent properties of pre-cast films for vapor doping. In short, thin films were spin coated from a chlorobenzene solution and subsequently heated at 100 °C to drive out residual solvent. The resultant P3HT thin films had a thickness of 48 ± 5 nm based on AFM. In **Figure 25** we show the UV-vis-NIR spectrum of the neat P3HT thin film. Analysis of the spectrum using the Spano model revealed the degree of

aggregation is 37%; this result is discussed in detail in the supporting information.[33,34] Additionally, a cyclic voltammetry measurement, as seen in **Figure 26**, indicates that the onset potential is 0.093 V vs Fc/Fc^+ and, thus an ionization energy of -5.10 eV. F4TCNQ's reported electron affinity is reported as around -5.2 eV, leading to efficient integer charge transfer.[21]

2.3.2 Apparatus for controlled vapor-doping experiments

We constructed a doping chamber and sample holder for the purpose of controlled vapor doping and *in situ* conductivity measurements of a polymer thin film sample held at a constant temperature (**Figure 17**, see **Figure 27** for 3D rendering). More detailed descriptions and procedures are located in the Methods section and the Supporting information. The following summarizes the pertinent features of the apparatus.

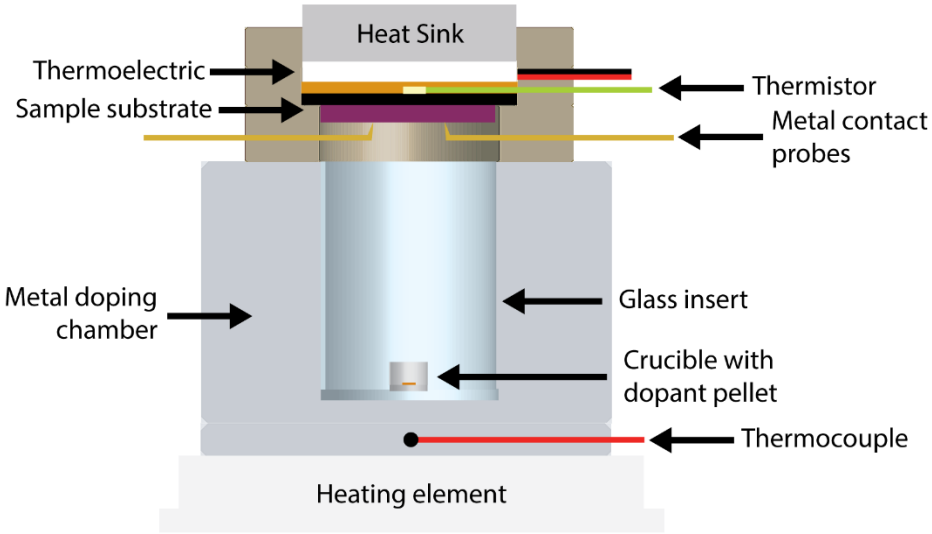

Figure 17. Cross section of apparatus for vapor doping experiments.
Metal doping chamber houses glass insert with alumina crucible and F4TCNQ pellet within. F4TCNQ pellet is vaporized by heating the metal doping chamber to a desired temperature on a hot plate, whose temperature in monitored by a thermocouple in the base. The sample is simultaneously measured and held stable by the metal contact probes, and a thermoelectric holds the temperature of the sample to a set constant from 0 °C to 70 °C. All vapor doping experiments were performed in an argon glovebox.

The sample holder has a thermoelectric module (Peltier) for active temperature control of the thin film sample (T_{film}). The thermoelectric module, coupled with a water-cooling heat sink, permitted a stable operational range from 0 °C to 70 °C. This temperature was measured using a thermistor that was thermally connected to the sample substrate, and thus ensured stable temperature measurement and control of the sample directly. Two stainless-steel probes allowed for electrical contact with the sample during vapor doping.

The doping chamber was designed for controlled sublimation of dopant by heating at the ambient pressure of the glovebox. The chamber housing is made of stainless-steel metal, which is in constant thermal contact with the heating source (ceramic hotplate). A cylindrical glass insert is placed in the center of the doping chamber to house the dopant source, which is placed on the bottom as a pellet in an alumina crucible. A thermocouple is placed near the dopant source at the base of the metal chamber to monitor the dopant sublimation temperature (T_{dopant}), which was fixed to 200 °C in this study unless otherwise stated.

2.3.3 P3HT-F4TCNQ *in situ* conductivity

To study vapor doping conductivity *in situ*, thin film P3HT (*ca.* 50 nm) was doped with F4TCNQ with T_{film} = 0, 30, and 70 °C. This range of temperatures is significant for probing the vapor doping process of P3HT above and below the T_g of the polymer backbone, which is known to be around 20 °C (dependent on the molecular weight and regioregularity).[35] Another potential effect would rely on how quickly the diffusion into the polymer would occur; one hypothesis is that at higher T_{film}, the diffusion would occur more quickly and would accelerate the rise of σ.

Using an interdigitated electrode device, the σ of the thin film can be tracked from its beginning to its end over six orders of magnitude. σ of P3HT was measured while doping with F4TCNQ up until 20 min, at which point all curves had established an equilibrium σ.

Representative curves at these three different T_{film} can be seen in **Figure 18**. A common pattern appears for all three temperatures, which looks similar to the standard relation between σ and dopant concentration published many times prior.[3,30,36] The σ profile shows a significant rise upon the film's first introduction to dopant, exponentially climbing around five orders of magnitude in around a minute, then slows to climbs linearly, and finally reaches a maximum electronic conductivity (σ_{max}) within four minutes. Past this point, the magnitude of the σ drops, which previously has been attributed to the oversaturation of the dopant degrading the order of the polymer, which in turn reduces the mobility of the charge carriers in the material.[27]

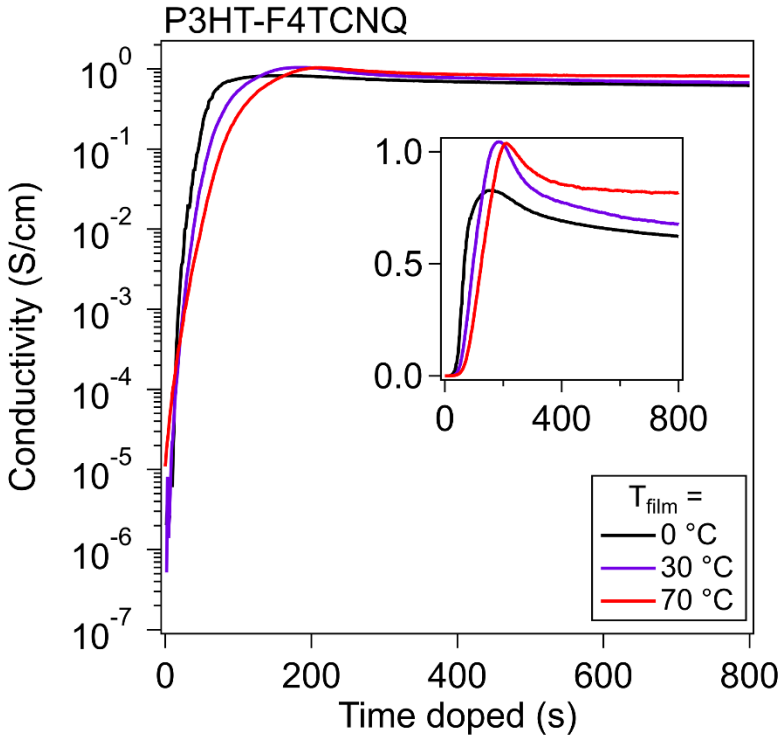

Figure 18. *In situ* conductivity curves of F4TCNQ-doped P3HT.

The σ for P3HT over the course of doping with F4TCNQ is shown for three different T_{film}. The semilog plot shows that σ rises five orders of magnitude in around two minutes, and the linear inset details the form of the drop in σ past σ_{max}.

A few comparisons stand out between the three T_{film}. The σ_{max} and general trends are almost identical between runs at the different T_{film}. T_{film} = 0 °C reached a σ_{max} about a minute faster than the films at T_{film} = 30 °C and T_{film} = 70 °C. We hypothesize that the difference in the timing of σ_{max} (t_{max}) is attributed to the adsorption of vaporized dopant occurring more quickly due to the larger temperature gradient between dopant and film. Across five runs, $\sigma_{max,0°C}$ = 2.29 ± 0.29 S/cm, $\sigma_{max,30°C}$ = 2.38 ± 0.26 S/cm, and $\sigma_{max,70°C}$ = 1.34 ± 0.04 S/cm; this shows a trend of σ rising highest when T_{film} is the lowest, but in general σ_{max} does not vary much from T_{film} to T_{film}. The lack of strong temperature dependence on the conductivity curve indicates that the dopant diffusion does not depend on the backbone T_g for fast diffusion, likely passing through the space provided by the alkyl sidechains. Post σ_{max}, the films retain over 70% of their σ_{max} once they stabilize out, which, in these experiments, did not differ consistently with T_{film}.

In order to probe the universality of the σ profile, a few further *in situ* conductivity experiments were conducted using the P3HT-F4TCNQ system. In the first experiment, we reduced the sublimation temperature of the dopant (T_{dopant}) from 200 °C to 160 °C. We did this to test if a slower sublimation rate would change the trends of the in situ σ curve. Shown in **Figure 19A**, these doping curves at T_{dopant} = 160 °C showed a similar σ_{max} to curves with T_{dopant} = 200 °C. When the doping curve for T_{dopant} = 160 °C was scaled by sublimation rate, its shape closely matched curves with the standard T_{dopant} = 200 °C, as seen in **Figure 19**B.

In a second experiment, P3HT films were annealed to a temperature high enough to melt-crystallize them (250 °C for 10 min, then slowly cooled), and then were subjected to an *in situ* conductivity experiment. We hypothesize that the higher and more stable σ is due to the melt-crystallized P3HT having a higher fraction of crystalline domains**.** The overlap of the highest occupied molecular orbital (HOMO) of the aggregate-P3HT with the lowest unoccupied molecular

orbital (LUMO) of the F4TCNQ is stronger than that of the amorphous-P3HT HOMO with the F4TCNQ LUMO and should result in a higher number of charge carriers generated overall with better stability of the reaction between the dopant and polymer.[37]

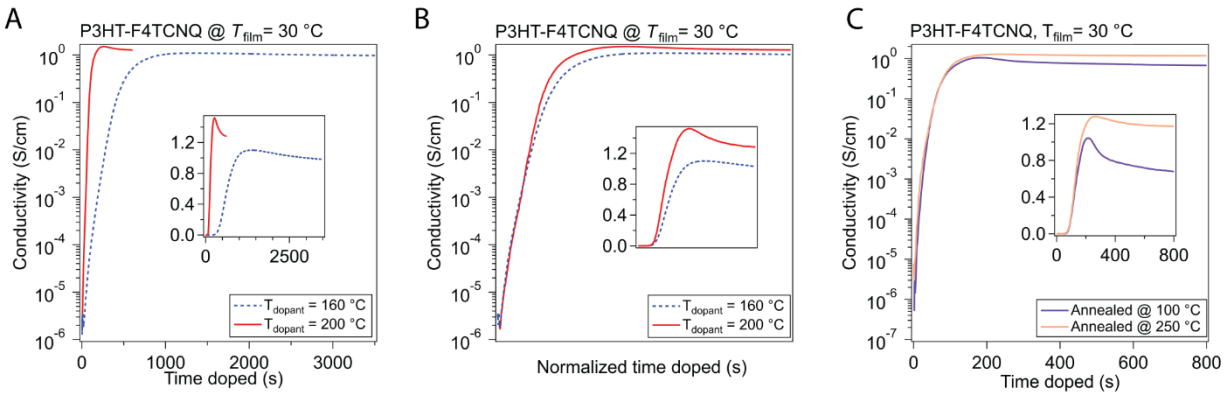

Figure 19. *In situ* σ curves for different dopant temperatures and processing methods. (A) F4TCNQ was set to 200 °C for the entirety of the F4TCNQ doping experiments shown in Figure 18. An experiment was conducted in order to test how lowering the dopant temperature, and hence the sublimation rate, would affect the conductivity curve. (C) All other samples were annealed below their recrystallization temperature. Experiments were conducted to see if recrystallizing the P3HT at 250 °C would result in different doping curves.

2.3.4 P3HT-F4TCNQ *in situ* conductivity "curtailed" experiments show difference in curve behavior pre and post t_{max}

We conducted *in situ* conductivity experiments where the sample was taken from the dopant vapor at specific doping times. Samples were made by exposing them to dopant for intervals apart to explore how the shape of the doping curve was affected by when the sample was taken off (when the doping curve was "curtailed").

These curves were shown in **Figure 20** at the same three T_{film} as the *in situ* conductivity experiments. Using the black curve as the non-curtailed sample (where the sample was not taken

off the dopant while being measured), the dotted lines indicate separate samples which were taken off at 50 s intervals from each other, from 50 s to 300 s.

When comparing the shape of the *in situ* conductivity curve post curtailing for these samples, the samples curtailed before and after t_{max} show different behavior. For samples curtailed before (*e.g.* 50 s, 100 s), the drop in σ resolves quickly and retains most of the σ before curtailing. For samples curtailed closer to, and especially after t_{max}, relatively large reductions occur in σ (~80 to 90% the pre-curtail σ) that take minutes to stabilize. We hypothesize from this transition that t_{max} represents a tipping point towards instability in σ, whether through a reduction in charge carriers or the mobility of those charge carriers.

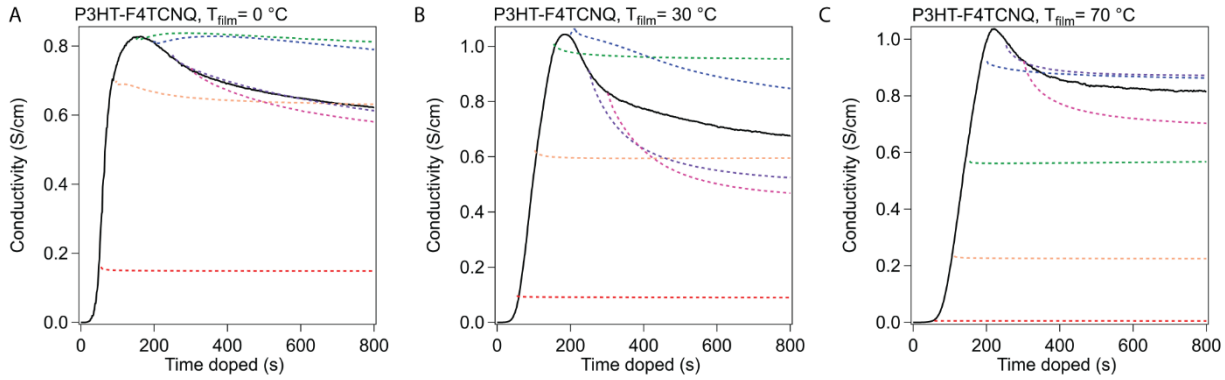

Figure 20. Stabilization of σ at 50 s intervals.

Samples of F4TCNQ-doped P3HT were taken off the dopant ("curtailed") at 50 s intervals as to replicate the conditions of samples that were taken off at that time for other experiments, such as UV-Vis, FTIR, Raman spectroscopy, and grazing incidence wide angle x-ray scattering. The dotted line indicates the shape of the σ curve when the sample is taken off at the beginning of the dotted line (*i.e.* the red dotted line was curtailed at 50 s). The solid line indicates the curve of σ when doping is not curtailed.

2.3.5 Absorption measurements of P3HT-F4TCNQ track fraction of doped sites to *in situ* conductivity curve

To gain further insight into the nature of the shape of the *in situ* doping curve, we used UV-Vis-NIR and FTIR spectra to determine a relative measure of doping level and the doping mechanism.

Figure 21A shows the UV-Vis-NIR absorption for a P3HT film doped in 50 s intervals, from neat to 300 s for T_{film} = 0 °C (**Figure 28** shows the spectra for T_{film} = 30, 70 °C). The black curve, for the neat polymer, shows a peak at 2.3 eV that corresponds to the primary absorption peak for neutral P3HT. Upon doping, peaks at 0.5 and 1.5 eV appear, which correspond to allowed sub-gap transition bands in positive polarons, as well as peaks at 1.4 and 1.6 eV, which come from the F4TCNQ radical anion and is indicative of an integer charge transfer doping mechanism.[30,38] Murrey *et al*. utilize a parameter Θ, which they define as the fraction of doped P3HT sites over the total available P3HT sites. They linearly approximate this from the absorption using the equation

$$\Theta = \frac{A_P}{A_P + A_N} \qquad \text{(Equation 1)}$$

where A_P is the integral of the polaron absorption peak fit at 0.5 eV and A_N is the integral of the neutral P3HT absorption at 2.3 eV.[39] We fit our spectra (using a fitting seen in **Figure 29**) to extract out the absorptions necessary to calculate Θ, and the evolution of Θ was plotted versus time doped in **Figure 21B**.

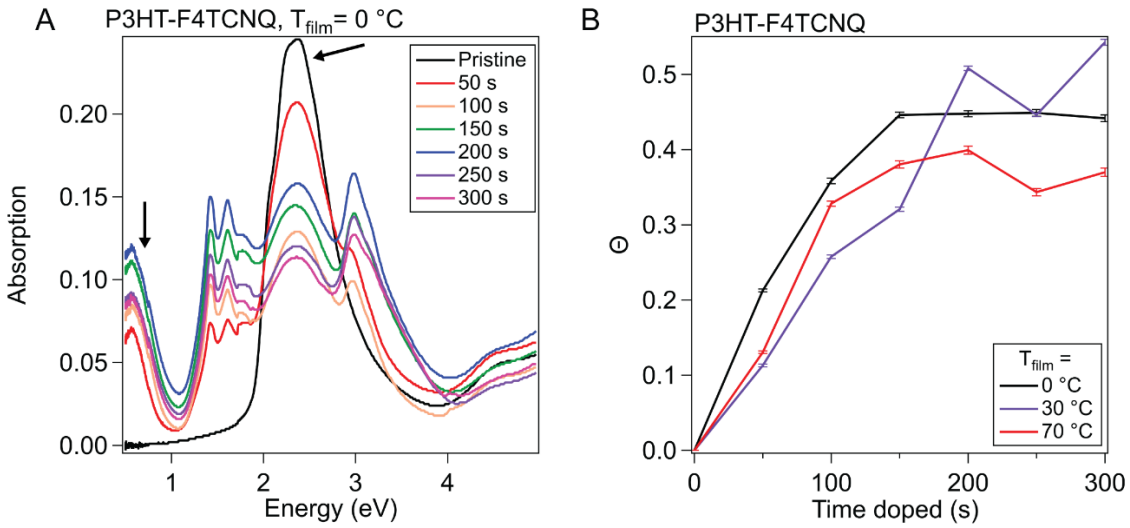

Figure 21. UV-Vis-NIR Absorption of P3HT and P3HT-F4TCNQ samples.
(A) Representative absorption spectra of P3HT-F4TCNQ films doped to the levels shown in figure 20 (0 s to 300 s at 50 s intervals), with sample temperature 0 °C. The peak at 0.5 eV is attributed to the polaron and the peak at 2.3 eV is attributed to the neutral P3HT. (B) Plotting the fraction of doped P3HT sites (Θ) versus the doping time. The value of Θ is correlated to charge carrier concentration.

As the amount of time doped increases, the neutral P3HT peak at 2.3 eV is bleached while the peaks attributed to the doped material increases.[40] It appears that the rise in Θ slows, then hits a maximum at the t_{max} in its corresponding *in situ* conductivity experiment (150 s or 200 s doped). After this maximum, Θ equilibrates or reduces slightly. All three T_{film} show similar values for Θ as well as the overall trend, which corresponds to their similarity for the *in situ* conductivity experiments.

FTIR spectra were also taken for these same doping times. These spectra can determine the nature of the charge transfer between the dopant and polymer; a set of peaks Neelamraju *et al.* indicated integer charge transfer or charge transfer complex mechanisms, the latter of which is a partial charge sharing.[16,17] These spectra can be seen in **Figure 22**. Peaks corresponding to integer charge transfer at 0.269 eV and 0.271 eV appear in the doped films; however, the presence of a

higher energy shoulder that indicates the presence of charge transfer complex formation appears in the 300 s doped P3HT in two of the temperatures. Previous studies have shown that the presence of charge transfer complexes, which have dopant between π-stacked backbones as opposed to the alkyl sidechain stacks, leads to a decrease in mobility.[22] This presence of a small concentration of charge transfer complex at high doping concentration, past σ_{max}, indicates that the drop in σ can be partly attributed to the decrease in mobility due to the formation of charge transfer complexes.[41]

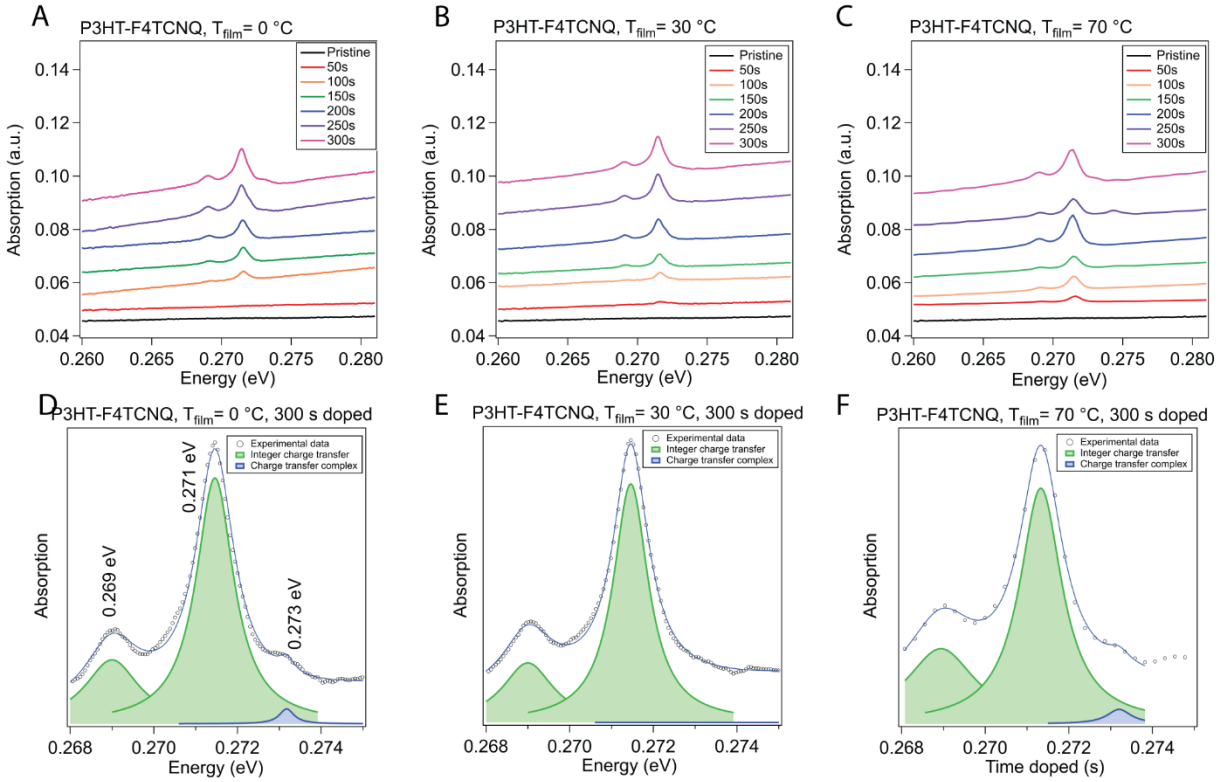

Figure 22. FTIR peak assignment and description.

(A), (B), and (C) show FTIR data for P3HT on KBr plates, vapor doped by F4TCNQ with the same method used for the *in situ* conductivity, UV Vis, and Raman experiments. These plots show the region indicated by Neelamraju *et al.* for P3HT doped at 0, 30, and 70 °C respectively,[17] peaks mostly attributed to integer charge transfer, with shoulder apparent in 250s and 300s doped showing emerging charge-transfer complex. These peaks are shown in (D), (E), and (F) for 0, 30, and 70 °C respectively.

2.3.6 Local molecular ordering of polymer closely correlates to σ

To provide more context to how the dopant situates and interacts with the ordered domains of the polymer film, we utilized grazing incidence wide angle x-ray scattering (GIWAXS). The molecular packing structure of P3HT is well documented, as well as its reaction to the infiltration of molecular dopant in both solution sequential and vapor sequential doping methods.[27,30,40] Qualities such as long-range ordering and the π-π stacking spacing are determinants on how efficiently charges can be conducted via inter- and intra-chain mechanisms; F4TCNQ has been shown to intercalate into the alkyl-stacking of the polymer during vapor doping, as well as reduce the π-π stacking spacing, increasing π-π orbital overlap and leading to better interchain conduction.[42]

2D GIWAXS scattering images from these experiments can be seen in **Figures 32, 33, and 34** for T_{film} = 0, 30 and 70 °C respectively. 1D scattering profiles were obtained via radial integration of the 2D scattering images, which are displayed in **Figure 23A, B & C**. The strong features primarily seen in the q_z direction that are equally spaced out correspond to the lamella-stacked side chains *(h00)*. The broad ring that stretches both in and out of the plane of scattering is the (020) peak, which is associated with the π-π stacking direction. In our analysis, resolving the individual peaks further out in reciprocal-space is difficult, so the maximum scattering spacing was used as an estimate of the average spacing distance. The alkyl sidechain stacking distance and the π-π stacking distance are plotted versus doping time in **Figures 23D & E**, respectively.

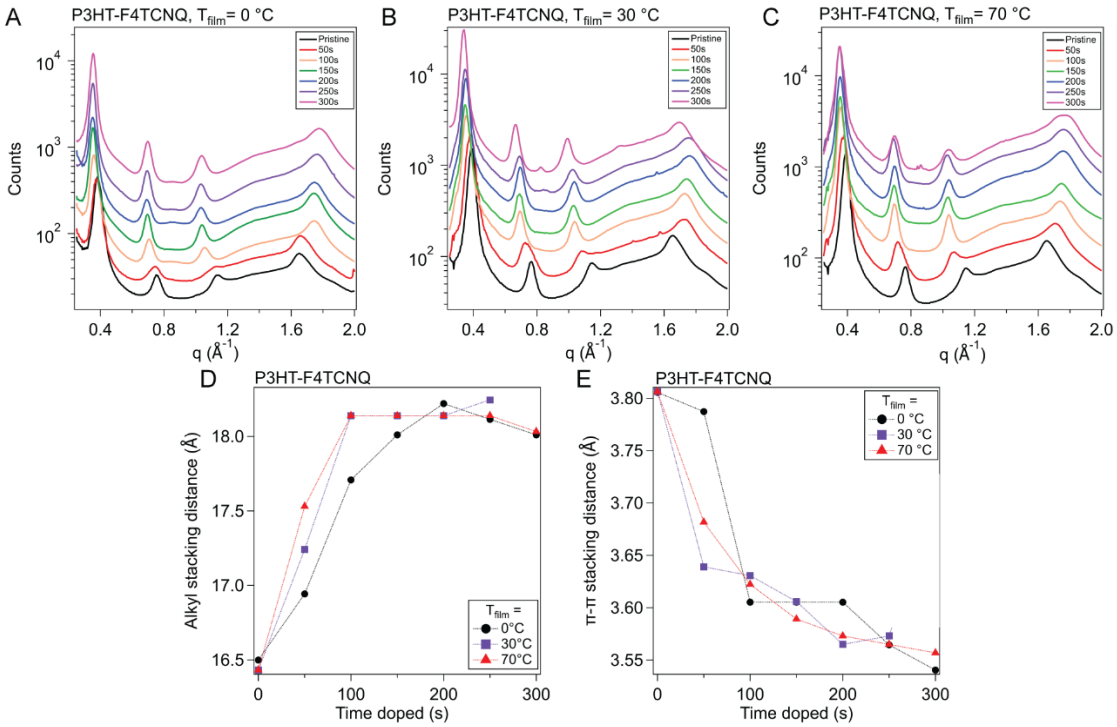

Figure 23. Evolution of ordered structures over the course of doping.

Grazing incidence wide angle x-ray scattering (GIWAXS) was conducted on P3HT vapor doped with F4TCNQ at 50 s intervals from 0 s to 300 s for all three sample temperatures. (A), (B), and (C) show the azimuthal linecuts of the scattering images, such as the ones seen in figure 32. (D) shows the evolution of the alkyl-stacking spacing, which are represented in the linecuts as the first three, equal spaced out peaks. The alkyl-stacking spacing appears to shift continuously until σ_{max} is reached at around 200 s, at which point the spacing appears to slightly decrease. This is likely due to the presence of dopant in the sidechains, which increases as doping time increases. (E) shows the π- π stacking, which is represented by the broad peak originating around 1.6 $Å^{-1}$ in the neat film. Similar to the alkyl stacking, the decrease in π-π stacking occurs similarly between all temperatures, which tails off as the film reaches σ_{max}. This decrease in π-π stacking spacing has been described in literature as due to electrostatic attractive forces between charged backbones, and increases the overlap of π orbitals, which in turn increases the probability of intrachain hopping of charge carriers.

Qualitatively, the scattering trends seen here are consistent to the reported results in literature. Upon doping, the sidechain/alkyl stacking and the π-π stacking distances do not drastically change;

the (*h00*) peaks' position decreases in reciprocal space, corresponding to a larger spacing between the sidechains. This increase in the alkyl stacking distance increases at a higher rate from the onset of doping to 150 s, dependent on T_{film}, which corresponds to t_{max} in our *in situ* experiments. Quantitatively, for the P3HT-F4TCNQ with T_{film} = 0 °C, the alkyl stacking spacing (d_{100}) changes from from 1.64 nm to 1.80 nm. Concurrently, the π-π stacking peak position increases in reciprocal space, indicating a decrease in packing spacing in the π-π direction. Although the spacing dropped quickly in the first 100 s of doping, the change in spacing slows down as the doping reaches σ_{max} as seen in the *in situ* conductivity experiment. For the P3HT-F4TCNQ at T_{film} = 0 °C, the π-π stacking spacing reduced from d_{020} = 0.381 nm to 0.355 nm over the course of 300 s vapor doping.

2.3.7 Resonance Raman spectroscopy of P3HT-F4TCNQ shows evolution of doping in ordered and amorphous domains

Raman spectra are very sensitive to π-electrons due to their polarizability under photoexcitation.[43,44] We use this phenomenon along with resonance Raman techniques to capture the evolution of various fractions of the polymer film. By using an excitation laser that matches the energy of the polaronic (charged) polymer, we can preferentially probe structural changes arising from these features.[45] This can be executed using a 785 nm laser (1.58 eV) that lines up with the second polaronic absorption and dopant anion peaks (see **Figure 29**).

The Raman spectra from the 785 nm excitation laser can be seen in **Figure 21A**. These spectra were obtained on P3HT-F4TCNQ films vapor doped in 50 s intervals, from neat to 300 s, at the three T_{film} as the *in situ* conductivity experiments. The spectra in these figures are focused on the 1300 to 1600 cm^{-1} range, which features peaks that correspond to the C=C intraring vibration modes which are sensitive to the charging of the conjugated thiophene backbone.

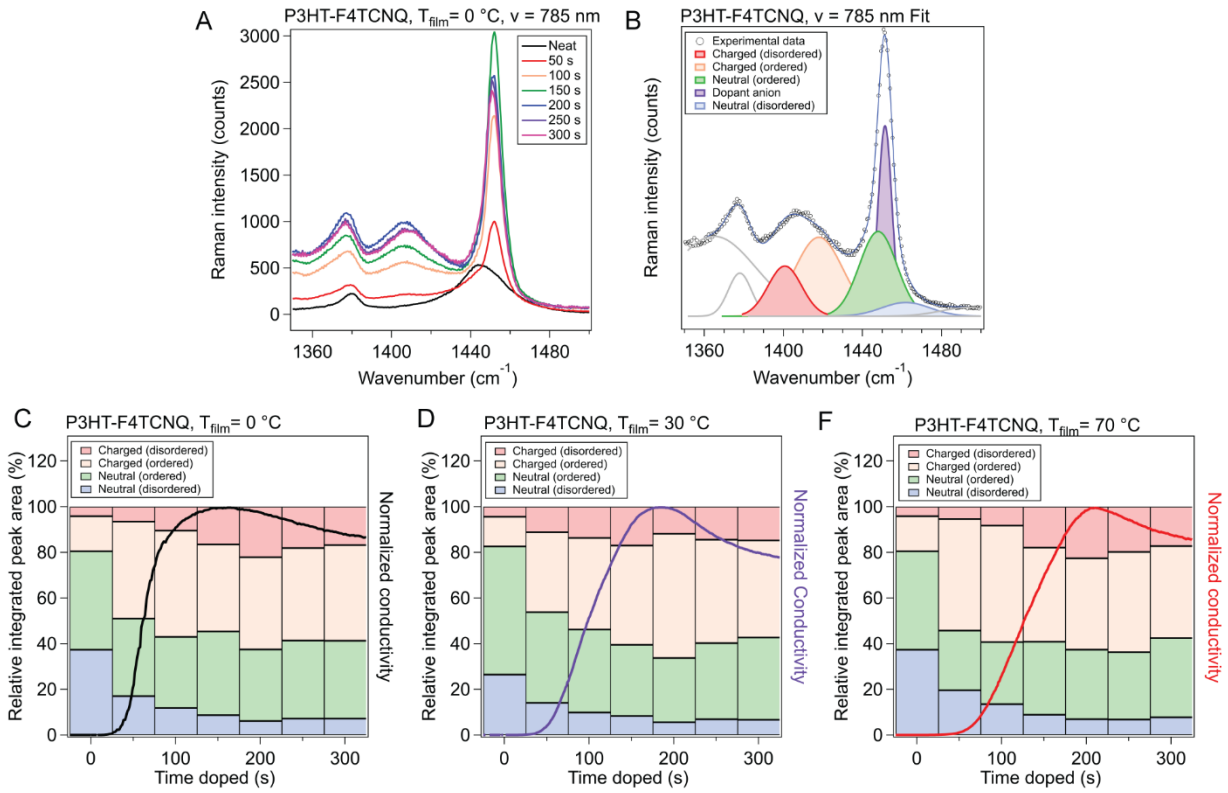

Figure 24. Raman spectra and peak fitting for P3HT-F4TCNQ samples doped to different levels. (A) Raman measurements were conducted on P3HT-F4TCNQ films doped to the levels shown in figure 20 (0 s to 300 s at 50 s intervals), using an excitation wavelength of 785 nm. (B) Peak fittings were made according to the methodology introduced in ref. 43. (C, D, E) The peak areas from the fittings were taken, and ratios of integrated peak area fitted were calculated, for T_{film} = 0, 30, & 70 °C respectively. The *in situ* σ curves for the respective T_{film} is overlayed for easier comparison. More detailed descriptions of the fitting methods are described prior to tables S1 through S4.

To accurately track the relative concentration of certain fractions over the course of doping, the spectra were fit to peaks that were described by Nightingale *et al*. Peaks corresponding to the C=C intraring vibration of the neutral fractions were centered around 1455 cm^{-1}, with a peak from the neutral, ordered domains around 1447 cm^{-1} and a peak from the neutral, disordered domains around 1462 cm^{-1}. Changes in peak position and shape were attributed to changes in conjugation length (*i.e.*, conformational order), with lower wavenumbers corresponding to longer conjugation

length (hence why the disordered polymer peak sits at a higher wavenumber than the ordered).[43] The peak widths and peak locations were given bounds to account for changes in the mean and distribution in conjugation lengths; these bounds were sourced from Nightingale *et al*.[43] Due to the resonance of the charged domains of the film, we can also resolve the charged ordered and charged disordered domains of the films, whose peaks sit at roughly 1417 cm^{-1} and 1401 cm^{-1}, respectively. These peaks were allowed to change in both peak width and position more widely, due to expected changes in the mean and standard deviation of conjugation lengths in the charged polymer as dopant infiltrated and interacted with the polymer film. A more detailed discussion of the fitting methodology, parameters, and data can be found alongside Tables S1 – S3 in the supporting information.

The relative integrated peak area from the fits of the 785 nm excited Raman for T_{film} = 0, 30, and 70 °C is plotted in **Figure 24C, D, and E** respectively. The relative integrated peak area was obtained by dividing the integrated area of the peak in question by all the peaks attributed to the polymer in its spectrum's fit; this was done in order to track the relative changes of each peak over the course of doping, dividing out the increase of the total absorption due to resonance with the polymeric polaron.

Due to the presence of the dopant anion peak (1451 cm^{-1}) over the neutral, ordered, and neutral, disordered peaks, we chose to focus our analysis primarily on the evolution of the charged, ordered and charged, disordered peaks. Comparing the ratio of charged peaks to neutral peaks (roughly correspondent to Θ in our UV-Vis-NIR analysis), the ratio is highest at t_{max} (~200 s), and decreases slightly from that maximum at higher doping times. However, the greatest increase in charged, ordered peak area comes from the step from the neat film to the 50 s doped film, whereas charged, disordered appears to increase steadily with time, with its maximum corresponding to t_{max} and the

highest ratio of charged to neutral peak area. The decrease in the ratio also appears to be primarily due to a loss in peak area for the charged, disordered peak, whereas the charged, ordered relative peak area stays relatively constant.

To recontextualize, these results indicate that the dopant first preferentially infiltrates and reacts with the ordered domains, which are energetically more favorable to interact with than the disordered domains. This rapid reaction with the ordered domain also corresponds with the exponential rise in conductivity, over five orders of magnitude, for the first 50 s. The slower, linear rise of conductivity can be attributed to the increase in charge concentration in the disordered domains, and the final stabilization to a lower σ also can be attributed to a loss of charge concentration in the disordered domains. From what was seen previously in the FTIR, it is possible that the presence of a high concentration of dopant in the disordered domain promotes a charge transfer complex in that domain, lowering its charge concentration.

These results show agreement with previous P3HT Raman literature. In a blend P3HT/PCBM film, Gao *et al.* show via 473 nm resonance Raman a broadening of the "aggregate P3HT" peak around 1450 cm^{-1} as F4TCNQ loading increases, which we would attribute to an increase in the charged ordered peak.[18] Chew *et al.* corroborate this finding using a 532 nm excitation focusing on the neutral aggregates, claiming an increase in conjugation length of the neutral aggregates with the presence of F4TCNQ dopant.[46] Lim *et al*. use an off-resonance laser wavelength of 633 nm that averages over the entire film, and show that both RR and RRa P3HT have a stiffening of the backbone with the presence of F4TCNQ.[27] This phenomenon was shown to also exist in polythiophenes with polar sidechains by Ma *et al*., where P3MEET shows a lower conjugation length than P3HT, but similarly stiffens in the presence of dopant.[47]

2.4 Conclusion

This study investigated vapor doping of P3HT with F4TCNQ in order to understand the evolution of conductivity *in situ* and the corresponding structural changes at the molecular level. The temporal profile of σ first exhibited a rapid exponential increase, followed by a short linear increase until reaching a σ_{max}, and finally followed by a slow decay in σ. While the profile and range of σ are comparable for each T_{film} (0, 30, 70 °C) investigated, t_{max} was achieved the fastest at T_{film} = 0 °C where the temperature difference between the T_{dopant} and T_{film} was the largest. For in situ conductivity experiments where the sample was doped to a specific time, the decay and stabilization of σ was dependent on the proximity to t_{max}. Specifically, samples doped close to and after t_{max} demonstrated the largest decay in sigma.

The characterization of the vapor doped P3HT thin films through UV-vis-NIR spectroscopy, FTIR spectroscopy, and GIWAXS provided complementary insight on the extent of doping. Analysis of the UV-vis-NIR spectra reveal the doping level (based on the fraction of doped sites, Θ), increases linearly until hitting a maximum near t_{max} in its corresponding *in situ* σ curve after which the doping level stabilized. Notably, analysis of the FTIR spectra indicated the formation of a small fraction of charge transfer complexes for doping times beyond t_{max} suggesting the decay in σ in this regime is partially arising from lower mobility charge carriers from charge transfer complexes. By monitoring d_{100} and d_{020} from the GIWAXS results showed the changes to these characteristic spacings from the infiltration of dopant anion in crystalline domains stabilizes near t_{max} of the in situ doping curve – consistent with the UV-vis-NIR data.

Resonant Raman spectroscopy experiments provided deeper insights on the relative extent of doping within the crystalline (ordered) and amorphous (disordered) domains and their connection the *in situ* conductivity profile. Specifically, at 785 nm, the spectra revealed relative fraction of

neutral ordered, charged ordered, neutral disordered, charged disordered components in the thin films. At 50 s, doping preferentially occurred in the ordered domains leading to a larger relative charged ordered fraction while only a small fraction of charge is formed in the amorphous domains. As the doping time was increased, the propensity of doping was still in the ordered domains and accounts for the rapid rise in sigma until approaching t_{max}. In the context of the in-situ conductivity profile, this corresponded to the transition point where the conductivity changes linearly and reaches σ_{max}. In this transition regime, the crystalline domains reached their saturated doping (charged) level and subsequent doping only occurred at sites in the disordered domains.

This method of comparing these characterization techniques to the *in situ*/*ex situ* σ curves has been fruitful in providing more granular insight into the processes of vapor molecular doping. Going forward, this platform is readily available for use for more novel polymer-dopant combinations. Further insight into how different sidechains or functional groups on the backbone effects the *in situ* σ, and how this is reflected in further characterization, will help to realize materials with better stability and higher σ with better understanding on how the polymer chemistry and structure affect the molecular doping process.

2.5 Experimental Methods

2.5.1 Materials and sample preparation

All substrates used for Grazing incidence wide angle X-ray scattering (GIWAXS), Raman spectroscopy, Atomic Force Microscopy (AFM) and UV-vis absorption spectroscopy in this study were cleaned by ultrasonication in acetone and 2-propanol for 15 minutes each. GIWAXS measurements were performed on films deposited on Si substrates with 1.5 nm of native SiO_2. UV-vis absorption, Raman measurements, and AFM were performed on films deposited on top of quartz substrates. Conductivity measurements were performed on films deposited on custom-

fabricated interdigitated gold electrodes (IDEs), which in turn is on Si substrates with 1000 nm of thermally-grown SiO_2. Solutions of 91% to 94% regioregular Poly(3-hexylthiophene-2,5-diyl) (RR-P3HT) (Rieke Metals) were prepared by dissolving P3HT in anhydrous chlorobenzene at 10 mg/mL. The mixed solutions were shaken overnight before being spun onto the prepared substrates. The substrates were spin coated with solution at 2000 rpm at 45 seconds, then at 3000 rpm for 25 seconds. IDEs were cleaned of excess polymer with cotton swabs to reduce leakage current.

2.5.2 *In situ* conductivity setup

For the *in situ* conductivity measurements, a specialized setup was fabricated for control and precision of measurement. A steady-state temperature is achieved using a thermoelectric module. The sample is held in place by two electrode probes, which allows for electrical contact with the sample during vapor doping. See figure 17 for a cross section of the setup, and figure 27 for a more detailed 3D rendering.

2.5.3 Vapor doping process

Vapor doping of F4TCNQ was performed in an argon-filled glovebox. Approximately 5 mg of dopant was pressed into a pellet and placed in an aluminum oxide crucible (OD 6.8 mm x H 4 mm from Government Scientific Source Inc.), which was in turn placed in a glass insert (diameter ~ 5 cm, height ~ 4.5 cm). A stainless-steel container is then preheated to allow the chamber to reach the desired temperature, which is monitored by thermocouple, and the glass insert is placed inside the container, at which point the setup is allowed to stabilize in temperature. A Teflon cap is placed upon the opening of the glass insert to block dopant from polluting the glovebox.

All samples used for doping were placed within the sample holder. Electrical contact was made to the sample through the sample holder, which was then routed via cables through the back of the

glovebox to a SP-200 Potentiostat. A voltage of 100 mV is applied to the sample, and the current through the sample is measured by the potentiostat every second. This data is converted from current to conductivity through the equation:

$$\sigma_{IDE} = \frac{1}{R}\frac{d}{l(N-1)h}$$

where d = 8 μm is the separation distance between the electrode digits, l = 150 μm is the length of the digits, N = 80 is the number of electrodes and h is the thickness of the sample.[48]

2.5.4 UV-Vis-NIR

UV-VIS-NIR spectra of neat P3HT and vapor-doped thin films on quartz substrates were obtained using the Shimadzu UV-3600 Plus UV-VIS-NIR Dual Beam Spectrophotometer housed in the Soft Matter Characterization Facility (SMCF) (Pritzker School of Molecular Engineering, University of Chicago). Measurements were taken within a wavelength range of 250 to 2480 nm.

2.5.5 FTIR & UV-Vis-NIR

FTIR and UV-Vis-NIR spectra of neat P3HT and vapor-doped thin films were made upon KBr plates within the Shimadzu IRTracer-100 Fourier Transform Infrared Spectrometer and the Shimadzu UV-3600 Plus UV-VIS-NIR Dual Beam Spectrophotometer housed in the Soft Matter Characterization Facility (SMF) (Pritzker School of Molecular Engineering, University of Chicago). UV-Vis-NIR measurements were taken within a wavelength range of 250 to 2480 nm, and FTIR measurements were taken with a wavelength range of 0.05 to 0.5 nm.

2.5.6 Raman spectroscopy

Raman spectroscopy experiments were performed under ambient conditions using the Horiba LabRAM HR Evolution NIR confocal Raman microscope housed in the Chicago Materials Research Center. Raman spectra of neat and doped P3HT thin films was collected using a 100× objective and a 785 nm wavelength laser. Laser power and was set to 10% for 785 nm lasers to

minimize local heating and material degradation. Spectra were taken between a wavenumber range of 1116 to 1771 cm^{-1}. For deeper insight into the peak fitting methodology, a detailed discussion can be found alongside Tables 1 – 4 in the appendix.

2.5.7 Grazing incidence wide angle X-ray scattering (GIWAXS)

GIWAXS experiments were conducted at the Advanced Photon Source (Argonne National Laboratory) at beamline 8-ID-E. The energy of the incident beam was at 10.91 keV, and a Pilatus 1MF pixel array detector (pixel size = 172 μm) was used.[49] The measurement time for one image was 10 seconds. All samples were placed and measured in a low vacuum chamber (10^{-3} mbar) to reduce the air scattering as well as to minimize beam radiation damage. There are multiple rows of inactive pixels between the detector modules when the images were collected at one position. To fill these inactive gaps, the detector was moved down to a pre-set new position along the vertical direction after each measurement. After the image was collected at the new spot, the data from these two detector positions were combined using the GIXSGUI package for MATLAB to fill the inactive gaps. The absence of artifacts in the combined image demonstrates that the scattering from the sample does not change during the exposure. The GIXSGUI package was also used to output the GIWAXS signals as intensity maps in (q_r, q_z) space, and take the linecuts along out-of-plane (q_z) and in-plane directions (q_r). GIWAXS images of thin films were taken at a grazing incident x-ray angle of 0.14°, which is above the critical angle of the polymer film and below the critical angle of the silicon substrate.

2.6 *Appendix*

2.6.1 Spano model fit of neat P3HT

The Spano model was used to make estimate of percent of aggregate versus amorphous fractions in the P3HT used in this study. The model dictates that the absorption spectra of P3HT

thin films in the ~2.0 eV to 3.0 eV range are comprised of low-energy π-stacking aggregate peaks and higher energy amorphous-fraction peaks. In order to determine the vibration bands for the aggregate portion, we utilize a Franck-Condon fit:

$$A_{\text{aggregate}} \propto \sum_{m=0} \left(\frac{S^m}{m!}\right) \times \left(1 - \frac{We^{-S}}{2E_p} \sum_{n \neq m} \frac{S_n}{n!\,(n-m)}\right)^2 \times e^{\left(E - E_0 - mE_p - \frac{1}{2}WS^m e^{-S}\right)^2 / 2\sigma^2}$$

Where *A* is the absorption of the aggregates as a function of photon energy, *E*; *S* is the Huang-Rhys factor, which represents the overlap between individual vibrational states (we assume this to be 1 for this fit); *m* corresponds to different vibrational energy levels; E_p = 0.179 eV the energy of the C=C symmetric branch mode in P3HT; the three fitting parameters are: *W*, the exciton bandwidth; E_0, the transition energy; and σ, the energetic disorder, which in this case is the Gaussian width of the absorption peaks. The peaks generated by this Franck-Condon fit can be seen in **Figure 25B**: the individual peaks are red with dotted lines, and the summation the solid red line, which appears to fit the shoulder from ~2.0 eV to 2.5 eV in the absorption well. The amorphous fraction was taken to be the higher energy region, obtained by subtracting the aggregate absorption calculated from the absorption from the experiment. The percent aggregate is calculated from this fit by taking the integrated area of the aggregate peaks to the amorphous peaks, and this was found for this fit to be roughly 37%. A Matlab fit program was used to perform the Spano fit as described by Dong *et al*.[50]

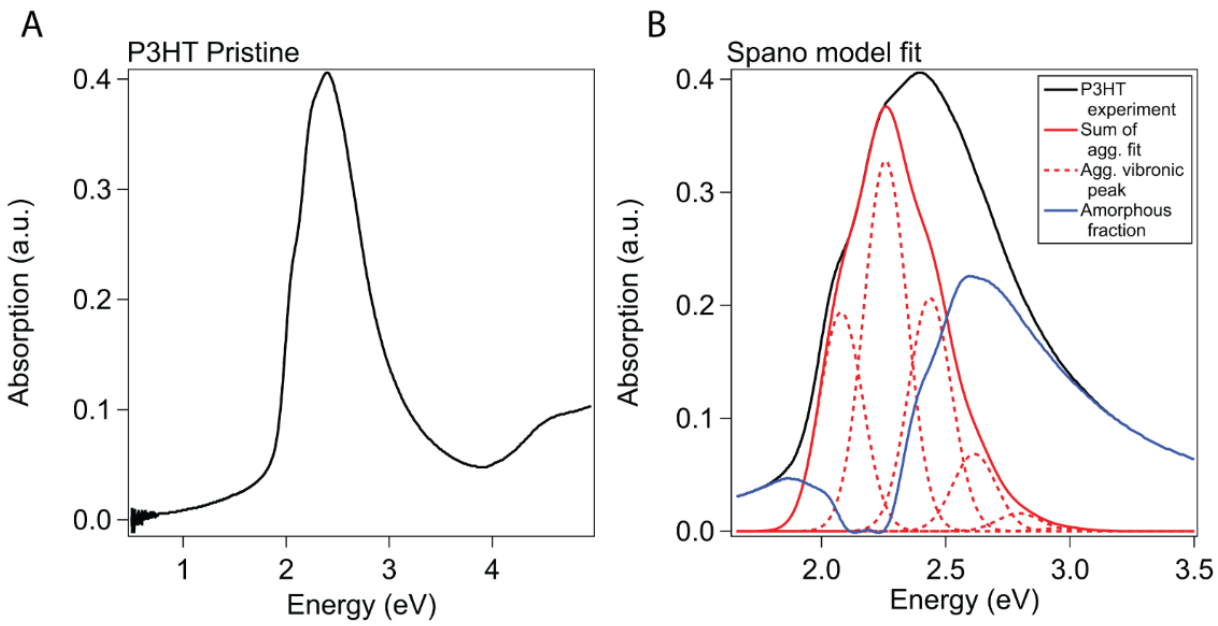

Figure 25. Pristine P3HT UV-Vis absorption fit with Spano model.
(A) UV-Vis-NIR of neat P3HT thin film. (B) Spano model fit.

2.6.2 Cyclic voltammetry of P3HT and F4TCNQ

Cyclic voltammetry (CV) was performed using a Biologic SP200 potentiostat in as standard 3-electrode configuration. Testing was performed in an anhydrous, degassed acetonitrile solution with a 0.1 M tetrabutylammonium hexafluorophosphate supporting electrolyte concentration at a scan rate of 0.1 V/s. A silver wire in 0.01 M $AgNO_3$ and 0.1 M supporting electrolyte served as a reference electrode, and a platinum wire was used as a counter electrode. Ferrocene purified by sublimation was used as an internal standard. All experiments were performed in a dry argon glove box. F4TCNQ was dissolved directly in acetonitrile at 0.01 M concentration. P3HT was spin coated onto an ITO-coated glass slide according to the procedure described in the experimental methods section. Ionization energy (IE, HOMO) of the polymers and electron affinity (EA, LUMO) of the dopants were determined by comparison against the ferrocene couple (5.1 eV), as described here:

$$IE = q(E_{ox} + 5.1 - E_{F,ox})$$

$$EA = q(E_{red} + 5.1 - E_{F,red})$$

where q is the fundamental charge of an electron, E_{red} is the reduction potential of F4TCNQ, and $E_{F,red}$ is the oxidation potential of ferrocene. Onset potentials were calculated by regressing the rising slope of the oxidation peak to the intersection point of the system background current. The linear regression and background current are seen straight lines in the CV plot for P3HT. F4TCNQ's LUMO level was calculated by this method to be 5.25 eV, and the HOMO for P3HT was calculated by this method to be approximately 5.1 eV.

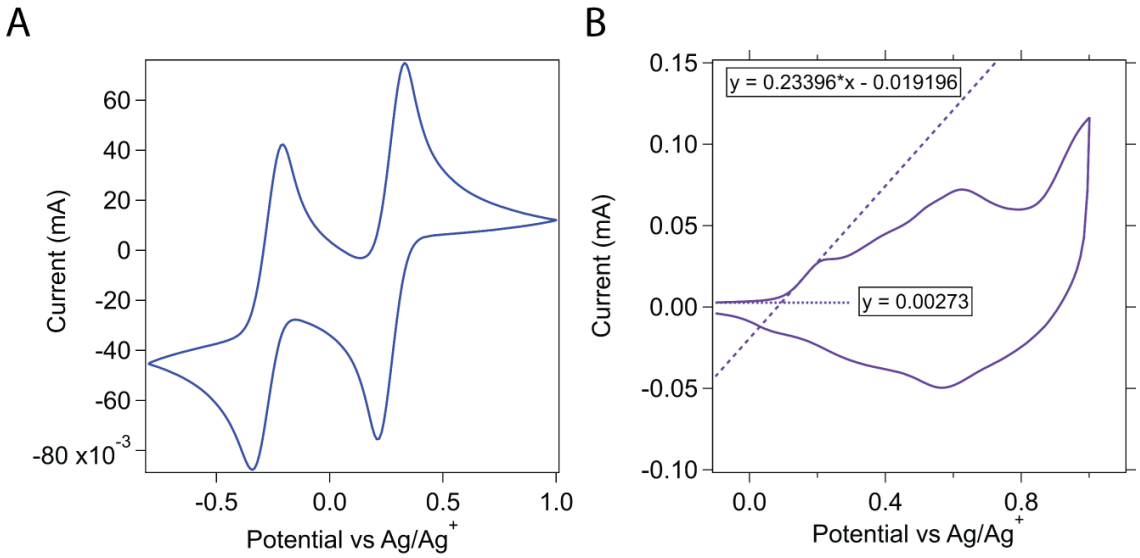

Figure 26. (A) CV of F4TCNQ. (B) CV of P3HT.

2.6.3 Vapor doping setup and experimental details

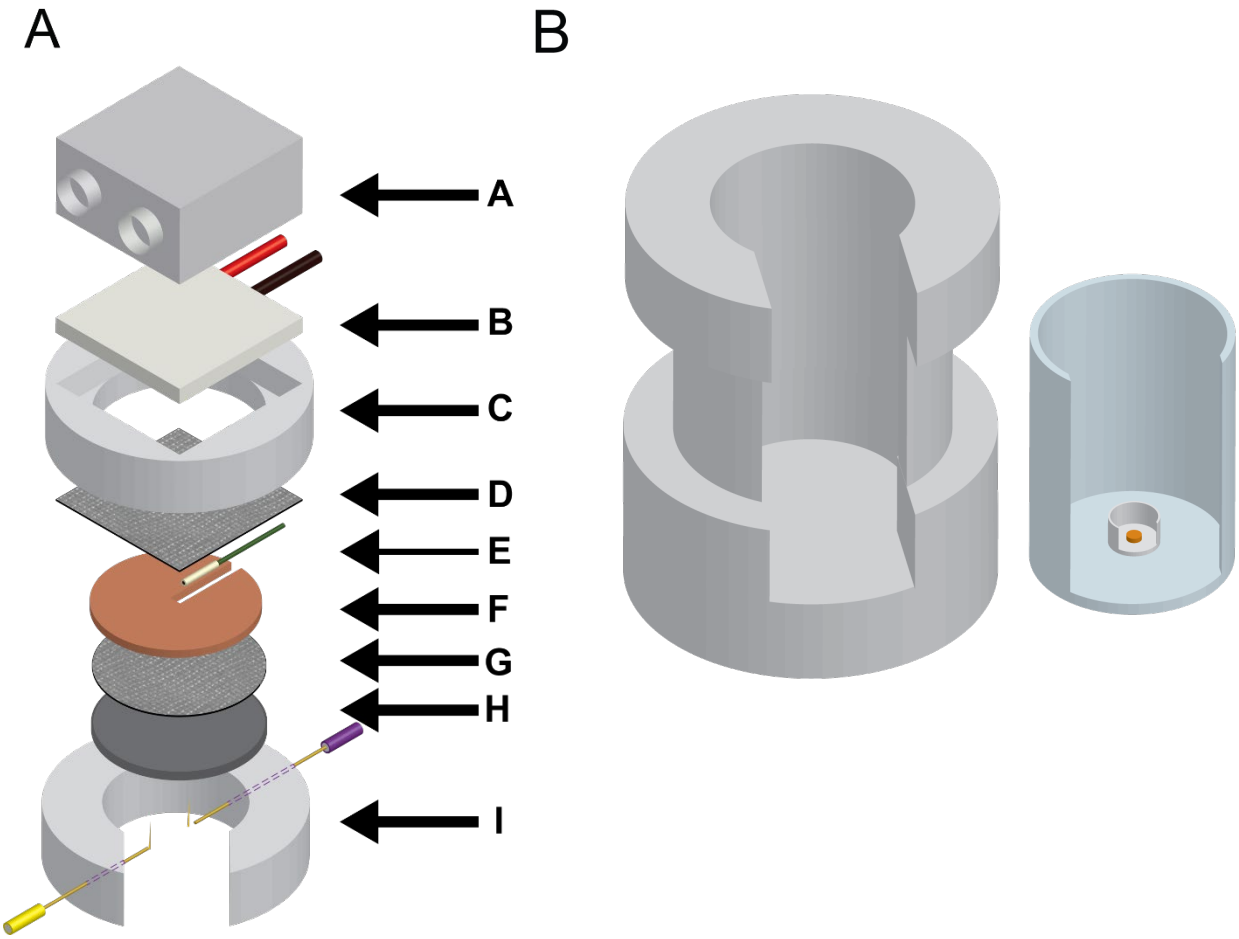

Figure 27. 3D renders of sample holder and doping chamber.

For sample holder (11A): A- aluminum water-cooling block. B- Peltier thermoelectric module. C- Peltier module housing. D- thermally conductive adhesive. E- thermistor for monitoring sample temperature. F- copper heat spreader. G- thermally conductive adhesive. H- silicon wafer sample base. I- retention ring with retaining electrode probes. For doping chamber (11B), a stainless steel chamber (left) jackets a quartz glass insert (right), which holds an alumina crucible with dopant pellet in a recess. A thermocouple in the base of the doping chamber measures the temperature of the doping chamber, allowing for control over the doping temperature.

2.6.4 UV-Vis-NIR

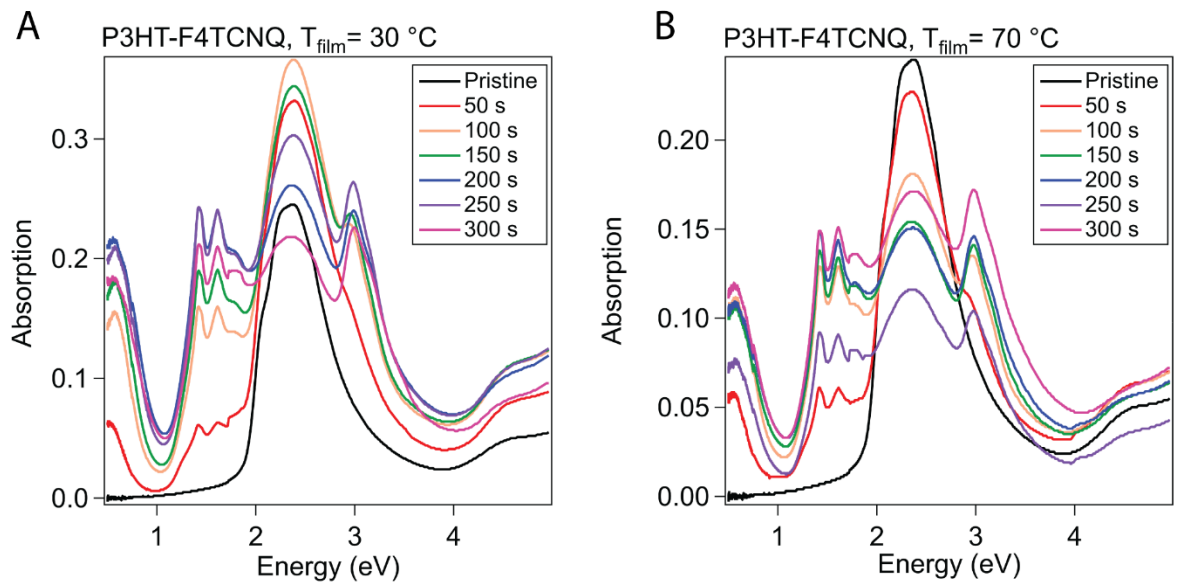

Figure 28. Absorption of P3HT-F4TNQ at 30 °C and 70 °C.

Absorption measurements were conducted on P3HT-F4TCNQ films doped to the levels shown in fig. 3 (0 s to 300 s at 50 s intervals). (A) shows the spectra for films doped with the film held at 30 °C, and (B) at 70 °C.

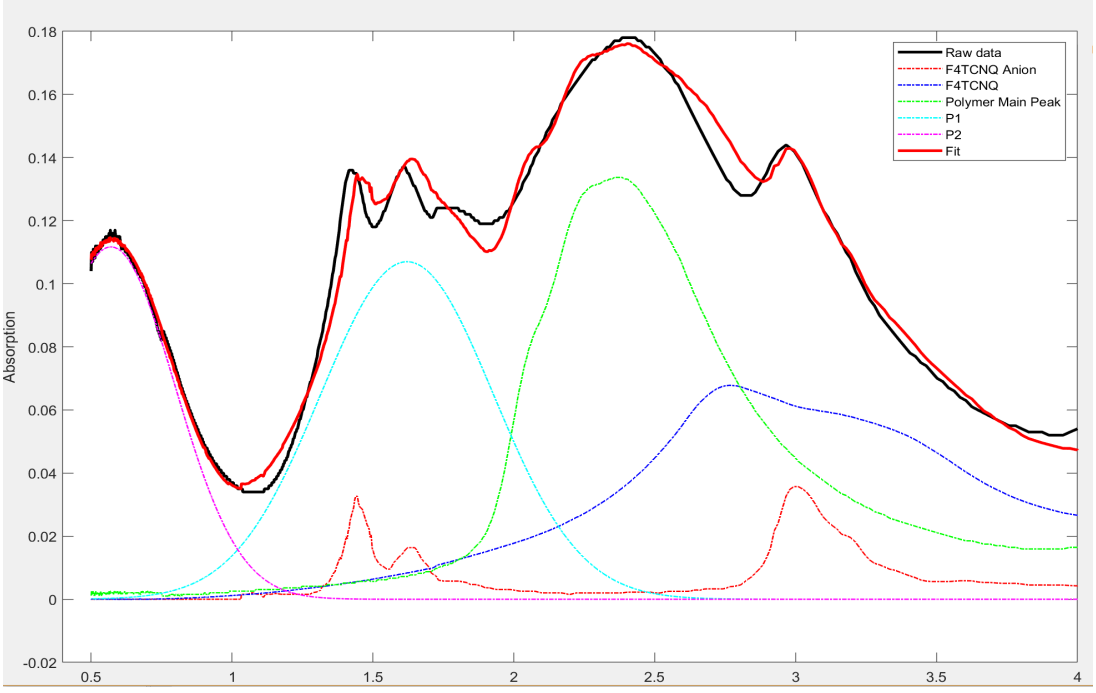

Figure 29. Fit of UV-Vis absorption.

(Figure 29. Fit of UV-Vis continued) Description of peaks adapted from Hynynen, Kiefer and Müller.[51] F4TCNQ anion, polaron peaks 1 and 2 were taken from the same paper. The F4TCNQ neutral peak was obtained from our own absorption measurements on vapor-deposited F4TCNQ. The ratio between the fitted polaron 1 peak (labeled P1 here) and the polymer neutral peak (labeled polymer main peak here) is what is used in fig. 5 in the main manuscript.

2.6.5 Raman spectroscopy and fitting

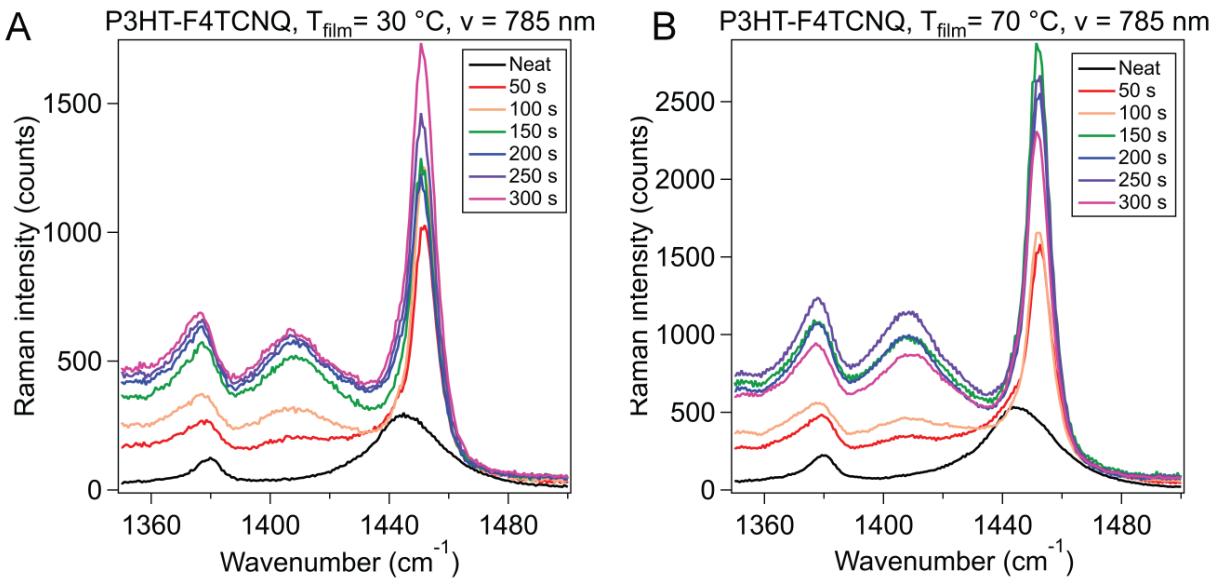

Figure 30. Raman spectra of P3HT-F4TCNQ excited by 785 nm laser @ 0 and 70 °C.
Raman spectra collected on P3HT doped to films doped with F4TCNQ from 0 s to 300 s at 50 s intervals. Films were doped at (A) 0 °C and (B) 70 °C, and excited by 785 nm laser.

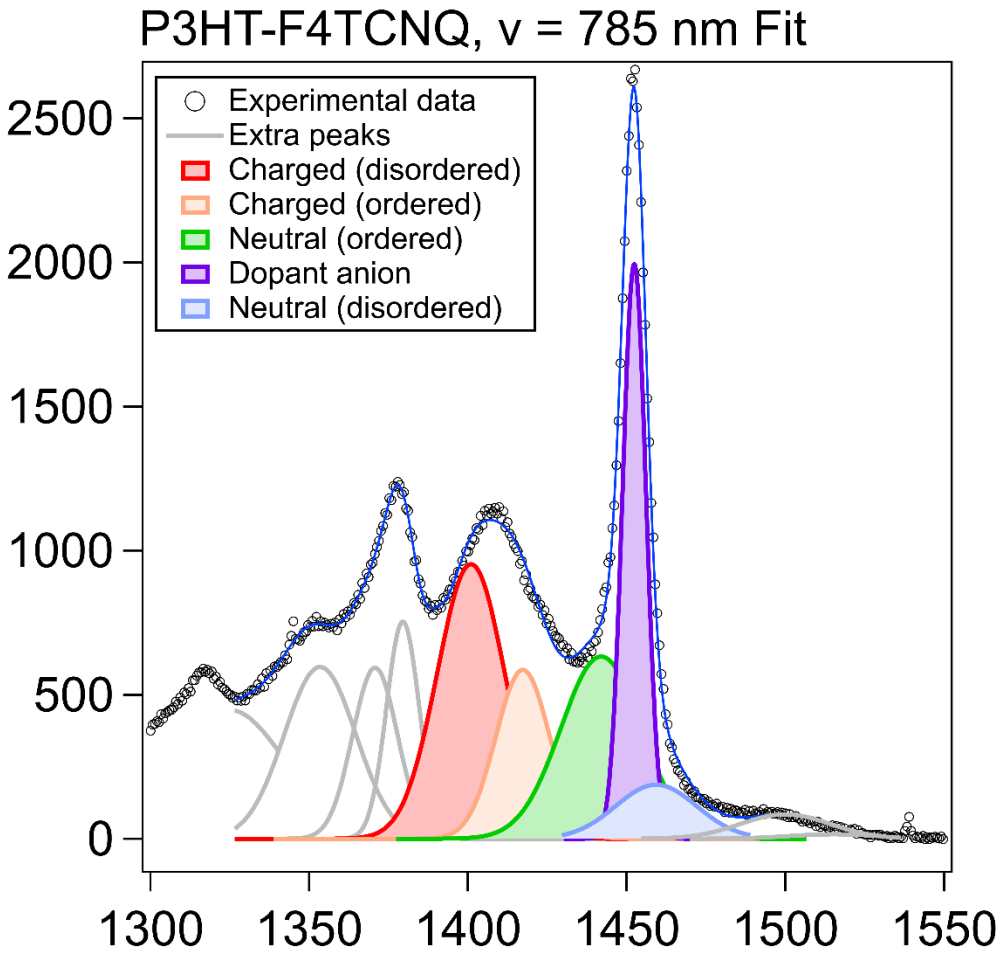

Figure 31. Wider view of 785 nm excitation Raman peak fitting.

A broader view of the peak fitting done for a 785 nm excitation Raman spectrum. Peaks colored in were used for the analysis seen for the bar graphs in figure 24. Grey peaks were included to fit the rest of the data and allow for accurate tracking of the peaks of main interest.

Discussion of Raman spectrum deconvolution and analysis

Our analysis centers on deconvolution of the main C=C stretching peaks in the region from 1400 cm^{-1} to 1460 cm^{-1}, which we attribute first to the work of Nightengale et al., but also point towards work by Degousée et al. and Dyson et al. as exemplary works utilizing this style of analysis.[43,52,53] In particular, we utilize the fact that the C=C symmetric stretch shifts to shorter

wavelength for chains with a higher conjugation length. Although this order is probed at the level of a bond on an individual chain, domains in P3HT are such that there are crystalline domains with a higher proportion of long-conjugation length chains, and amorphous domains with a greater proportion of low conjugation length chains, and hence we take ratio of higher conjugation length chains to lower conjugation length chains as a measure of how ordered or disordered the material is as a whole.

When we excite the film for Raman spectroscopy using a 785 nm laser, we preferentially excite the charged regions of the film, as this wavelength/energy corresponds to the P2 absorption in the UV Vis (as seen in fig. S6). This resonance strengthens the contribution to the Raman spectrum from the charged parts of the films and allows for deconvolution of the charged C=C stretching peak seen at a slightly lower wavenumber, around 1410 to 1420 cm^{-1}, into charged ordered and charged disordered populations. The lower peak center wavenumber compared to the neutral portions of the film is due to a higher planarity of the polymer upon introduction of charge carriers into the system; the fact that the disordered charged phase has a peak centered around a lower wavenumber is due to a larger change in bond length locally around the charge carrier in the amorphous (disordered) domain than the ordered domain.

When taken as a whole, we argue that fitting the C=C symmetric peak as deconvoluted into charged disordered (~1401 cm^{-1}), charged ordered (~1420 cm^{-1}), neutral ordered (~1447 cm^{-1}), and neutral disordered (~1462 cm^{-1}) Gaussian peaks allows us to track the evolution of doping within the ordered and amorphous phases of our polymer separately. We achieve this by fitting and tracking how these peaks change over the course of our timepoints, from the undoped film to films doped 300 s by F4TCNQ.

In order to accurately track the evolution of these peaks, we use the peak positions and FWHM suggested by Nightingale et al. for these modes, but set constraints of roughly ±3 cm^{-1} to ±5 cm^{-1}, dependent on the variance in peak positions reported for P3HT by Nightingale *et al.* and Degousée *et al.* We believed that constraining the FWHM, rather than fixing, would also represent the changing population of conjugation lengths in the individual phases more accurately. The FWHM for all C=C modes were constrained between 0 and 50 cm^{-1}, except for the charged disordered phase, which was constrained between 0 and 20 cm^{-1}, to fit how these peaks were constrained prior by Degousée et al.

F4TCNQ anion was also confirmed to have a peak present within the range that we were deconvolution for peaks, sharply resolved at around 1452 cm^{-1}. This peak was fit in order to be able to accurately deconvolute those peaks resulting from the polymer and that of the dopant.

The window of the Raman spectra that were fit roughly spanned from 1250 cm^{-1} to 1600 cm^{-1}. Gaussians with FWHM between 0 and 20 cm^{-1} that were given a constraint on location in a range of 20 cm^{-1} were fit in order to account for all Raman counts between the fit range and produce accurate fit data for the four main peaks, including the C-C stretching around 1380 cm^{-1}. The peak locations and areas under the curve for the four C=C modes are included comprehensively in the tables below for this analysis, and can be seen in **Figure 31** for an example fitting.

P3HT-F4TCNQ excited by 785 nm		
Peak origin	Peak Location (cm^{-1})	FWHM (cm^{-1})
Charged, disordered fraction	1399 - 1405	20
Charged, ordered fraction	1415 - 1425	28 - 38
Neutral, ordered fraction	1442 - 1447	22
Dopant anion	1451 - 1453	5 - 8
Neutral, disordered fraction	1455 - 1462	23 - 35

Table 1. Approximate peak location and widths for Raman fits with both excitation lasers.

Peak locations for the ordered and disordered fractions of P3HT that were charged and neutral, listed in the table above, were used for the fits in the tables below as starting points. These peaks can be seen labeled in in **Figure 21B & E**. These peak locations and widths were sourced from a similar analysis done by Nightingale *et al*.[43]

P3HT-F4TCNQ 0 °C										
	Charged Disordered		Charged Ordered		Neutral Ordered		Dopant Anion		Neutral Disordered	
Time doped (s)	Peak location (cm^{-1})	Area	Peak location (cm^{-1})	Area	Peak location (cm^{-1})	Area	Peak location (cm^{-1})	Area	Peak location (cm^{-1})	Area
0	1399	849	1421	3124	1445	8804	N/A	N/A	1455	7613
50	1402	1426	1426	9282	1448	7418	1452	4452	1462	3716
100	1401	3939	1418	17565	1448	11713	1452	12643	1462	4480
150	1400	7501	1418	17240	1448	16607	1452	19226	1462	3946
200	1401	11383	1418	20765	1448	16104	1452	15516	1462	3166
250	1401	9412	1418	21027	1448	17768	1451	14431	1462	3748
300	1401	8646	1418	21592	1448	17570	1451	13810	1462	3713

Table 2. Fit of Raman spectra for P3HT-F4TCNQ excited by 785 nm at 0 °C

P3HT-F4TCNQ 30 °C										
	Charged Disordered		Charged Ordered		Neutral Ordered		Dopant Anion		Neutral Disordered	
Time doped (s)	Peak location (cm^{-1})	Area	Peak location (cm^{-1})	Area	Peak location (cm^{-1})	Area	Peak location (cm^{-1})	Area	Peak location (cm^{-1})	Area
0	1405	466	1424	1363	1445	5882	N/A	N/A	1462	2779
50	1401	1987	1421	6226	1448	7065	1452	5548	1462	2498
100	1400	2810	1418	8212	1448	7446	1452	7534	1462	2027
150	1401	4869	1418	12464	1448	8958	1451	7028	1462	2384
200	1404	3800	1418	17375	1448	8986	1451	6460	1462	1786
250	1401	4946	1418	15501	1448	11410	1451	7956	1462	2364
300	1401	5380	1418	15484	1448	13116	1451	9815	1462	2434

Table 3. Fit of Raman spectra for P3HT-F4TCNQ excited by 785 nm at 30 °C.

P3HT-F4TCNQ 70 °C										
	Charged Disordered		Charged Ordered		Neutral Ordered		Dopant Anion		Neutral Disordered	
Time doped (s)	Peak location (cm^{-1})	Area	Peak location (cm^{-1})	Area	Peak location (cm^{-1})	Area	Peak location (cm^{-1})	Area	Peak location (cm^{-1})	Area
0	1399	849	1421	3124	1445	8804	N/A	N/A	1455	7613
50	1399	1900	1419	17045	1448	9123	1453	8345	1462	6847
100	1401	2683	1419	16482	1448	8792	1452	9769	1462	4378
150	1401	9834	1418	22668	1448	17533	1452	17262	1462	4892
200	1403	11449	1419	20304	1448	15440	1452	15663	1462	3516
250	1402	11606	1418	25765	1448	17284	1452	15923	1462	3971
300	1401	8614	1418	20075	1448	17337	1452	12929	1462	3863

Table 4. Fit of Raman spectra for P3HT-F4TCNQ excited by 785 nm at 70 °C.

2.6.6 Grazing incidence wide angle X-ray scattering (GIWAXS) data

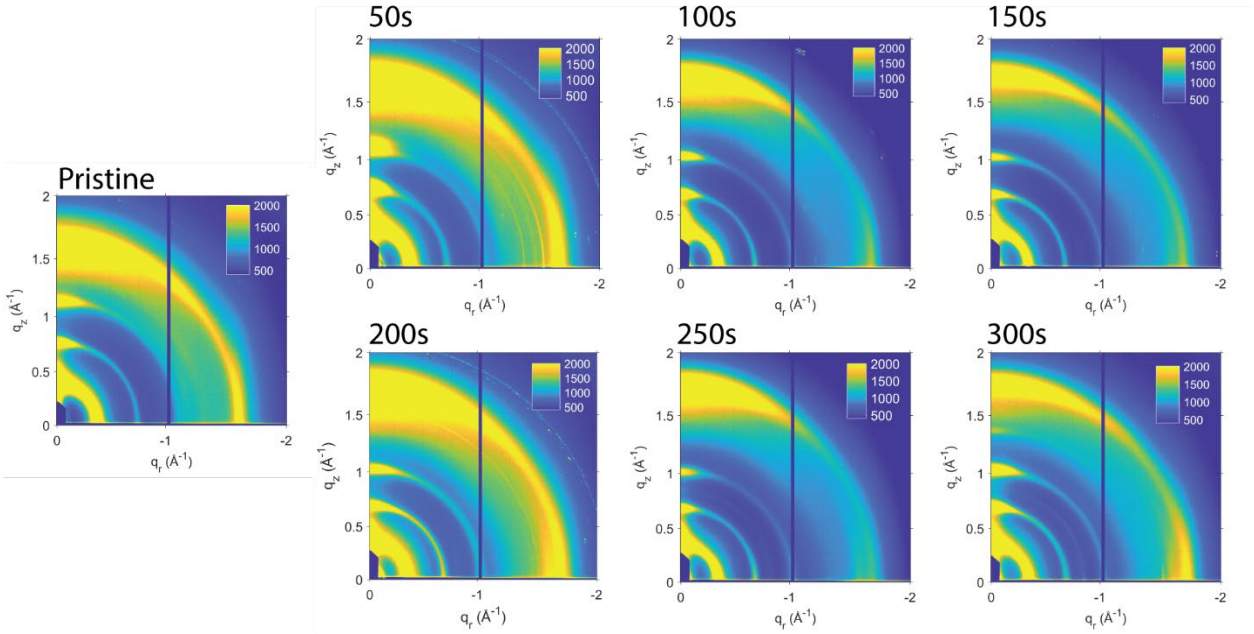

Figure 32. P3HT-F4TCNQ scattering, doped at 0 °C.

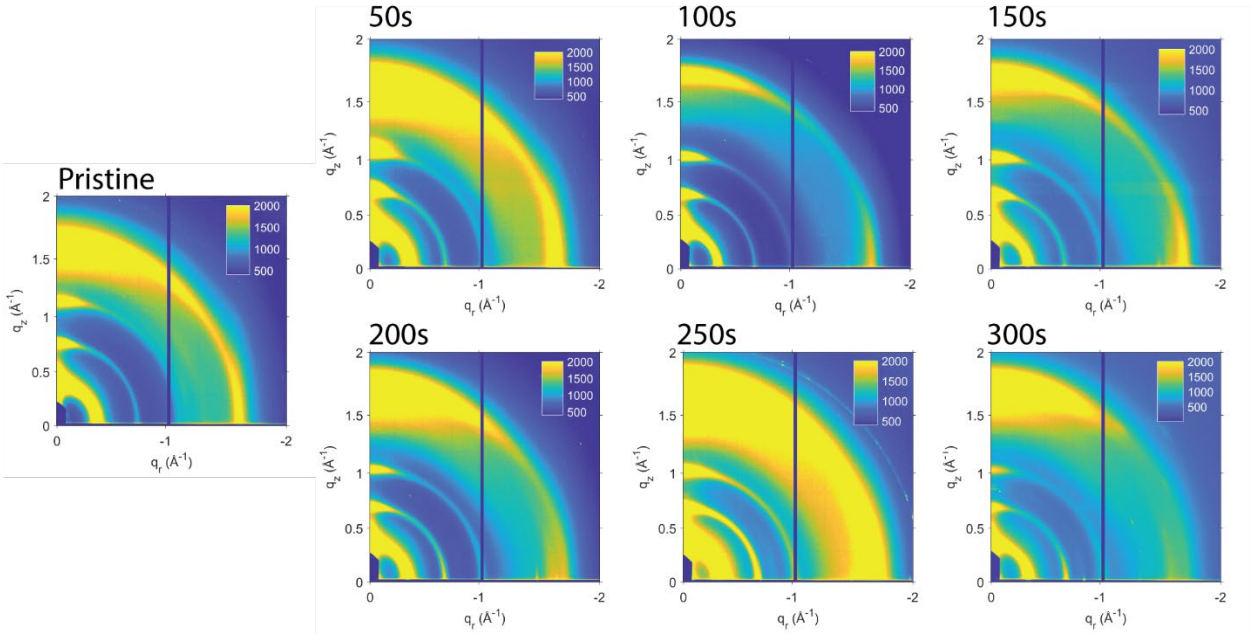

Figure 33. P3HT-F4TCNQ scattering, doped at 30 °C.

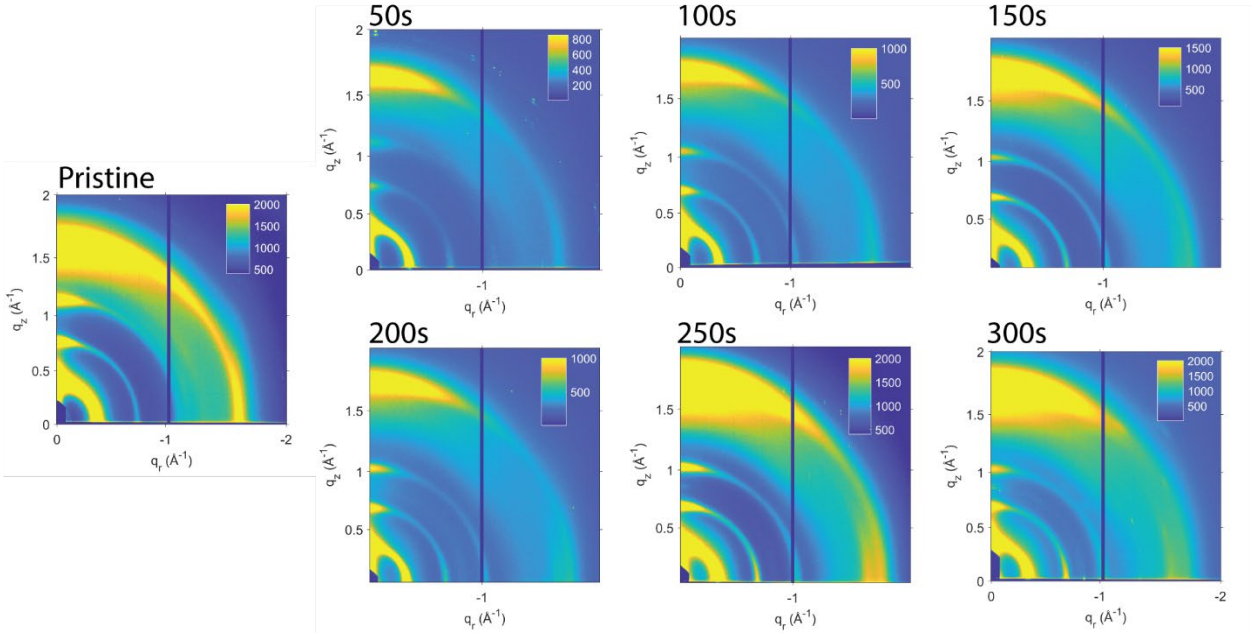

Figure 34. P3HT-F4TCNQ scattering, doped at 70 °C.

2.7 Acknowledgments

This work was primarily supported by the University of Chicago Materials Research Science and Engineering Center, which is funded by National Science Foundation under award number

DMR-1420709. M.D. acknowledges support from the National Science Foundation through the National Science Foundation Graduate Research Fellowship under grant no. DGE-1746045. This research used resources of the Advanced Photon Source, an Office of Science User Facility operated for the U.S. Department of Energy (DOE) by Argonne National Laboratory under Contract No. DE-AC02-06CH11357. Parts of this work were carried out at the Soft Matter Characterization Facility of the University of Chicago.

2.8 References

1. I. E. Jacobs, E. W. Aasen, J. L. Oliveira, T. N. Fonseca, J. D. Roehling, J. Li, G. Zhang, M. P. Augustine M. Mascal and A. J. Moulé, J. Mater. Chem. C, 2016, 4, 3454–3466.
2. D. T. Scholes, S. A. Hawks, P. Y. Yee, H. Wu, J. R. Lindemuth, S. H. Tolbert and B. J. Schwartz, J. Phys. Chem. Lett., 2015, 6, 4786–4793.
3. S. N. Patel, A. M. Glaudell, K. A. Peterson, E. M. Thomas, K. A. O'Hara, E. Lim and M. L. Chabinyc, Sci. Adv., e1700434.
4. I. E. Jacobs and A. J. Moulé, Adv. Mater., 2017, 29, 1703063.
5. P. Y. Yee, D. T. Scholes, B. J. Schwartz and S. H. Tolbert, J. Phys. Chem. Lett., 2019, 10, 4929–4934.
6. D. T. Scholes, P. Y. Yee, J. R. Lindemuth, H. Kang, J. Onorato, R. Ghosh, C. K. Luscombe, F. C. Spano, S. H. Tolbert and B. J. Schwartz, Adv. Funct. Mater., 2017, 27, 1702654.
7. S. N. Patel, A. M. Glaudell, D. Kiefer and M. L. Chabinyc, ACS Macro Lett., 2016, 5, 268–272.
8. M. S. AlSalhi, J. Alam, L. A. Dass and M. Raja, Int. J. Mol. Sci., 2011, 12, 2036–2054.
9. J.-H. Bahk, H. Fang, K. Yazawa and A. Shakouri, J. Mater. Chem. C, 2015, 3, 10362–10374.
10. L. Huang, Z. Hu, J. Xu, K. Zhang, J. Zhang, J. Zhang and Y. Zhu, Electrochim. Acta, 2016, 196, 328–336.
11. R. Meerheim, C. Körner and K. Leo, Appl. Phys. Lett., 2014, 105, 063306.
12. T. Ma, B. X. Dong, G. L. Grocke, J. Strzalka and S. N. Patel, Macromolecules, 2020, 53, 2882–2892.
13. S. D. Kang and G. J. Snyder, Nat. Mater., 2017, 16, 252–257.
14. D. Venkateshvaran, M. Nikolka, A. Sadhanala, V. Lemaur, M. Zelazny, M. Kepa, M. Hurhangee, A. J. Kronemeijer, V. Pecunia, I. Nasrallah, I. Romanov, K. Broch, I. McCulloch, D. Emin, Y. Olivier, J. Cornil, D. Beljonne and H. Sirringhaus, Nature, 2014, 515, 384–388.
15. P. Pingel and D. Neher, Phys. Rev. B, 2013, 87, 115209.

16. K. E. Watts, B. Neelamraju, E. L. Ratcliff and J. E. Pemberton, Chem. Mater., 2019, 31, 6986–6994.

17. B. Neelamraju, K. E. Watts, J. E. Pemberton and E. L. Ratcliff, J. Phys. Chem. Lett., 2018, 9, 6871–6877.

18. J. Gao, J. D. Roehling, Y. Li, H. Guo, A. J. Moulé and J. K. Grey, J. Mater. Chem. C, 2013, 1, 5638.

19. S. Olthof, W. Tress, R. Meerheim, B. Lüssem and K. Leo, J. Appl. Phys., 2009, 106, 103711.

20. I. Salzmann, G. Heimel, M. Oehzelt, S. Winkler and N. Koch, Acc. Chem. Res., 2016, 49, 370–378.

21. D. Kiefer, R. Kroon, A. I. Hofmann, H. Sun, X. Liu, A. Giovannitti, D. Stegerer, A. Cano, J. Hynynen, L. Yu, Y. Zhang, D. Nai, T. F. Harrelson, M. Sommer, A. J. Moulé, M. Kemerink, S. R. Marder, I. McCulloch, M. Fahlman, S. Fabiano and C. Müller, Nat. Mater., 2019, 18, 149–155.

22. O. Zapata-Arteaga, B. Dörling, A. Perevedentsev, J. Martín, J. S. Reparaz and M. Campoy-Quiles, Macromolecules, 2020, 53, 609–620.

23. T. J. Aubry, K. J. Winchell, C. Z. Salamat, V. M. Basile, J. R. Lindemuth, J. M. Stauber, J. C. Axtell, R. M. Kubena, M. D. Phan, M. J. Bird, A. M. Spokoyny, S. H. Tolbert and B. J. Schwartz, Adv. Funct. Mater., 2020, 30, 2001800.

24. R. Noriega, J. Rivnay, K. Vandewal, F. P. V. Koch, N. Stingelin, P. Smith, M. F. Toney and A. Salleo, Nat. Mater., 2013, 12, 1038–1044.

25. C. Wang, D. T. Duong, K. Vandewal, J. Rivnay and A. Salleo, Phys. Rev. B, 2015, 91, 085205.

26. J. Hynynen, D. Kiefer, L. Yu, R. Kroon, R. Munir, A. Amassian, M. Kemerink and C. Müller, Macromolecules, 2017, 50, 8140–8148.

27. E. Lim, A. M. Glaudell, R. Miller and M. L. Chabinyc, Adv. Electron. Mater., 2019, 5, 1800915.

28. P. Carbone and A. Troisi, J. Phys. Chem. Lett., 2014, 5, 2637–2641.

29. M. T. Fontana, D. A. Stanfield, D. T. Scholes, K. J. Winchell, S. H. Tolbert and B. J. Schwartz, J. Phys. Chem. C, 2019, 123, 22711–22724.

30. E. Lim, K. A. Peterson, G. M. Su and M. L. Chabinyc, Chem. Mater., 2018, 30, 998–1010.

31. K. Kang, S. Watanabe, K. Broch, A. Sepe, A. Brown, I. Nasrallah, M. Nikolka, Z. Fei, M. Heeney, D. Matsumoto, K. Marumoto, H. Tanaka, S. Kuroda and H. Sirringhaus, Nat. Mater., 2016, 15, 896–902.

32. C. Poelking and D. Andrienko, Macromolecules, 2013, 46, 8941–8956.

33. C. Scharsich, R. H. Lohwasser, M. Sommer, U. Asawapirom, U. Scherf, M. Thelakkat, D. Neher and A. Köhler, J. Polym. Sci. Part B Polym. Phys., 2012, 50, 442–453.

34. J. Gierschner, Y.-S. Huang, B. Van Averbeke, J. Cornil, R. H. Friend and D. Beljonne, J. Chem. Phys., 2009, 130, 044105.

35. R. Xie, Y. Lee, M. P. Aplan, N. J. Caggiano, C. Müller, R. H. Colby and E. D. Gomez, Macromolecules, 2017, 50, 5146–5154.

36. H. Shirakawa, E. J. Louis, A. G. MacDiarmid, C. K. Chiang and A. J. Heeger, J. Chem. Soc. Chem. Commun., 1977, 578.

37. S. Sweetnam, K. R. Graham, G. O. Ngongang Ndjawa, T. Heumüller, J. A. Bartelt, T. M. Burke, W. Li, W. You, A. Amassian and M. D. McGehee, *J. Am. Chem. Soc.*, 2014, **136**, 14078–14088.

38. K.-H. Yim, G. L. Whiting, C. E. Murphy, J. J. M. Halls, J. H. Burroughes, R. H. Friend and J.-S. Kim, Adv. Mater., 2008, 20, 3319–3324.

39. T. L. Murrey, M. A. Riley, G. Gonel, D. D. Antonio, L. Filardi, N. Shevchenko, M. Mascal and A. J. Moulé, J. Phys. Chem. Lett., 2021, 12, 1284–1289.

40. H. Méndez, G. Heimel, S. Winkler, J. Frisch, A. Opitz, K. Sauer, B. Wegner, M. Oehzelt, C. Röthel, S. Duhm, D. Többens, N. Koch and I. Salzmann, Nat. Commun., 2015, 6, 8560.

41. I. E. Jacobs, C. Cendra, T. F. Harrelson, Z. I. Bedolla Valdez, R. Faller, A. Salleo and A. J. Moulé, Mater. Horizons, 2018, 5, 655–660.

42. X. Shen, V. V. Duzhko and T. P. Russell, Adv. Energy Mater., 2013, 3, 263–270.

43. J. Nightingale, J. Wade, D. Moia, J. Nelson and J.-S. Kim, J. Phys. Chem. C, 2018, 122, 29129–29140.

44. Y. Sun, M. Palma and M. Brinkmann, 2021, 16065–16075.

45. J. Wade, S. Wood, D. Beatrup, M. Hurhangee, H. Bronstein, I. McCulloch, J. R. Durrant and J. Kim, J. Chem. Phys., 2015, 142, 244904.

46. A. R. Chew, R. Ghosh, Z. Shang, F. C. Spano and A. Salleo, J. Phys. Chem. Lett., 2017, 8, 4974–4980.

47. T. Ma, B. X. Dong, J. W. Onorato, J. Niklas, O. Poluektov, C. K. Luscombe and S. N. Patel, J. Polym. Sci., 2021, 59, 2797–2808.

48. D. Sharon, P. Bennington, C. Liu, Y. Kambe, B. X. Dong, V. F. Burnett, M. Dolejsi, G. Grocke, S. N. Patel and P. F. Nealey, J. Electrochem. Soc., 2018, 165, H1028–H1039.

49. Z. Jiang, X. Li, J. Strzalka, M. Sprung, T. Sun, A. R. Sandy, S. Narayanan, D. R. Lee and J. Wang, J. Synchrotron Radiat., 2012, 19, 627–636.

50. B. X. Dong, J. A. Amonoo, G. E. Purdum, Y.-L. Loo and P. F. Green, ACS Appl. Mater. Interfaces, 2016, 8, 31144–31153.

51. J. Hynynen, D. Kiefer and C. Müller, *RSC Adv.*, 2018, **8**, 1593–1599.

52. T. Degousée, V. Untilova, V. Vijayakumar, X. Xu, Y. Sun, M. Palma, M. Brinkmann, L. Biniek and O. Fenwick, J. Mater. Chem. A, 2021, 9, 16065–16075.

53. M. J. Dyson, E. Lariou, J. Martin, R. Li, H. Erothu, G. Wantz, P. D. Topham, O. J. Dautel, S. C. Hayes, P. N. Stavrinou and N. Stingelin, Chem. Mater., 2019, 31, 6540–6547.

Chapter 3: Impact of Doping Strength using Fluorinated TCNQ Derivatives on Conductivity and Structure of Vapor Doped P3HT

3.1 Abstract

Dopant selection within molecular doped polymer semiconductors has been shown to greatly affect the creation of charge carriers, based upon the ionization energy of the polymer relative to the electron affinity of the dopant for p-type dopants. However, how dopant strength controls the vapor molecular doping process is unclear. Here, we utilize an *in situ* conductivity method to track the σ as our polymer thin film is exposed to a gradually higher concentration of dopant, where our dopants are selected to have a similar physical profile and a spectrum of electron affinities. These *in situ* σ experiments were then compared to polymer thin film samples that were doped to 50 s interval timepoints, which were studied via microscopy and spectroscopy. We find that the proximity of the dopant's electron affinity to the polymer's aggregate and amorphous domains' ionization energy determines the ability for the dopant to react and create charge carriers in the respective domains of the polymer film. We also note that the larger charge carrier concentration introduced by the strongest dopant reduces the π-π stacking distance, which is conducive to better electronic mobility, and hence conductivity. We also find that one dopant showed a process unique from the other dopants that was dependent on the temperature of the polymer film and was more dramatic at higher film temperatures. We posit that these results allow for better control on how the dopant interacts with the polymer. We also believe that this methodology highlights how the molecular doping process intricately depends on the relation between the polymer and dopant, and that similar studies with novel polymer-dopant pairings will help uncover polymer chemistries and polymer-dopant interactions that can control desired electronic properties.

3.2 Introduction

Precise control of the electronic properties of conjugated polymer films is desired to promote their use within organic electronic devices. One such benchmark electronic property is conductivity (σ), which quantitatively can be calculated using the equation $\sigma = nq\mu$, where n is the concentration of charge carriers, q is the charge of the charge carrier (in this case, just the charge of the electron), and μ is the mobility of the charge carrier. Qualitatively, this means that conductivity is dependent on the concentration of charge carriers and their ability to move throughout the system.

Conjugated polymers recently have been a popular target of organic semiconductor studies due to their favorable properties for electronic conduction.[1–10] Conjugation, which is defined by alternating single and double bonds along the molecular backbone, allows for a resonant, "quinoid" form which helps delocalize charge carriers intrachain. Conjugated backbones are also rigid (to which the quinoid form contributes), which encourages aggregation and ordering. Domains of high aggregation are surrounded by amorphous domains, which have poor μ, and must be bridged by a "tie chain" from one aggregate domain to another to maintain an efficient pathway for charge carriers throughout the system.[11] In short, both short range, intra-domain order and long range, inter-domain order is important for conjugated polymers to maintain high μ.

As for increasing charge carrier concentration within conjugated polymers, charge carriers are typically introduced by an interaction between the polymer backbone and a molecular dopant.[12–14] For p-type (positive charge carrier) doping, the offset between the highest occupied molecular orbital (HOMO) of the polymer and the lowest unoccupied molecular orbital (LUMO) drives the transfer of a charge from the polymer to the dopant, introducing a hole as the charge carrier within the system.[15] Molecular doping is a delicate process. The efficiency of the charge transfer is

dependent on the concentration of dopant,[16,17] and introducing high concentrations of molecular dopant may also introduce electronic roadblocks for the charge carriers it creates to move around the system.[16,18–20]

There has been a lot of work attempting to control the molecular doping process to preserve or even enhance the μ of the charge carrier within the underlying polymer structure. One particularly powerful technique is known as sequential doping, which is the process of introducing the molecular dopant into an already-cast polymer film, which tends to preserve the polymer's carefully-selected high-μ structure better than mixing the dopant and polymer together in solution (known as "solution doping"), and leads to higher σ.[21–24] This has been achieved using a "sequential solution doping" method, where dopant in solution was placed on top of an already-cast polymer thin film, and allowed to diffuse in,[21] as well as via a "vapor sequential doping" method, where dopant was sublimated and diffused into the film in vapor form.[3,25–28] Furthermore, there is evidence that vapor sequential doping induces order in previously more amorphous parts of the polymer, resulting in better μ in these previously low μ parts of the film.[26] However, there remained untapped potential for granular control of the sequential doping process to tune for specific electronic properties.

Using sequential doping, we have previously designed a study to better understand the interaction between polymer and dopant, both structurally and electronically, in order to control our final electronic properties. We wished to see how poly(3-hexylthiophene) (P3HT) is affected by the process of vapor doping with a molecular dopant, for which we used 2,3,5,6-tetrafluoro-7,7,8,8-tetracyanoquinodimethane (F4TCNQ). Using an *in situ* σ experiment to elucidate how electronic conduction properties changed granularly, we then took that understanding to probe how the change of σ reflected how F4TCNQ interacted with the aggregate and amorphous domains of

P3HT separately. As a result of this study, we felt that this suite of techniques was a powerful characterization tool that could be used to probe how the molecular doping process could be understood and controlled to produce optimal electronic properties. However, we also felt that there were outstanding questions. How would different dopants change the shape of the *in situ* σ curve? How does the strength of the dopant affect how the aggregate and amorphous regions of the polymer are interacted with?

There have been also studies investigating how the interaction between the polymer and the molecular dopant drives the charge concentration, charge species, and even thermoelectric properties.[29–32] Kiefer *et al.* showed that they could introduce more than one charge per dopant molecule, given clever choice of molecular dopant whose LUMO was much lower than the polymer's HOMO, leading to a dianionic dopant.[13] Patel *et al.* demonstrated that doping PBTTT, a conjugated polymer with a lower HOMO, demonstrated similar σ between doping with F4TCNQ and its weaker cousin F2TCNQ, but a stronger thermoelectric power factor for the weaker dopant.[33] Recently, Dong *et al.* found that doping poly 3-(methoxyethoxyethoxy) thiophene (P3MEET) with tetracyanoquinodimethane (TCNQ) and its fluorinated derivatives resulted in σ of the same magnitude due to good HOMO-LUMO overlap, whereas the higher HOMO poly(3-(methoxyethoxyethoxymethyl)thiophene) (P3MEEMT) resulted in decreasing σ with increasing LUMO level.[34]

This study aims to use F4TCNQ's less-fluorinated cousins, TCNQ and its fluorinated derivatives (FNTCNQ, N = 1, 2, 4) to probe how dopant strength affects our structure-transport properties. As demonstrated with Dong *et al.* above, these organic dopants' LUMO can be easily tuned by changing the number of Fluorine atoms.[34,35] In combination with Raman & UV-Vis-NIR spectroscopy, and grazing incidence wide angle X-ray scattering (GIWAXS), we show how the *in*

situ σ curve's shape and amplitude corresponds to the creation and location of charge carriers in the polymer thin film, and how the strength of the interaction between polymer and dopant drives these properties.

3.3 Results and Discussion

3.3.1 Neat P3HT thin film fabrication and properties

Thin films of P3HT were fabricated through a spin coating method (see Methods section for details). A single processing condition was applied in this study to ensure consistent properties of pre-cast films for vapor doping: thin films were spin coated from a chlorobenzene solution and subsequently heated at 100 °C to drive out residual solvent. The resultant P3HT thin films had a thickness of 48 ± 5 nm based on AFM. In **Figure 42A** we show the UV-Vis-NIR spectrum of the neat P3HT thin film. Analysis of the spectrum using the Spano model revealed the degree of the crystalline order is 37%; this result is discussed in detail in the supporting information. Additionally, a cyclic voltammetry measurement, as seen in **Figure 43**, indicates that the onset potential of the aggregate domain is 0.09 V vs Fc/Fc^+ and, thus an ionization energy of -5.11 eV, as well as amorphous domains with ionization energies of -5.30 eV and -5.52 eV.

3.3.2 Molecular dopant characterization and comparison

P3HT thin films in this study were vapor doped using the "apparatus for controlled vapor-doping experiments" described in chapter 2. Dopants used in this study were tetracyanoquinodimethane (TCNQ) and its fluorinated derivatives, named for the number of fluorenes substituted for hydrogens (F1TCNQ, F2TCNQ, and F4TCNQ). We will describe these dopants collectively as "FNTCNQ" throughout this paper. These dopants were selected for their range of lowest-unoccupied molecular orbital (LUMO) energy levels. This was calculated using cyclic voltammetry to be -4.91, -5.01, -5.09, and -5.28 eV for TCNQ, F1TCNQ, F2TCNQ, and

F4TCNQ respectively. This range results in varying strengths of interaction with P3HT, which is driven by the overlap between the dopant LUMO and the polymer's highest-occupied molecular orbital (HOMO), known as the HOMO-LUMO overlap. We conducted our own cyclic voltammetry (CV) measurements on dopant, whose results can be seen in **Figure 35**, and whose data can be seen directly in **Figure 43**.

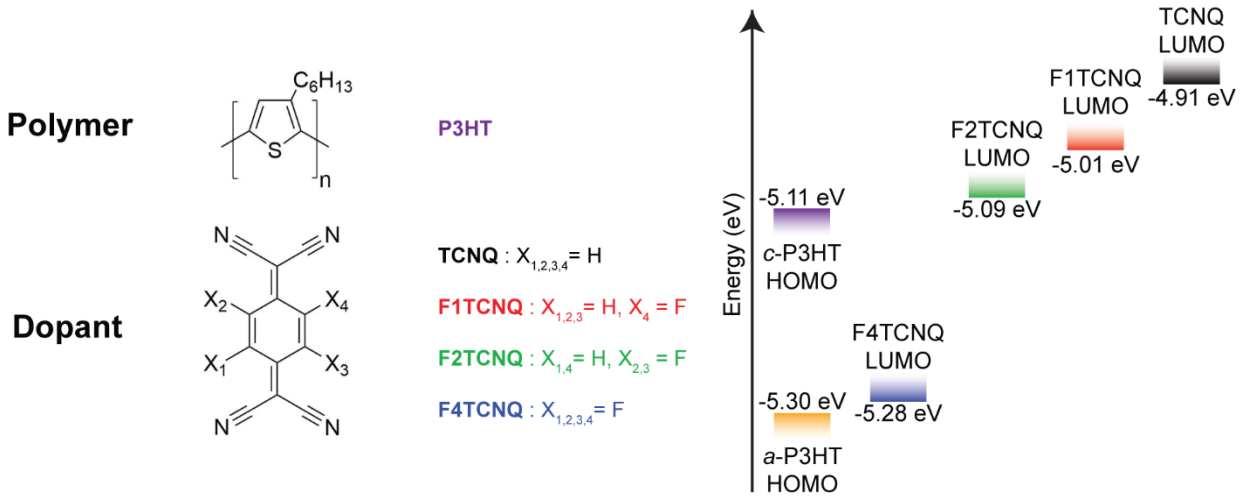

Figure 35. Polymer and dopant structure and energy levels.

The polymer-dopant pairing used in this work is Poly(3-hexylthiophene-2,5-diyl) (P3HT) with tetracyanoquinondimethane (TCNQ) and its fluorinated derivatives (FNTCNQ), whose structures are displayed above. The electronic levels of the P3HT highest-occupied molecular orbital (HOMO) for both the crystalline/aggregate (*c*) and the amorphous (*a*) domains, and dopant lowest-unoccupied molecular orbital (LUMO), calculated from CV seen in figure 43, are also shown.

3.3.3 P3HT-FNTCNQ *in situ* conductivity highlights difference in strengths of dopants

To characterize the process of vapor doping P3HT with FNTCNQ, we used an *in situ* conductivity (σ) measurement while utilizing our apparatus for controlled vapor doping experiments. The temperature of the polymer film, T_{film}, was held at 30 °C for all experiments, and T_{dopant} was held at temperatures that resulted in a similar sublimation rate as measured by thermogravimetric analysis, which can be seen in **Figure 44**. We used an interdigitated electrode

device to track the σ of the thin film over six orders of magnitude. For these experiments, σ was tracked for at least 20 minutes under positive dopant pressure, at which point all curves had established a stable trend.[34]

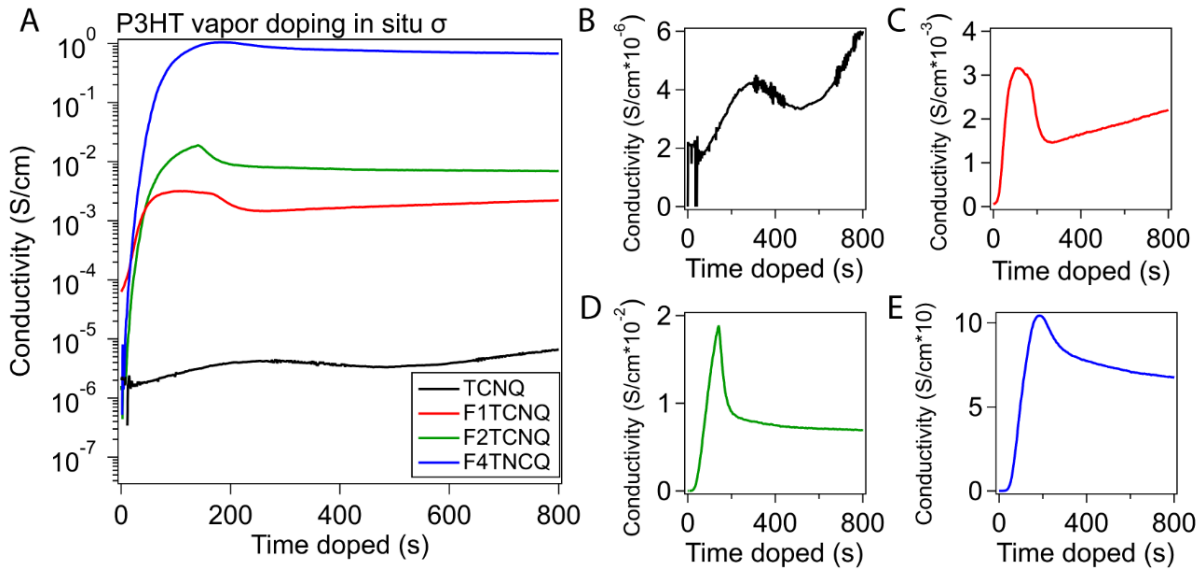

Figure 36. *In situ* σ of FNTCNQ-doped P3HT.

The σ for P3HT is shown during *in situ* σ experiments doping with FNTCNQ for T_{film} = 30 °C. (A) A semilog view of P3HT doped with all four dopants, which details the rapid rise of P3HT once dopant is introduced and starts diffusing into the film. (B-E) A linear view of the doping curve, which details the σ_{max} and the drop of the σ post maximum.

Representative curves for *in situ* σ using all four dopants can be seen in **Figure 36**. The magnitude of the σ appears to track well to the listed LUMO of the dopant. P3HT doped with F4TCNQ reaches ~1 S/cm, F2TCNQ ~10^{-2} S/cm, F1TCNQ ~5 × 10^{-3}, and TCNQ ~10^{-6} (barely doping it at all from its

inherent σ). All three dopants, besides the almost completely non-reactive TCNQ, appear to have the same basic structure to the σ curve. There is a period of exponential increase in σ, which then leads to a linear rate of increase. As the maximum σ is reached (σ_{max}), the rate slows, and then turns negative as the curve settles to a lower, final σ. Although the timing and exact shape of the

curve is dependent on the dopant, the main difference only appears to be the σ_{max} that is reached, which is orders of magnitude different between dopants. To explain why these magnitudinal differences in σ appear, it's worth looking more deeply into the HOMO-LUMO overlap concept when it comes to this polymer and these dopants.

Although P3HT's HOMO is calculated here as -5.11 eV, this most accurately describes those polymer chains within the aggregate domains of the polymer.[36–38] Chains within some of the amorphous domains of the polymer can be described with a HOMO of -5.29 eV (there is a second type of amorphous domain with a HOMO of -5.52 eV, see **Figure 43**). This distinction is crucial. On its face, this indicates three different regimes of ability to interact with the polymer: able to conduct charge transfer with both amorphous and aggregate domains, able to conduct charge transfer with only the aggregate domains, and unable to conduct charge transfer with either. This method of analysis puts F4TCNQ into the first camp (albeit only a small fraction of the amorphous domain), F2TCNQ in the second, and F1TCNQ and TCNQ in the third.

It is, however, worth noting that this is a rudimentary (yet still effective) way of describing the interaction between the P3HT thin film and FNTCNQ molecules. Previous studies have shown that the effective HOMO and LUMO of the polymer and dopant, respectively, is dependent on its surroundings. For the polymer, this manifests most clearly here in the different listed HOMO for the aggregate and amorphous domains; the surroundings of a thiophene unit that could interact with a dopant, whether it is tightly packed with other chains or around other disordered chains, affects whether it is energetically favorable to interact. The dopant, too, has a LUMO that is modified by being present in the film, rather than the controlled solution on which the CV is conducted. The main effect of this is that the HOMO and LUMO energy levels listed in **Figure 35** are suggestions rather than hard values. Only F2TCNQ theoretically should be able to have a

spontaneous charge transfer from P3HT's aggregate domains but not the amorphous domains, but a smaller fraction of F1TCNQ should achieve a charge transfer than for F2TCNQ, due to the distribution of HOMOs around the value calculated via CV.

This analysis describes the differences in σ as seen in the *in situ* σ experiments well. F2TCNQ and F1TCNQ's σ are much closer in magnitude than F2TCNQ to F4TCNQ, or F1TCNQ to TCNQ. The change in LUMO by -0.08 eV between F2TCNQ and F1TCNQ places it above the listed value of P3HT, leading to a smaller fraction of actual charge transfer reactions for P3HT with F1TCNQ than to F2TCNQ.

One other significant difference occurs between the dopants: the loss of σ after σ_{max} is higher for F1TCNQ and F2TCNQ than F4TCNQ. When comparing multiple runs of each dopant, P3HT-F4TCNQ retained ~70% of σ_{max}, P3HT-F2TCNQ retained ~35%, and P3HT-F1TCNQ retained ~30%. In order to better understand this instability, as well as relate individual doping times in *in situ* σ experiments to other characterization techniques, we also conducted *in situ* σ curtailed experiments, which show how σ for samples doped to certain doping times relaxes when its exposure to dopant is removed, and can be seen in **Figure 36**. These samples were removed from positive dopant pressure such that their doping times were 50 s apart, from 50 s to 300 s. The trends between the three dopants are similar: before σ_{max}, the σ pre-curtail appears stable post-curtail. This changes as σ_{max} is approached, as the drop in σ increases with doping time, with the most dramatic change in instability pre- and post-σ_{max}. This result indicates that the instability in σ is due to a process that occurs more frequently as σ_{max} is approach and surpassed, perhaps the disordering of aggregate domains and disruption of tie chains by the presence of molecular dopant that does not react with the polymer backbone.

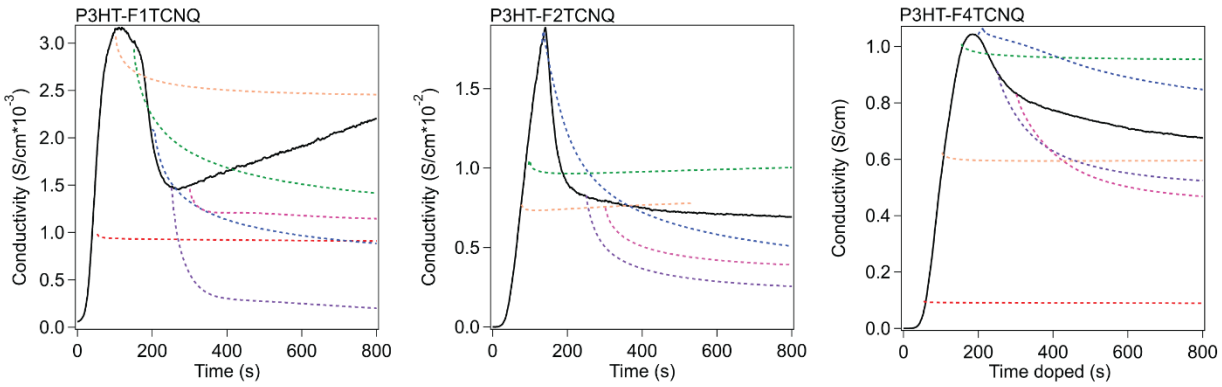

Figure 37**.** Stabilization of σ at 50 s intervals.

Samples of FNTCNQ-doped P3HT were removed from positive-dopant pressure, or curtailed, at 50 s sample intervals, and its relaxation in σ was followed. This was done to replicate the conditions of samples that were doped to these specific 50 s intervals for other experiments, such as UV-Vis-NIR spectroscopy, Raman spectroscopy, and GIWAXS. The solid curve is the σ of the non-curtailed sample, as seen in figure 36. The dotted lines that extend from the solid curve are samples taken off the dopant when the dotted line starts.

3.3.4 P3HT-FNTCNQ absorption measurements compare dopant strength and doping time to fraction of sites doped

UV-Vis-NIR spectra are often used for molecularly doped conjugated polymers to track the concentration of charge carriers in the polymer thin film.[16,21,39] We took advantage of this to compare the ratio of doped sites for P3HT doped with FNTCNQ.

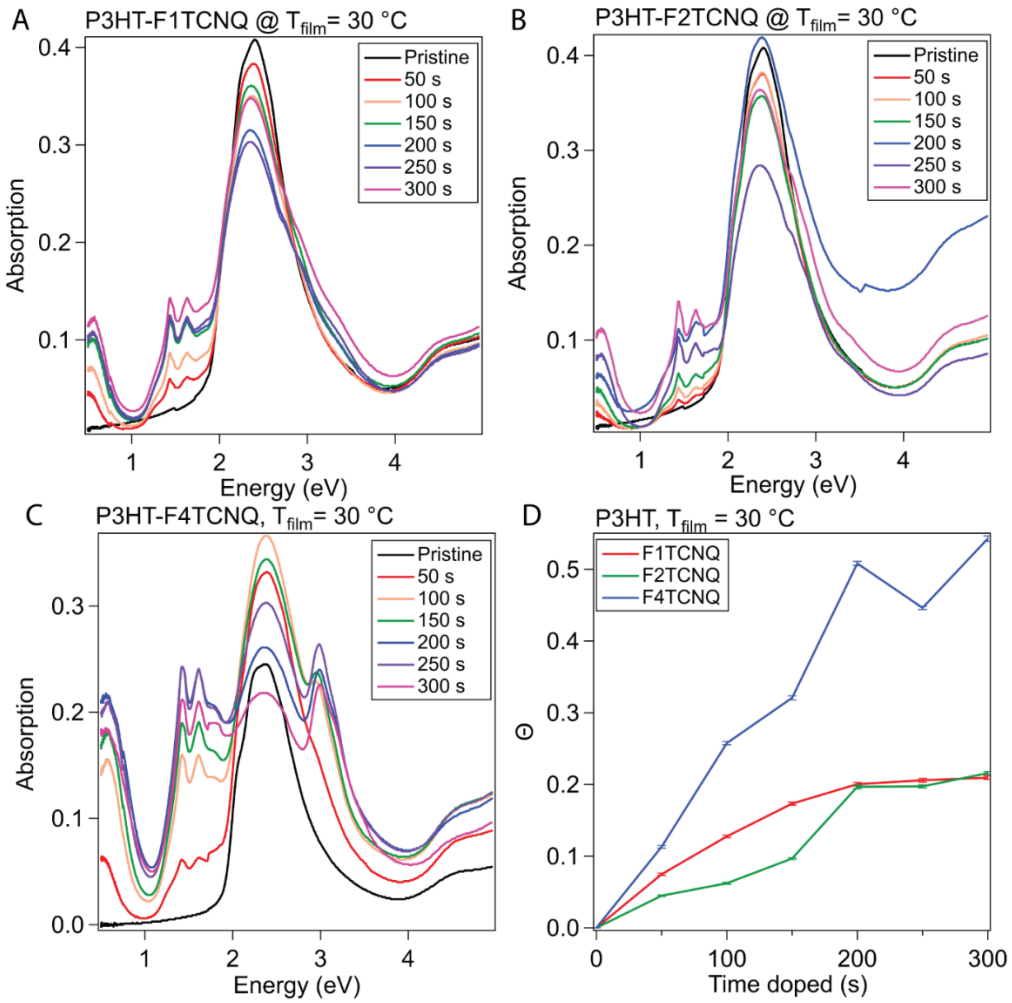

Figure 38. UV-Vis-NIR Absorption of P3HT-FNTCNQ samples.

Representative absorption spectra are shown for P3HT (A) -F1TCNQ, (B) -F2TCNQ, and (C) -F4TCNQ, with samples doped in 50 s intervals from neat sample to 300 s doped, with sample temperature T_{film} = 30 °C. The peak at 0.5 eV is attributed to the charge carrier in the film (polaron), and the peak at 2.3 eV is attributed to neutral, undoped polymer. These spectra are fit, and the area of these two peaks are compared using the parameter Θ, which is proportional to the fraction of doped P3HT sites, or roughly charge carrier concentration. (D) plots this parameter Θ against doping time for all three reactive dopants.

In **Figure 38A, B, & C**, we can see the progression of the absorption for P3HT doped with F1TCNQ, F2TCNQ, and F4TCNQ respectively, for samples doped to the same times as in the curtailed *in situ* σ experiments. As doping time increases, we can see for all three dopants the

emergence of peaks at 0.5 eV and 1.5 eV; these absorptions correspond to allowed sub-gap transitions for polaronic (*i.e.* charged) P3HT.[40–42] The peaks at 1.4 and 1.6 eV come from the FNTCNQ radical anion, and are evidence of integer charge transfer between the dopant and polymer backbone.[39] These experiments were also conducted on P3HT-TCNQ, whose spectra can be seen in **Figure 45**; these spectra showed no strong evidence of doping, as would be expected from the *in situ σ* experiment results.

In order to use these spectra to quantify the progression of sites being doped in the polymer thin film, we fit these spectra using the peaks shown in **Figure 46**, including fits of the main neutral P3HT peak at 2.3 eV, and the polaronic peak at 0.5 eV. We then follow a methodology of Murrey *et al.* to calculate the parameter Θ, which is an estimate of the fraction of doped P3HT sites over the total available P3HT sites.[8] This is done by using the equation

$$\Theta = \frac{A_P}{A_P + A_N} \qquad \text{(Equation 1)}$$

where A_P is the integral of the polaron absorption peak fit at 0.5 eV and A_N is the integral of the neutral P3HT absorption at 2.3 eV. Lim *et al.* use a similar analysis, and note that the fraction of doped sites we use here is not a statement that this is a fraction of sites with a charge on it at all times, but instead a measurement of the fraction of P3HT monomers that are affected by the presence of a charge (throughout the charge carrier's spatial extent).[25]

All three reactive dopants show a similar shape, with slight differences in timing that correspond to the different timings in σ_{max} seen in the *in situ σ* experiments. The number of sites doped appears to increase linearly with time until t_{max}, from which point the fraction of sites doped doesn't appear to change significantly. The final value of the fraction of sites doped corresponds to the strength of the dopant. For T_{film} = 30 °C, Θ_{F1TCNQ} = 20.9% ± 0.3%, Θ_{F2TCNQ} = 21.6% ± 0.2%, Θ_{F4TCNQ} = 54.3% ± 0.4%. Qualitatively, this means that less than half of the P3HT monomers in

the thin film are affected by the presence of a charge carrier in P3HT-F1TCNQ & -F2TNCQ relative to -F4TCNQ. This result indicates that the orders of magnitude difference in σ can't be attributed just to a difference in charge carrier concentration, alone.

3.3.5 Resonance Raman spectroscopy of P3HT-FNTCNQ shows dopant dependence of polymer ordering and charge location

Resonance Raman spectroscopy continues to be a powerful tool for probing the amorphous and aggregate domains of conjugated polymers separately. Partially, this is due to the technique's sensitivity to the highly-polarizable π-electrons along the conjugated backbone. However, Raman spectroscopy also can give spectra that are more sensitive to the aggregate or amorphous domains dependent on the excitation wavelength. If the excitation wavelength lines up with a particular feature in the sample's absorption, the Raman spectra will primarily probe that feature. Since these excitation wavelengths are in the UV-Vis range, the resonances can be compared to the UV-Vis-NIR peak breakdown in **Figure 46**.

For this study, we focused on 473 nm (2.62 eV) and 532 nm (2.33 eV) excitation wavelengths, which are resonant with the amorphous and aggregate neutral P3HT, respectively. The 532 nm excitation wavelength Raman for P3HT-F1TCNQ, - F2TCNQ, and -F4TCNQ can be seen in **Figure 39A, B, and C**. These spectra were obtained on films doped from 50 s to 300 s in 50 s intervals, and were focused in the 1300 to 1600 cm^{-1} region, which contains peaks attributed to C-C and C=C intraring vibration modes.[43] These peaks are sensitive both to their environment as well as the presence of charges, which allows for analysis into how these vibration modes change as dopant physically infiltrates the polymer film and creates charge carriers. Additionally, the strong peak ~1450 cm^{-1} seen in some of the spectra in **Figure 39A & C** are attributed to the neutral dopant, which is also resonant at 473 nm.

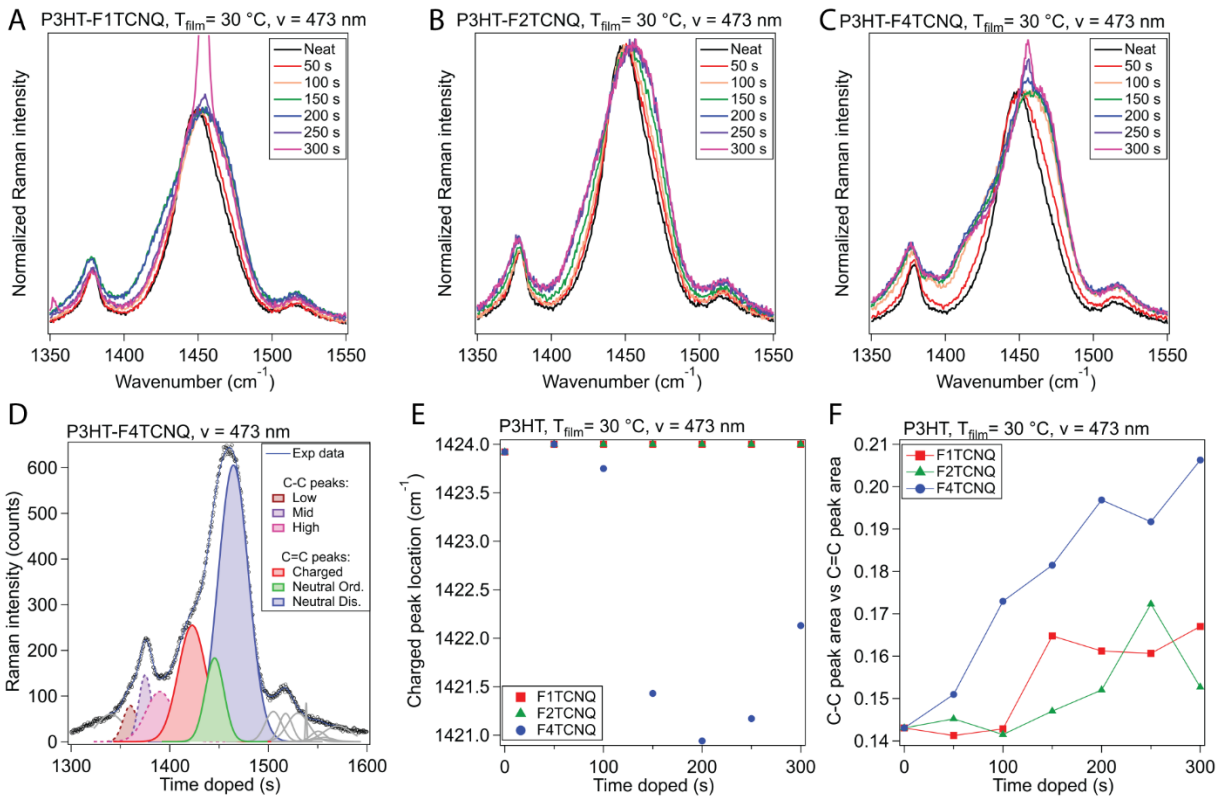

Figure 39. Raman spectra and peak fitting of P3HT-FNTCNQ samples.

Raman measurements were conducted on P3HT-FNTCNQ films doped from 50 s to 300 s with samples at 50 s intervals. The 473 nm excitation spectra are shown for P3HT- (A) F1TCNQ, (B) F2TCNQ, and (C) F4TCNQ. (D) Peak fitting for 473 nm is shown, with peaks for C-C and C=C highlighted. (E) The location of the "charged" C=C peak is plotted against doping time for all three dopants. (F) The ratio of the C-C peak area versus the C=C peak area is plotted against doping time. More detailed descriptions of the fitting methods, along with similar plots for 532 nm excitation spectra, can be found in figures 48 and 49.

Following an analysis described by Nightingale *et al.*, we fit peaks in this range, including three attributed to the C-C intraring stretching mode (~1360, 1380, and 1390 cm^{-1}) and three attributed to the C=C symmetric stretching mode (~1420, 1445, and 1465 cm^{-1}). This peak fitting can be seen in **Figure 39D**. For the analysis from Nightingale *et al.*, these three C=C symmetric stretching mode were labeled as from populations backbones that were charged, ordered, and

disordered, respectively.[43] Bounds for peak location and width were taken from the Nightingale analysis and were given to allow for changes in the mean and distribution of conjugation lengths.

We analyzed these peak fits in two ways to track the evolution of the film as dopant concentration increased. Firstly, we tracked the change in the location of the "charged" C=C symmetric peak. As the charged peak shifts to lower wavenumbers, more of the charged population can be attributed to charges in the amorphous portion of the film. Hence, by tracking how the charged peak's location (which for this fit was bound between 1424 and 1418 cm^{-1}) changes over time, we can track whether the charge carriers are being created preferentially in the aggregate or amorphous domains at different points in the doping curve. Our second analysis compared the peaks attributed to C-C versus that for C=C. This ratio is correlated with the coplanarity of the individual monomers on the backbone, or torsional order.

These two analyses for all three dopants with an excitation wavelength of 473 nm are displayed in **Figure 39E & F**, with 532 nm excitation in **Figure 48 and 49**. Using the 473 excitation Raman, we can see that the location the charged C=C peak is fit to only appreciably changes with the P3HT-F4TCNQ samples. In the previous chapter, we reported that the charged, disordered fraction of the film reached a maximum at t_{max} (~200 s). This result agrees well with our analysis here, as the lowest charged peak location coincides with this time. Similarly, this analysis corroborates our previous claim that the F4TCNQ is capable of doping the amorphous domains, whereas F1TCNQ and F2TCNQ are too weak.

Comparing the C-C area to C=C area ratio between dopants, the evolution of this ratio adheres well to the change in Θ seen from our UV-Vis-NIR analysis. The higher the concentration of charge carriers in our system, the more coplanar the monomeric units. This same result and trend is seen when doing this analysis on the 532 nm excitation Raman spectra, indicating that the

presence of charge carriers improves coplanarity in both amorphous and aggregate domains, a result that has been seen in previous P3HT vapor doping literature.[4,26]

3.3.6 Packing structure of P3HT shows dopant independence in alkyl stacking, dopant dependence in π-π stacking

We further examined the aggregate domains in P3HT and its changes when vapor doped by FNTCNQ by using grazing incidence wide angle X-ray scattering (GIWAXS). Although Raman already gives some insight into how the aggregate domain is affected by the presence of dopant, GIWAXS allows for more detailed analysis of how dopant packs into the aggregate domain, and how this affects ordering between the alkyl sidechain direction or through the plane of the backbone and alkyl stacking along the π-orbitals. The quality of this ordering are determinants on the mobility of charge carriers in the aggregate domains; in particular, the alignment of the π-orbitals of multiple polymer backbones (the "π-π stacking") facilitates interchain transport of charge carriers, which is necessary for efficient transport.[44]

1D scattering profiles were obtained via azimuthal integration of the scattering image, and highly doped (300 s) profiles can be seen in **Figure 39A** (spectra from neat to 300 s doped for F1 through F4TCNQ can be seen in **Figure 40**). These profiles feature (*h*00) peaks that correspond to the lamella-stacked sidechains, primarily seen in the q_z direction, and a broader ring, a (020) peak, that appears at higher q values in both the q_z and q_{xy} directions that corresponds to the π-π stacking. Using the value of the maxima of these peaks, we calculate that the neat P3HT's alkyl stacking spacing and π-π stacking spacing are 1.67 nm and 0.385 nm, which are similar to previously reported literature values.[25,26,45]

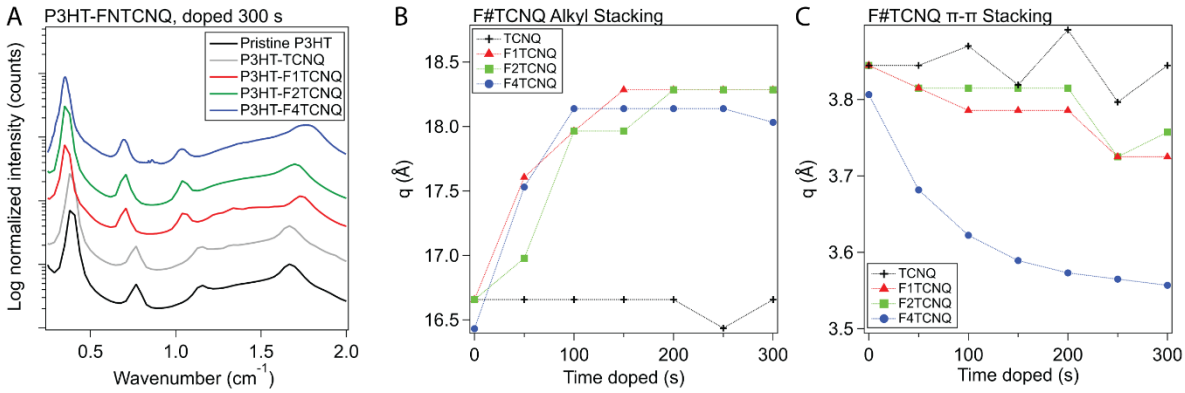

Figure 40. GIWAXS and analysis of characteristic stacking spacings of P3HT-FNTCNQ samples. (A) Azimuthal linecuts of 300 s doped P3HT with all four dopants. These linecuts were generated from the GIWAXS 2D scattering images, and a full progression of linecuts can be seen in figure 50. (B) Alkyl stacking spacing and (C) π-π stacking spacing was extracted from the azimuthal linecuts for the neat sample, and samples doped from 50 s to 300 s.

These values change when dopant is introduced into the system. We have seen in previous literature that when F4TCNQ is introduced into the P3HT thin film via vapor doping, that the alkyl stacking spacing grows due to the F4TCNQ molecular settling in between the alkyl stacks, and the π-π stacking spacing shrinks, which we believe to be due to a Coulombic attraction between the partially negatively charged backbone and the positive charge carriers on neighboring backbones.

Extracting the alkyl stacking spacing from the azimuthal linecuts of the 300 s doped P3HT with all four of our dopants, we find that the alkyl stacking spacings are 1.67 nm, 1.83 nm, 1.83 nm, and 1.80 nm, for TCNQ, F1TCNQ, F2TCNQ, and F4TCNQ respectively. We attribute the slightly lower spacing for P3HT-F4TCNQ to the slightly lower spacing of the neat P3HT used for those measurements; otherwise, it appears that if the dopant is reactive with the aggregate portion of the film, it can infiltrate into the alkyl stacking and swells the alkyl stacking spacing by 1.6 Å. We can see how the alkyl stacking spacing changes as dopant concentration increases in **Figure 40B**. Although the sublimation rate was controlled such that t_{max} is similar between the dopants,

P3HT-F4TCNQ reaches a maximum alkyl stacking spacing at around 100 s, which is faster than t_{max}, F2TCNQ reaches a maximum at 150 s (slightly before its t_{max}), and F1TCNQ at 200 s (at or past its t_{max}). This agrees with our understanding of how the strength of the dopant impacts where it is doping at which point in the doping curve: F4TCNQ dopes the aggregate domains within the first 100 s and switches to primarily doping the amorphous domain from then on, whereas F2TCNQ and F1TCNQ are only capable of doping the aggregate domains, and hence continue to affect the mean alkyl stacking spacing distance until around when it stops introducing new charge carriers altogether.

When we do the same extraction for the π-π stacking spacing, we see that the final spacing, unlike the alkyl stacking spacing, is dopant strength dependent. This spacing is 0.385 nm, 0.372 nm 0.376 nm, and 0.356 nm for TCNQ, F1TCNQ, F2TCNQ, and F4TCNQ respectively. When following how this spacing evolves over the course of doping, we can see that it continues to shrink for all three reactive dopants until t_{max}. These results point towards two facts: one, that the shrinking of the mean π-π stacking spacing is sensitive to the concentration of charge carriers, and that it is sensitive to charge carriers both in the aggregate and amorphous regimes. Smaller π-π stacking spacing leads to better π orbital overlap between neighboring backbones, and hence better μ for the charge carriers in the material. We believe that this explains partially why that although our UV-Vis-NIR and Raman analyses pointed towards the charge carrier concentration being on the same order of magnitude for all three reactive dopants in this study, that the σ is orders of magnitude apart.

3.3.7 P3HT-F1TCNQ *in situ* conductivity reveals film temperature dependence of conductivity curve

Our previous paper involving *in situ* σ showed that P3HT-F4TCNQ showed litte dependence on the temperature of the film between the temperatures we tested (T_{film} = 0 to 70 °C). We hypothesized that this may not be true for all dopants. **Figure 41** shows *in situ* σ experiments with T_{film} = 0, 30, and 70 °C. We can see that for the high T_{film} experiment, the σ curve has different behavior post-σ_{max} (which also occurs earlier than in other (T_{film}): instead of dropping to a final, stable σ, the curve instead drops, then rises again to a higher σ. This σ_{final} is a higher fraction of σ_{max} than for lower T_{film}, but it results in a similar σ_{final} to the other curves. This phenomenon was not seen in P3HT-F4TCNQ or P3HT-F2TCNQ, but was also seen for the mostly non-reactive TCNQ doped P3HT (these curves can be seen in **Figure 51D**). **Figure 41B** shows the dependence of the P3HT-F1TCNQ *in situ* σ curve on T_{film}. We can see that this curve shape is quicker and more dramatic at higher T_{film}, but the characteristic fall and rise is present in samples with T_{film} > 20 °C.

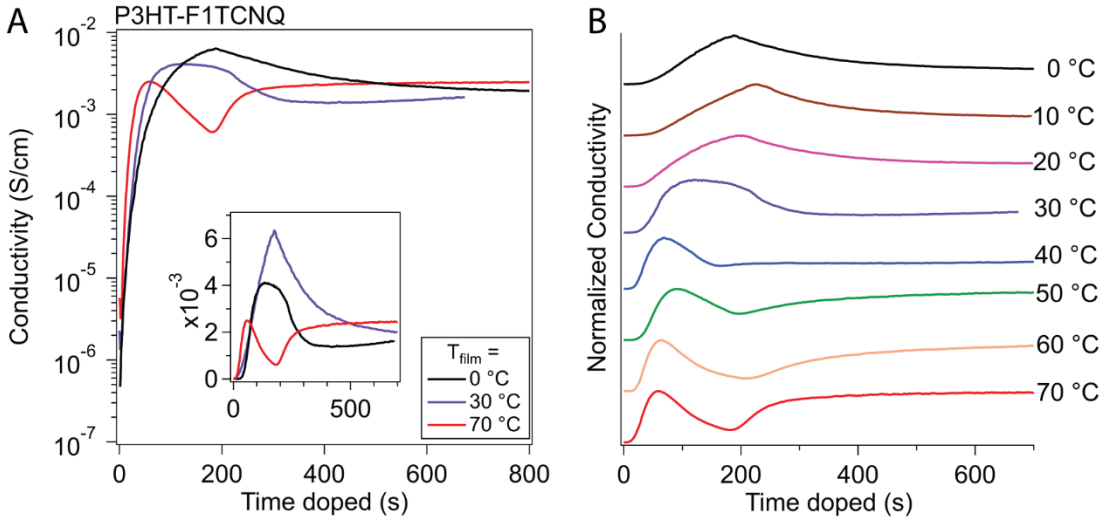

Figure 41. *In situ* σ of P3HT-F1TCNQ for different T_{film}.
(A) *In situ* σ for P3HT-F1TCNQ at T_{film} = 0, 30, and 70 °C are plotted against each other. (B) The shape of the *in situ* σ for P3HT-F1TCNQ at T_{film} between 0 °C and 70 °C at 10 °C intervals are compared.

Because this phenomenon is only visible dynamically, we could only capture any extra information about this trend through our curtailed *in situ* σ experiments, which can be seen in **Figure 51**. This rise in σ occurs even after the P3HT thin film has been taken off positive pressure of dopant but occurs more quickly at higher doping times/dopant concentrations, and only starts occurring as the time doped approaches t_{max} (~100 s in these samples). Our other experiments on P3HT doped with F1TCNQ at T_{film} = 70 °C did not find any insight as to why the curve takes this shape. Our only hypothesis is that F1TCNQ's lower reactivity combined with its lower sublimation temperature causes some form of recongifuration as the dopant concentration grows. Regardless, we believe that this is evidence that there remains more mysteries about the method in which the dopant infiltrates, reacts with, and settles within the conjugated polymer backbone, and that with clever (*in situ*) instrumentation, we may be able to better understand and control this process.

3.4 Conclusion

This study investigated vapor doping of P3HT with TCNQ and its fluorinated derivatives in order to probe how the evolution of conductivity (σ) *in situ*, and its corresponding structural changes, differed as the strength of the interaction between the polymer and dopant changed. TCNQ, whose interaction with both amorphous and aggregate P3HT is energetically unfavorable, F1TCNQ & F2TCNQ, which energetically can react with the aggregate P3HT, and F4TCNQ which has the ability to react with both amorphous and aggregate P3HT, were chosen for these experiments. All four dopants, regardless of strength of interaction, showed very similar *in situ* σ curves. All but TCNQ first exhibited a rapid exponential rise, and all exhibited a slower linear increase to a σ_{max}, after which a final slow decay took the film to a final, stable σ. The relaxation of σ was tested by doping P3HT to a specific time, after which it was taken off the dopant. The

decay and stabilization of the σ for all three reactive dopants depended on the proximity of the time to t_{max}, where the decay was strongest close to and after t_{max}.

These vapor doped P3HT thin films, doped to the times explored in the relaxation/decay experiments were characterized through UV-Vis-NIR spectroscopy, GIWAXS, and Raman spectroscopy. Analysis of the UV-Vis-NIR spectra provided insight on the doping level through the fraction of doped sites. For all three reactive dopants, the doping level increased linearly with doping time until hitting a maximum near t_{max}, at which point the doping level stabilized. This analysis also showed that P3HT-F4TCNQ had more than twice the number of doped sites than that of P3HT-F1TCNQ and F2TCNQ. Resonant Raman spectroscopy experiments allowed for more precise determination of doping within the aggregate and amorphous domains of the polymer, as well as how the presence of dopant affected the coplanarity of the individual monomeric units of the polymer backbone. The former analysis showed that the F4TCNQ, as expected, was capable of doping both amorphous and aggregate domains, whereas F1TCNQ and F2TCNQ preferentially charged only the aggregate domains. However, all three dopants were capable of inducing order within both the amorphous and aggregate domains, which likely is induced by the presence of charge carriers on the polymeric backbone. Analysis of the scattering from GIWAXS allowed for tracking of the alkyl stacking and π-π stacking spacing within the aggregate domains over the course of doping. The alkyl stacking spacing showed that the change in spacing was only dependent on whether the dopant could react with the aggregate domains; the π-π stacking spacing however shrunk in conjunction with the strength of the dopant, reaffirming that the π-π stacking spacing condenses due to the Coulombic attraction between the partially negatively charged polymer backbone and a neighboring backbone with a positive charge carrier. P3HT doped by F4TCNQ reached its maximum alkyl stacking spacing much quicker than t_{max}, whereas P3HT-

F1TCNQ and -F2TCNQ stabilize around t_{max}, reinforcing the results from our Resonance Raman analysis that only the F4TCNQ finishes doping the aggregate domains and most growth in σ past this point comes from doping the amorphous domain.

Some outstanding mysteries remain about the shape of the doping curve, which is highlighted by the shape of the doping curve for high T_{film} P3HT-F1TCNQ. These curves are characterized by a decay in σ post σ_{max}, which then rises to a final σ that sits closer to σ_{max} than films doped at a lower T_{film}. For P3HT-F1TCNQ, the transition between this different type of *in situ* σ and our standard curve appears to occur between T_{film} = 20 and 30 °C. P3HT-TCNQ also exhibits similar traits in its doping curves, but due to its low to non-existent doping of P3HT, it is difficult to probe.

We believe that this is evidence that there is yet more information that can be gleaned about the interaction and infiltration of dopant into a conjugated polymer thin film from this combination of *in situ* σ measurements and this suite of characterization techniques. Through clever selection of polymer-dopant pairing and T_{film}, we have shown new insight on how to control the structure and σ of our materials. Further usage of these techniques with novel polymer-dopant pairings, different sidechains, and different functional groups on the backbone will help our understanding on how the polymer chemistry, polymer structure, and doping mechanism affect the molecular doping process.

3.5 Experimental Methods

3.5.1 Materials and sample preparation

All substrates used for Grazing incidence wide angle X-ray scattering (GIWAXS), Raman spectroscopy, Atomic Force Microscopy (AFM) and UV-vis absorption spectroscopy in this study were cleaned by ultrasonication in acetone and 2-propanol for 15 minutes each. GIWAXS measurements were performed on films deposited on Si substrates with 1.5 nm of native SiO_2.

UV-vis absorption, Raman measurements, and AFM were performed on films deposited on top of quartz substrates. Conductivity measurements were performed on films deposited on custom-fabricated interdigitated gold electrodes (IDEs), which in turn is on Si substrates with 1000 nm of thermally-grown SiO_2. Solutions of 91% to 94% regioregular Poly(3-hexylthiophene-2,5-diyl) (RR-P3HT) (Rieke Metals) were prepared by dissolving P3HT in anhydrous chlorobenzene at 10 mg/mL. The mixed solutions were shaken overnight before being spun onto the prepared substrates. The substrates were spin coated with solution at 2000 rpm at 45 seconds, then at 3000 rpm for 25 seconds. IDEs were cleaned of excess polymer with cotton swabs to reduce leakage current.

3.5.2 *In situ* conductivity setup

For the *in situ* conductivity measurements, a specialized setup was fabricated for control and precision of measurement. A steady-state temperature is achieved using a thermoelectric module. The sample is held in place by two electrode probes, which allows for electrical contact with the sample during vapor doping. A more detailed description and visuals can be found in chapter 2.

3.5.3 Vapor doping process

Vapor doping of TCNQ, F1TCNQ, F2TCNQ, and F4TCNQ was performed in an argon-filled glovebox. Approximately 5 mg of dopant was pressed into a pellet and placed in an aluminum oxide crucible (OD 6.8 mm x H 4 mm from Government Scientific Source Inc.), which was in turn placed in a glass insert (diameter ~ 5 cm, height ~ 4.5 cm). Crucibles were cleaned as necessary and were only used for a single dopant as to prevent cross-contamination. A stainless-steel container is then preheated to allow the chamber to reach the desired temperature, which is monitored by thermocouple, and the glass insert is placed inside the container, at which point the

setup is allowed to stabilize in temperature. A Teflon cap is placed upon the opening of the glass insert to block dopant from polluting the glovebox.

All samples used for doping were placed within the sample holder. Electrical contact was made to the sample through the sample holder, which was then routed via cables through the back of the glovebox to a SP-200 Potentiostat. A voltage of 100 mV is applied to the sample, and the current through the sample is measured by the potentiostat every second. This data is converted from current to conductivity through the equation:

$$\sigma_{IDE} = \frac{1}{R}\frac{d}{l(N-1)h}$$

where d = 8 μm is the separation distance between the electrode digits, l = 150 μm is the length of the digits, N = 80 is the number of electrodes and h is the thickness of the sample.[46]

3.5.4 UV-Vis-NIR

UV-VIS-NIR spectra of neat P3HT and vapor-doped thin films on quartz substrates were obtained using the Shimadzu UV-3600 Plus UV-VIS-NIR Dual Beam Spectrophotometer housed in the Soft Matter Characterization Facility (SMCF) (Pritzker School of Molecular Engineering, University of Chicago). Measurements were taken within a wavelength range of 250 to 2480 nm.

3.5.5 Raman spectroscopy

Raman spectroscopy experiments were performed under ambient conditions using the Horiba LabRAM HR Evolution NIR confocal Raman microscope housed in the Chicago Materials Research Center. Raman spectra of neat and doped P3HT thin films was collected using a 100× objective and 473 nm and 532 nm wavelength lasers. Laser power and was set to 1% for 473 nm, 0.1% for 532 nm wavelength to minimize local heating and material degradation. Spectra were taken between a wavenumber range of 1149 to 1746 cm^{-1} for 473 nm excitation and 1229 to 1668 cm^{-1} for 532 nm excitation laser.

3.5.6 Grazing incidence wide angle X-ray scattering (GIWAXS)

GIWAXS experiments were conducted at the Advanced Photon Source (Argonne National Laboratory) at beamline 8-ID-E. The energy of the incident beam was at 10.91 keV, and a Pilatus 1MF pixel array detector (pixel size = 172 μm) was used.[47] The measurement time for one image was 10 seconds. All samples were placed and measured in a low vacuum chamber (10^{-3} mbar) to reduce the air scattering as well as to minimize beam radiation damage. There are multiple rows of inactive pixels between the detector modules when the images were collected at one position. To fill these inactive gaps, the detector was moved down to a pre-set new position along the vertical direction after each measurement. After the image was collected at the new spot, the data from these two detector positions were combined using the GIXSGUI package for MATLAB to fill the inactive gaps. The absence of artifacts in the combined image demonstrates that the scattering from the sample does not change during the exposure. The GIXSGUI package was also used to output the GIWAXS signals as intensity maps in (q_r, q_z) space, integrated angularly, and then linecut azimuthally. GIWAXS images of thin films were taken at a grazing incident x-ray angle of 0.14°, which is above the critical angle of the polymer film and below the critical angle of the silicon substrate.

3.6 Appendix

3.6.1 Spano model fit of neat P3HT

The Spano model was used to make estimate of percent of aggregate versus amorphous fractions in the P3HT used in this study. The model dictates that the absorption spectra of P3HT thin films in the ~2.0 eV to 3.0 eV range are comprised of low-energy π-stacking aggregate peaks and higher energy amorphous-fraction peaks. In order to determine the vibration bands for the aggregate portion, we utilize a Franck-Condon fit:

$$A_{\text{aggregate}} \propto \sum_{m=0} \left(\frac{S^m}{m!}\right) \times \left(1 - \frac{We^{-S}}{2E_p} \sum_{n \neq m} \frac{S_n}{n!\,(n-m)}\right)^2 \times e^{\left(E - E_0 - mE_p - \frac{1}{2}WS^m e^{-S}\right)^2 / 2\sigma^2}$$

Where *A* is the absorption of the aggregates as a function of photon energy, *E*; *S* is the Huang-Rhys factor, which represents the overlap between individual vibrational states (we assume this to be 1 for this fit); *m* corresponds to different vibrational energy levels; E_p = 0.179 eV the energy of the C=C symmetric branch mode in P3HT; the three fitting parameters are: *W*, the exciton bandwidth; E_0, the transition energy; and σ, the energetic disorder, which in this case is the Gaussian width of the absorption peaks. The peaks generated by this Franck-Condon fit can be seen in **Figure 42B**: the individual peaks are red with dotted lines, and the summation the solid red line, which appears to fit the shoulder from ~2.0 eV to 2.5 eV in the absorption well. The amorphous fraction was taken to be the higher energy region, obtained by subtracting the aggregate absorption calculated from the absorption from the experiment. The percent aggregate is calculated from this fit by taking the integrated area of the aggregate peaks to the amorphous peaks, and this was found for this fit to be roughly 37%. A Matlab fit program was used to perform the Spano fit as described by Dong *et al*.[48]

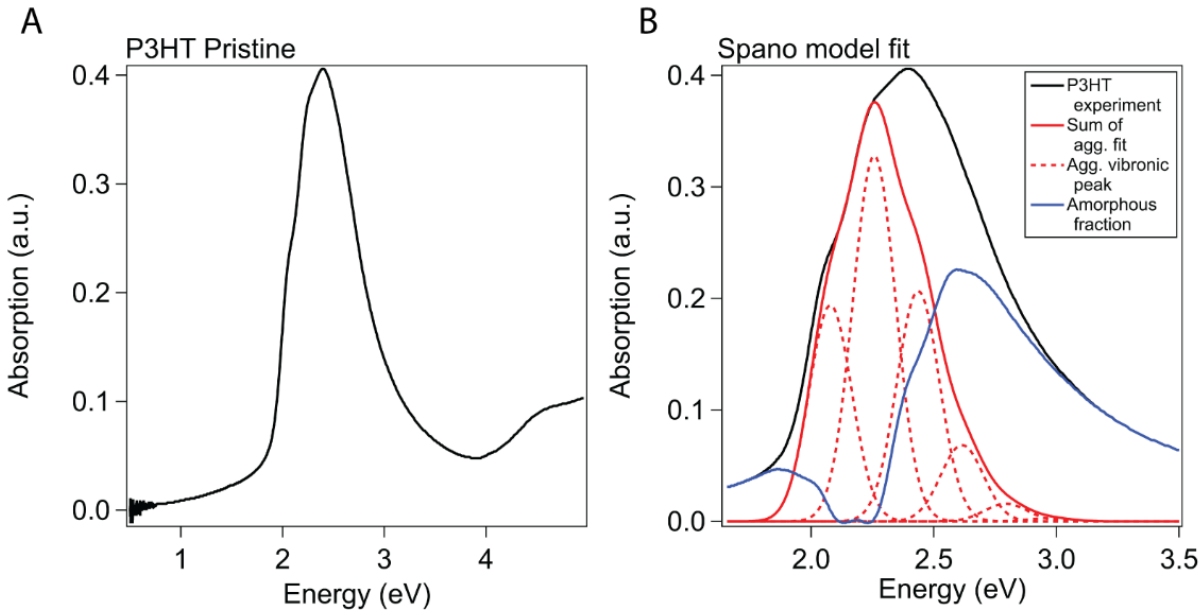

Figure 42. Pristine P3HT UV-Vis absorption fit with Spano model.

(A) UV-Vis-NIR of neat P3HT thin film. (B) Spano model fit.

3.6.2 Cyclic voltammetry of P3HT and FNTNQ

Cyclic voltammetry (CV) was performed using a Biologic SP200 potentiostat in as standard 3-electrode configuration. Testing was performed in an anhydrous, degassed acetonitrile solution with a 0.1 M tetrabutylammonium hexafluorophosphate supporting electrolyte concentration at a scan rate of 0.1 V/s. A silver wire in 0.01 M $AgNO_3$ and 0.1 M supporting electrolyte served as a reference electrode, and a platinum wire was used as a counter electrode. Ferrocene purified by sublimation was used as an internal standard. All experiments were performed in a dry argon glove box. TCNQ, F1TCNQ, F2TCNQ, and F4TCNQ were dissolved directly in acetonitrile at 0.01 M concentration. P3HT was spin coated onto an ITO-coated glass slide according to the procedure described in the experimental method section. Ionization energy (IE, HOMO) of the polymers and electron affinity (EA, LUMO) of the dopants were determined by comparison against the ferrocene couple (5.1 eV), as described here:

$$IE = q\left(E_{ox} + 5.1 - E_{F,ox}\right)$$

$$EA = q(E_{red} + 5.1 - E_{F,red})$$

where q is the fundamental charge of an electron, E_{red} is the reduction potential of F4TCNQ, and $E_{F,red}$ is the oxidation potential of ferrocene. Onset potentials were calculated by regressing the rising slope of the oxidation peak to the intersection point of the system background current. The linear regression and background current are seen straight lines in the CV plot for P3HT. The amorphous-P3HT HOMO was calculated by comparing the difference in voltage between the peak value of the aggregate P3HT and the amorphous-P3HT in the CV, and subtracting this from the calculated onset potential of the aggregate P3HT.[49] From this method, the HOMO of aggregate P3HT was calculated to be -5.11 eV, the HOMO of the first population of amorphous P3HT to be -5.30 eV, and the second population of amorphous P3HT to be -5.53 eV. The LUMO level for TCNQ and its fluorinated derivates were calculated by this method to be -4.91, -5.01, -5.09. and -5.28 eV for TCNQ, F1TCNQ, F2TCNQ, and F4TCNQ respectively.

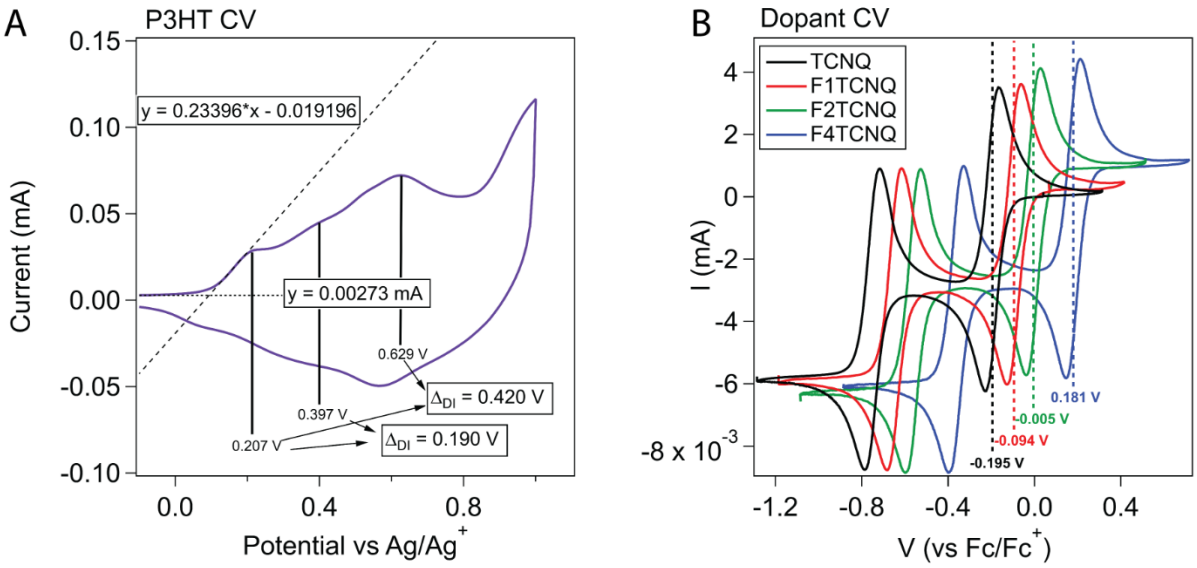

Figure 43. Cyclic voltammetry of P3HT and dopants.
(A) CV of P3HT. (B) CV of TCNQ, F1TCNQ, F2TCNQ, and F4TCNQ.

3.6.3 Thermogravimetric analysis of dopant sublimation

5 mg pellets of F1TCNQ, F2TCNQ, and F4TCNQ were made in the same aluminum oxide crucibles that were used for the *in situ* σ experiments and placed on a thermogravimetric analysis pan (TGA). Using the rate of mass loss in TGA experiments, sublimation rates were calculated at temperatures from 160 °C to 200 °C at 10 °C intervals. In order to most closely compare our P3HT-F1TCNQ and -F2TCNQ *in situ* σ experiments to those previously done on P3HT-F4TCNQ at T_{dopant} = 200 °C, which was shown here to have a sublimation rate of 3 µg/min, T_{dopant} was selected to be 180 °C (1.3 µg/min) and 160 °C (1. 6 µg/min) for F2TCNQ and F1TCNQ, respectively. Although we did not measure sublimation rate at these temperatures for TCNQ, we selected T_{dopant} = 140 °C, so that it would be a rate that was roughly equivalent to the rest based upon the trend.

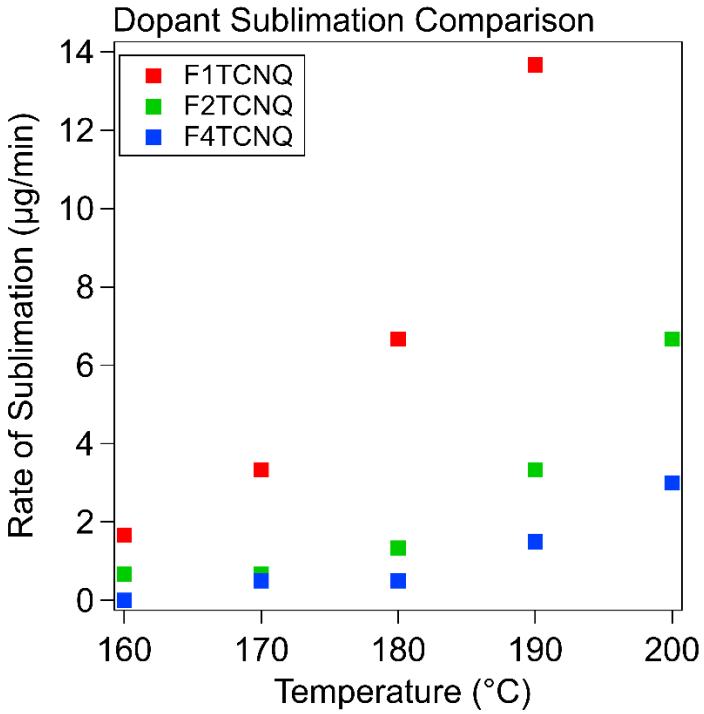

Figure 44. Sublimation rate of molecular dopants found by thermogravimetric analysis.

3.6.4 UV-Vis-NIR, FTIR spectroscopy

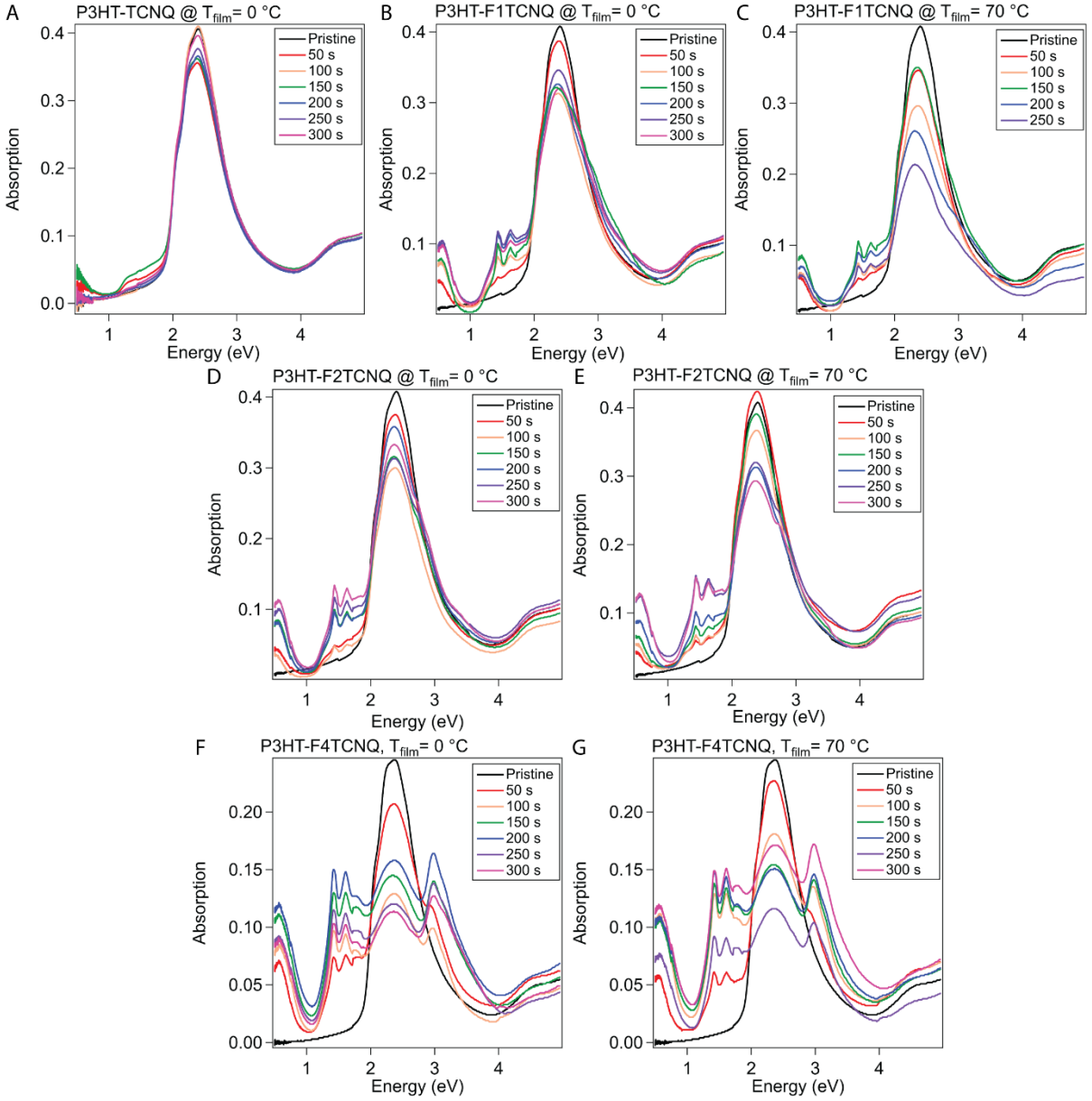

Figure 45. UV-Vis-NIR of P3HT-FNTCNQ at T_{film} = 0 °C & 70 °C.

Absorption measurements were conducted on P3HT-FNTCNQ films doped to the levels shown in fig. 3 (0 s to 300 s at 50 s intervals). (A) TCNQ, T_{film} = 0 °C (B) F1TCNQ, T_{film} = 0 °C (C) F1TCNQ, T_{film} = 70 °C (D) F2TCNQ, T_{film} = 0 °C (E) F2TCNQ, T_{film} = 70 °C (F) F4TCNQ, T_{film} = 0 °C (G) F4TCNQ, T_{film} = 70 °C.

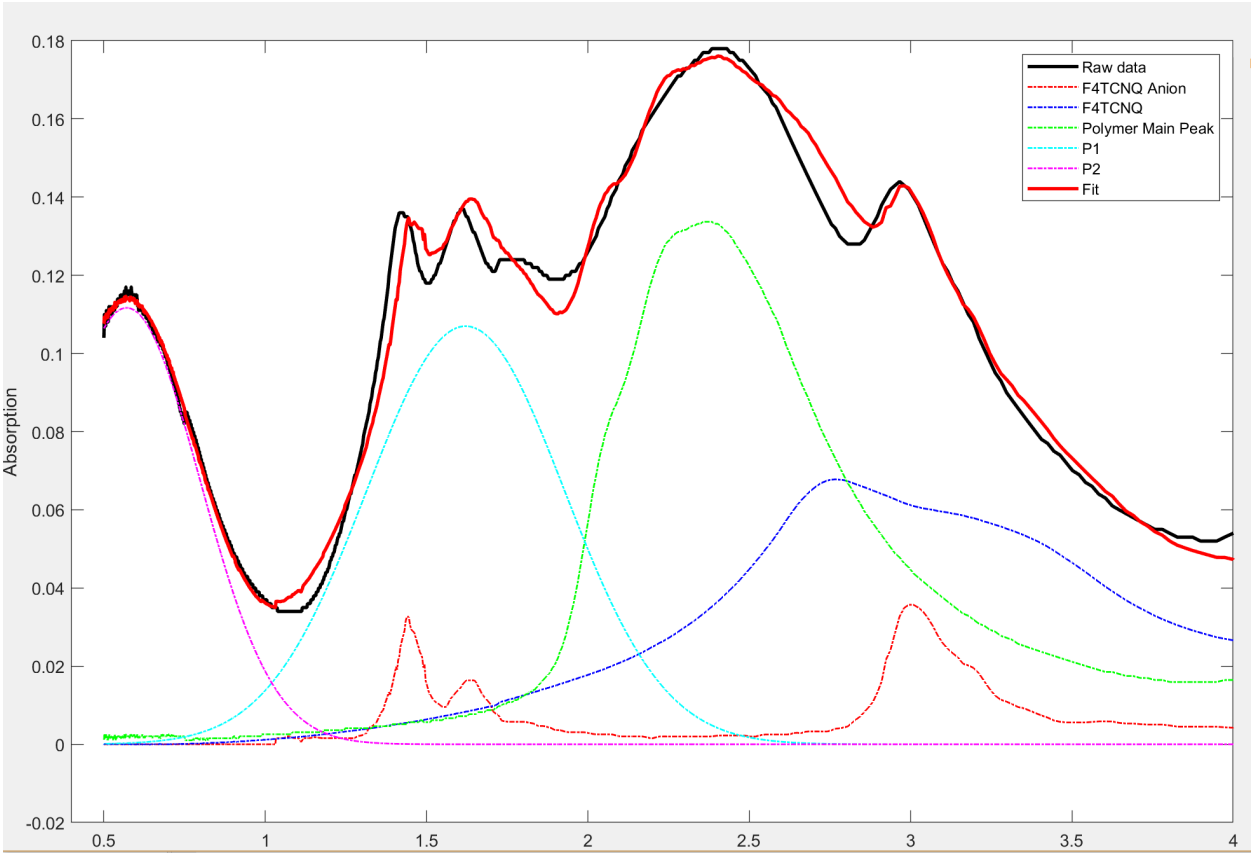

Figure 46. Fit of UV-Vis absorption.

Description of peaks adapted from Hynynen, Kiefer and Müller.[50] F4TCNQ anion, polaron peaks 1 and 2 were taken from the same paper. The F4TCNQ neutral peak was obtained from our own absorption measurements on vapor-deposited F4TCNQ. The ratio between the fitted polaron 1 peak (labeled P1 here) and the polymer neutral peak (labeled polymer main peak here) is what is used in figure 38 in the main manuscript, and in figure 45.

3.6.5 Raman spectroscopy and fitting

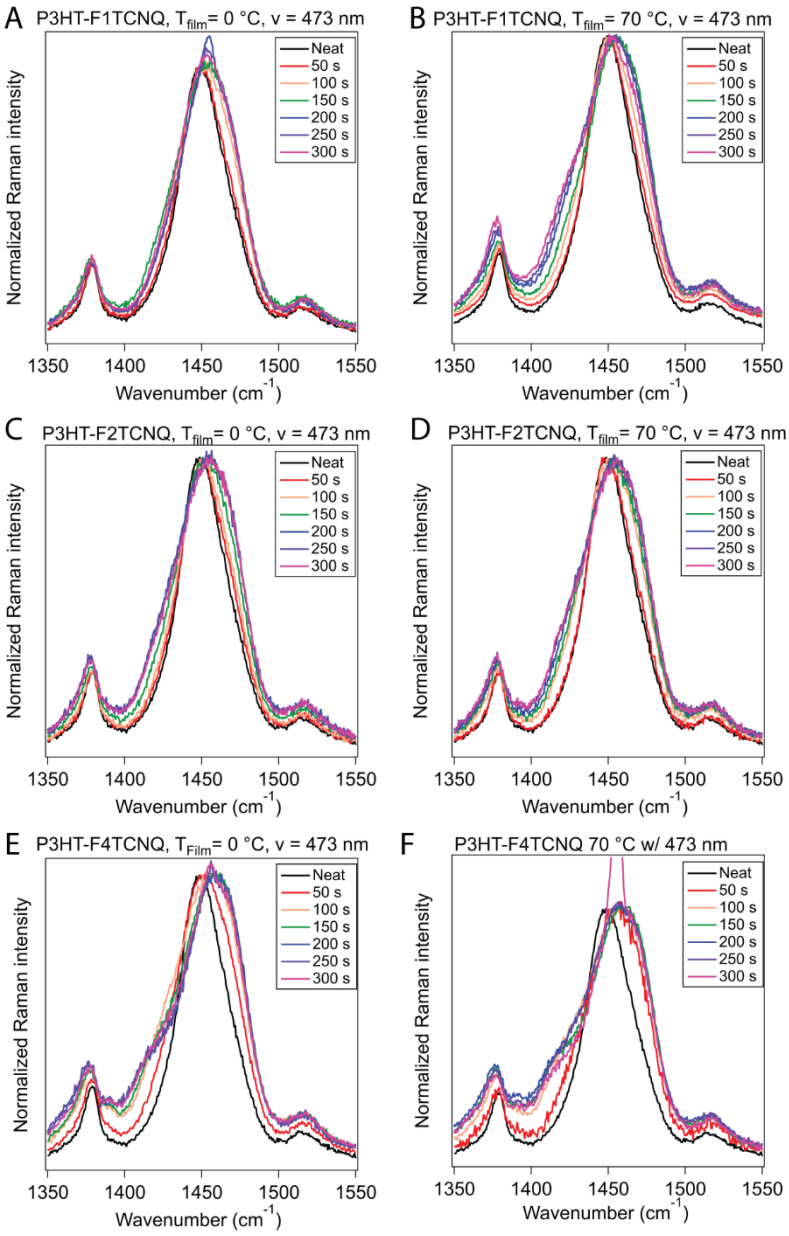

Figure 47. Raman spectra of P3HT-FNTCNQ excited by 473 nm laser @ 0 and 70 °C.

Raman spectra with a 473 nm laser excitation collected on P3HT doped to films doped with FNTCNQ from 0 s to 300 s at 50 s intervals. (A) F1TCNQ, T_{film} = 0 °C (B) F1TCNQ, T_{film} = 70 °C (C) F2TCNQ, T_{film} = 0 °C (D) F2TCNQ, T_{film} = 70 °C (E) F4TCNQ, T_{film} = 0 °C (F) F4TCNQ, T_{film} = 70 °C.

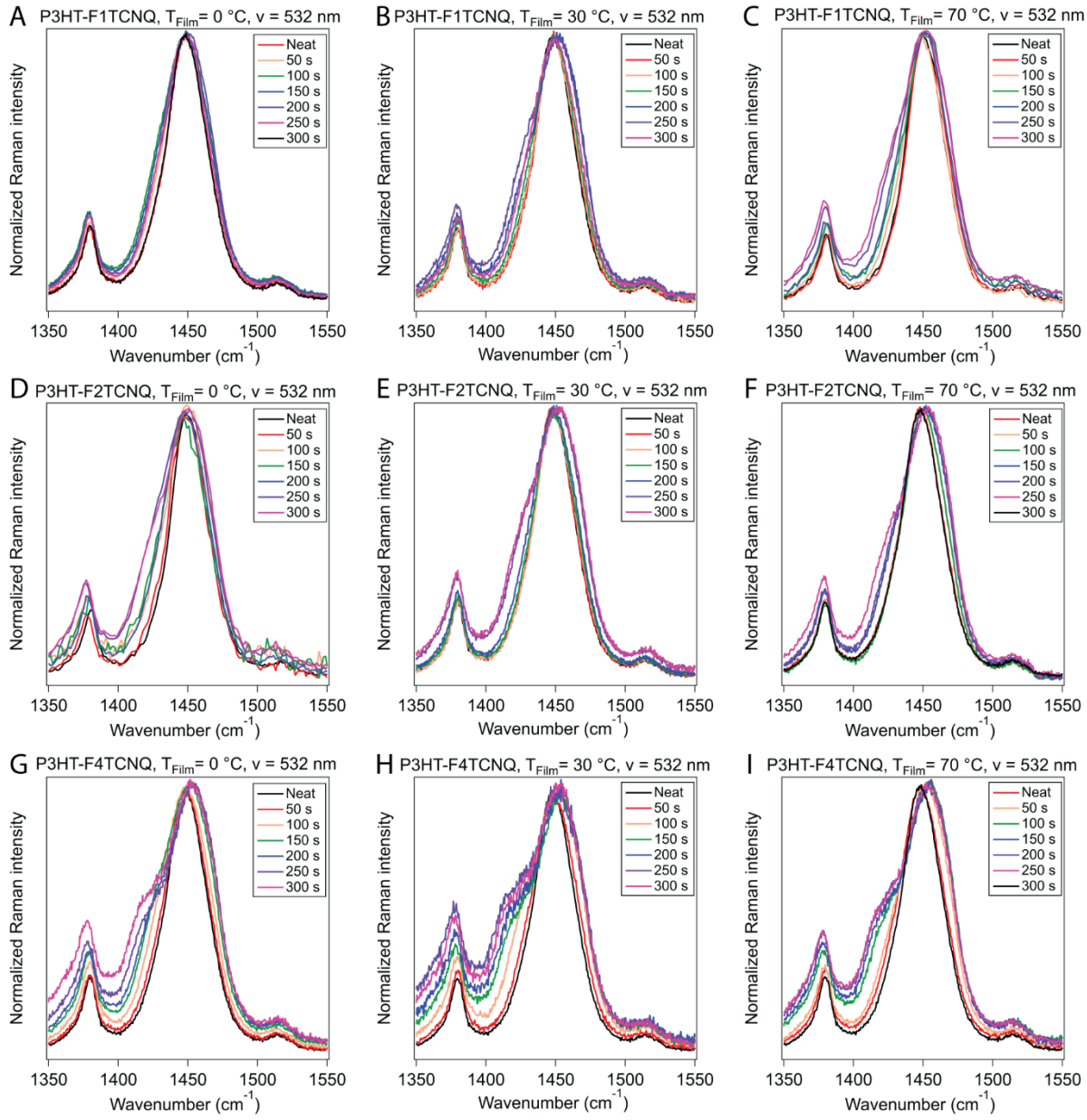

Figure 48. Raman spectra of P3HT-FNTCNQ excited by 532 nm laser @ 0, 30, and 70 °C.

Raman spectra with a 532 nm laser excitation collected on P3HT doped to films doped with FNTCNQ from 0 s to 300 s at 50 s intervals. (A) F1TCNQ, T_{film} = 0 °C (B) F1TCNQ, T_{film} = 30 °C (C) F1TCNQ, T_{film} = 70 °C (D) F2TCNQ, T_{film} = 0 °C (E) F2TCNQ, T_{film} = 30 °C (F) F2TCNQ, T_{film} = 70 °C (G) F4TCNQ, T_{film} = 0 °C (H) F4TCNQ, T_{film} = 30 °C (I) F4TCNQ, T_{film} = 70 °C.

3.6.6 Grazing incidence wide angle X-ray scattering (GIWAXS) data

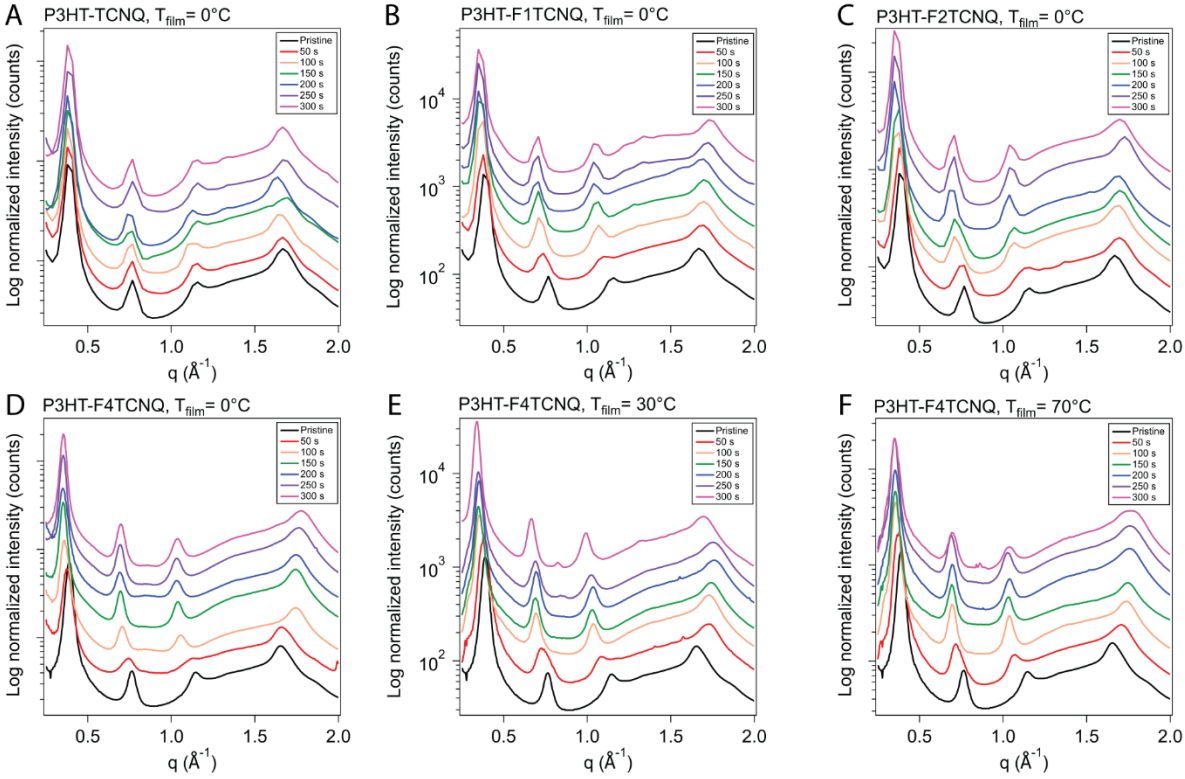

Figure 49. Azimuthal linecuts of GIWAXS of P3HT-FNTCNQ.

Samples were P3HT films doped with FNTCNQ from 0 s to 300 s at 50 s intervals. Linecuts were normalized and spaced to show how the (100) and (020) peaks shift as doping time increased. (A) TCNQ, T_{film} = 0 °C (B) F1TCNQ, T_{film} = 0 °C (C) F2TCNQ, T_{film} = 0 °C (D) F4TCNQ, T_{film} = 0 °C (E) F4TCNQ, T_{film} = 30 °C (F) F4TCNQ, T_{film} = 70 °C.

3.6.7 *In situ* σ experiments for T_{film} = 0 °C, 30 °C, 70 °C for all dopants

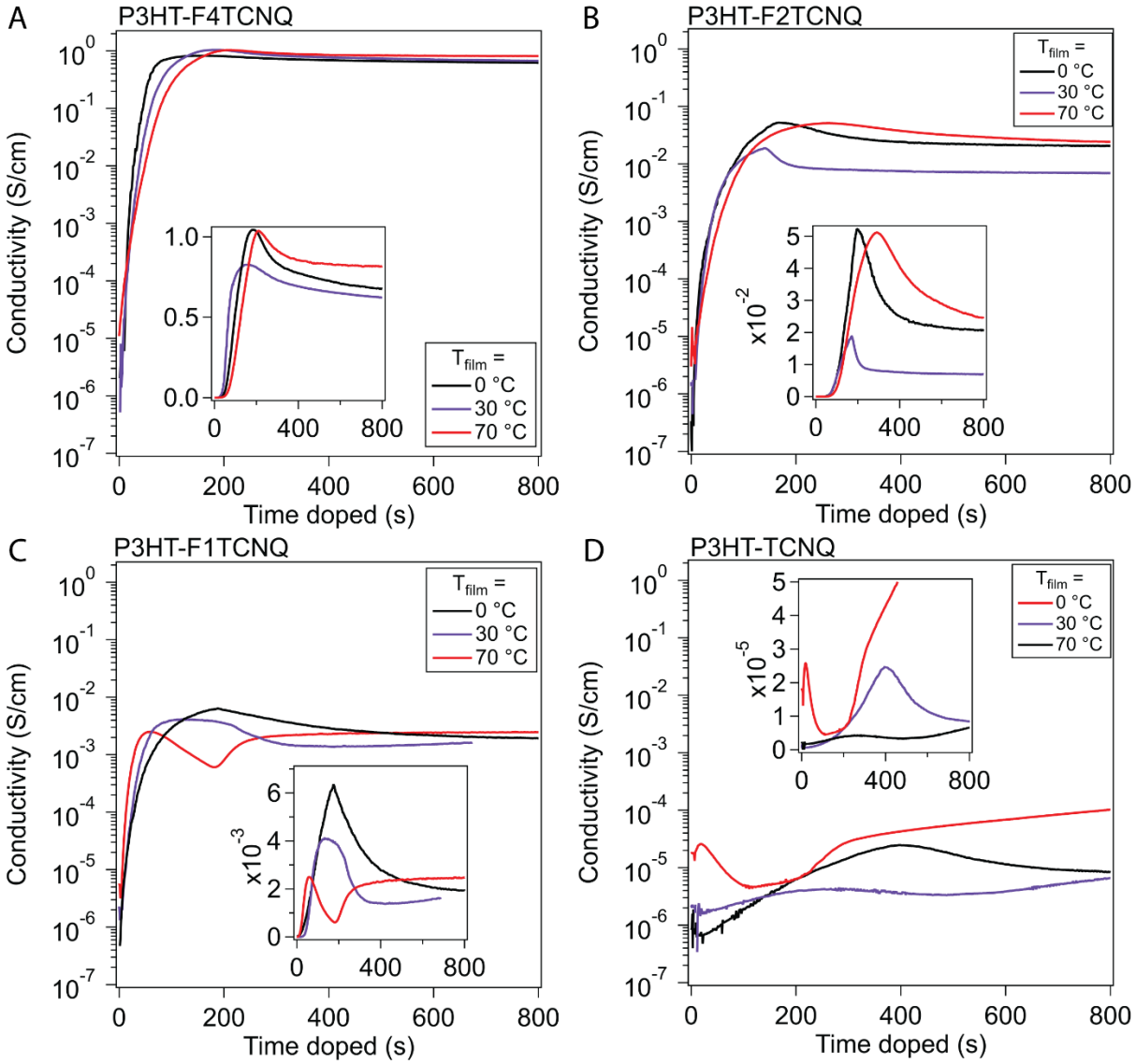

Figure 50. *In situ* σ of P3HT-FNTCNQ for T_{film} = 0, 30, & 70 °C.

(A) P3HT-F4TCNQ (B) P3HT-F2TCNQ (C) P3HT-F1TCNQ (D) P3HT-TCNQ.

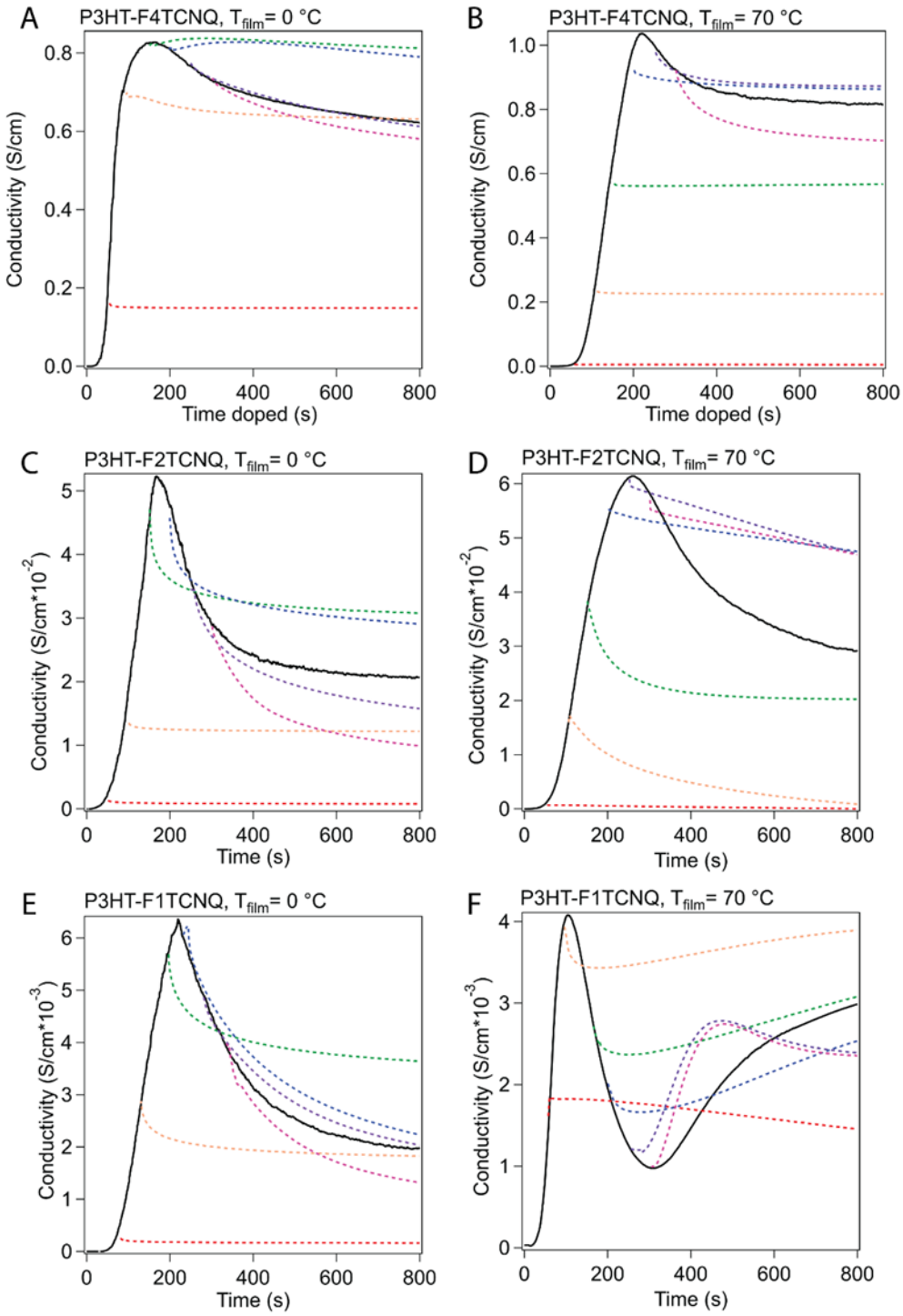

Figure 51. *In situ σ* curtailed experiments of P3HT-FNTCNQ for T_{film} = 0 & 70 °C. (A) F1TCNQ, T_{film} = 0 °C (B) F1TCNQ, T_{film} = 70 °C (C) F2TCNQ, T_{film} = 0 °C (D) F2TCNQ, T_{film} = 70 °C (E) F4TCNQ, T_{film} = 0 °C (F) F4TCNQ, T_{film} = 70 °C.

3.7 Acknowledgements

This work was primarily supported by the University of Chicago Materials Research Science and Engineering Center, which is funded by National Science Foundation under award number DMR-1420709. M.D. acknowledges support from the National Science Foundation through the National Science Foundation Graduate Research Fellowship under grant no. DGE-1746045. This research used resources of the Advanced Photon Source, an Office of Science User Facility operated for the U.S. Department of Energy (DOE) by Argonne National Laboratory under Contract No. DE-AC02-06CH11357. Parts of this work were carried out at the Soft Matter Characterization Facility of the University of Chicago.

3.8 References

1. Salzmann, I., Heimel, G., Oehzelt, M., Winkler, S. & Koch, N. Molecular Electrical Doping of Organic Semiconductors: Fundamental Mechanisms and Emerging Dopant Design Rules. *Acc. Chem. Res.* **49**, 370–378 (2016).
2. Degousée, T. *et al.* High thermal conductivity states and enhanced figure of merit in aligned polymer thermoelectric materials. *J. Mater. Chem. A* **9**, 16065–16075 (2021).
3. Ma, T., Dong, B. X., Grocke, G. L., Strzalka, J. & Patel, S. N. Leveraging Sequential Doping of Semiconducting Polymers to Enable Functionally Graded Materials for Organic Thermoelectrics. *Macromolecules* **53**, 2882–2892 (2020).
4. Yee, P. Y., Scholes, D. T., Schwartz, B. J. & Tolbert, S. H. Dopant-Induced Ordering of Amorphous Regions in Regiorandom P3HT. *J. Phys. Chem. Lett.* **10**, 4929–4934 (2019).
5. Neusser, D. *et al.* High Conductivities of Disordered P3HT Films by an Electrochemical Doping Strategy. *Chem. Mater.* **32**, 6003–6013 (2020).
6. Yedikardeş, B. *et al.* Enhanced Electrical Properties of P3HT:WO3 Hybrid Thin Film Transistors. *J. Electron. Mater.* **50**, 2466–2475 (2021).
7. Vijayakumar, V. *et al.* Bringing Conducting Polymers to High Order: Toward Conductivities beyond 10 5 S cm −1 and Thermoelectric Power Factors of 2 mW m −1 K −2. *Adv. Energy Mater.* **9**, 1900266 (2019).
8. Murrey, T. L. *et al.* Anion Exchange Doping: Tuning Equilibrium to Increase Doping Efficiency in Semiconducting Polymers. *J. Phys. Chem. Lett.* **12**, 1284–1289 (2021).
9. Scholes, D. T. *et al.* The Effects of Crystallinity on Charge Transport and the Structure of Sequentially Processed F 4 TCNQ-Doped Conjugated Polymer Films. *Adv. Funct. Mater.* **27**, 1702654 (2017).

10. Yamamoto, J. & Furukawa, Y. Electronic and Vibrational Spectra of Positive Polarons and Bipolarons in Regioregular Poly(3-hexylthiophene) Doped with Ferric Chloride. *J. Phys. Chem. B* **119**, 4788–4794 (2015).

11. Noriega, R. *et al.* A general relationship between disorder, aggregation and charge transport in conjugated polymers. *Nat. Mater.* **12**, 1038–1044 (2013).

12. Kim, G. H., Shao, L., Zhang, K. & Pipe, K. P. Engineered doping of organic semiconductors for enhanced thermoelectric efficiency. *Nat. Mater.* (2013). doi:10.1038/nmat3635

13. Kiefer, D. *et al.* Double doping of conjugated polymers with monomer molecular dopants. *Nat. Mater.* **18**, 149–155 (2019).

14. Yim, K.-H. *et al.* Controlling Electrical Properties of Conjugated Polymers via a Solution-Based p-Type Doping. *Adv. Mater.* **20**, 3319–3324 (2008).

15. Kroon, R. *et al.* Thermoelectric plastics: from design to synthesis, processing and structure–property relationships. *Chem. Soc. Rev.* **45**, 6147–6164 (2016).

16. Pingel, P. & Neher, D. Comprehensive picture of p-type doping of P3HT with the molecular acceptor F4TCNQ. *Phys. Rev. B* **87**, 115209 (2013).

17. Tietze, M. L. *et al.* Elementary steps in electrical doping of organic semiconductors. *Nat. Commun.* (2018). doi:10.1038/s41467-018-03302-z

18. Jacobs, I. E. *et al.* Polymorphism controls the degree of charge transfer in a molecularly doped semiconducting polymer. *Mater. Horizons* **5**, 655–660 (2018).

19. Venkateshvaran, D. *et al.* Approaching disorder-free transport in high-mobility conjugated polymers. *Nature* **515**, 384–388 (2014).

20. Duong, D. T., Wang, C., Antono, E., Toney, M. F. & Salleo, A. The chemical and structural origin of efficient p-type doping in P3HT. *Org. Electron. physics, Mater. Appl.* (2013). doi:10.1016/j.orgel.2013.02.028

21. Jacobs, I. E. *et al.* Comparison of solution-mixed and sequentially processed P3HT:F4TCNQ films: effect of doping-induced aggregation on film morphology. *J. Mater. Chem. C* **4**, 3454–3466 (2016).

22. Chew, A. R., Ghosh, R., Shang, Z., Spano, F. C. & Salleo, A. Sequential Doping Reveals the Importance of Amorphous Chain Rigidity in Charge Transport of Semi-Crystalline Polymers. *J. Phys. Chem. Lett.* **8**, 4974–4980 (2017).

23. Scholes, D. T. *et al.* Overcoming Film Quality Issues for Conjugated Polymers Doped with F 4 TCNQ by Solution Sequential Processing: Hall Effect, Structural, and Optical Measurements. *J. Phys. Chem. Lett.* **6**, 4786–4793 (2015).

24. Patel, S. N., Glaudell, A. M., Kiefer, D. & Chabinyc, M. L. Increasing the Thermoelectric Power Factor of a Semiconducting Polymer by Doping from the Vapor Phase. *ACS Macro Lett.* **5**, 268–272 (2016).

25. Lim, E., Peterson, K. A., Su, G. M. & Chabinyc, M. L. Thermoelectric Properties of Poly(3-hexylthiophene) (P3HT) Doped with 2,3,5,6-Tetrafluoro-7,7,8,8-tetracyanoquinodimethane (F 4 TCNQ) by Vapor-Phase Infiltration. *Chem. Mater.* **30**, 998–1010 (2018).

26. Lim, E., Glaudell, A. M., Miller, R. & Chabinyc, M. L. The Role of Ordering on the Thermoelectric Properties of Blends of Regioregular and Regiorandom Poly(3-hexylthiophene). *Adv. Electron. Mater.* **5**, 1800915 (2019).

27. Ma, T. *et al.* Correlating conductivity and Seebeck coefficient to doping within crystalline and amorphous domains in poly(3-(methoxyethoxyethoxy)thiophene). *J. Polym. Sci.* **59**, 2797–2808 (2021).

28. Reiser, P. *et al.* Dopant Diffusion in Sequentially Doped Poly(3-hexylthiophene) Studied by Infrared and Photoelectron Spectroscopy. *J. Phys. Chem. C* **122**, 14518–14527 (2018).

29. Liang, Z. *et al.* Influence of dopant size and electron affinity on the electrical conductivity and thermoelectric properties of a series of conjugated polymers. *J. Mater. Chem. A* **6**, 16495–16505 (2018).

30. Jiang, H. *et al.* Tuning of the degree of charge transfer and the electronic properties in organic binary compounds by crystal engineering: a perspective. *J. Mater. Chem. C* **6**, 1884–1902 (2018).

31. Zapata-Arteaga, O. *et al.* Closing the Stability–Performance Gap in Organic Thermoelectrics by Adjusting the Partial to Integer Charge Transfer Ratio. *Macromolecules* **53**, 609–620 (2020).

32. Aubry, T. J. *et al.* Tunable Dopants with Intrinsic Counterion Separation Reveal the Effects of Electron Affinity on Dopant Intercalation and Free Carrier Production in Sequentially Doped Conjugated Polymer Films. *Adv. Funct. Mater.* **30**, 2001800 (2020).

33. Patel, S. N. *et al.* Morphology controls the thermoelectric power factor of a doped semiconducting polymer. *Sci. Adv.* **3**, (2017).

34. Dong, B. X. *et al.* Complex Relationship between Side-Chain Polarity, Conductivity, and Thermal Stability in Molecularly Doped Conjugated Polymers. *Chem. Mater.* **33**, 741–753 (2021).

35. Hu, P., Du, K., Wei, F., Jiang, H. & Kloc, C. Crystal growth, HOMO-LUMO engineering, and charge transfer degree in perylene-FxTCNQ (x = 1, 2, 4) organic charge transfer binary compounds. *Cryst. Growth Des.* (2016). doi:10.1021/acs.cgd.5b01675

36. Sweetnam, S. *et al.* Characterization of the Polymer Energy Landscape in Polymer:Fullerene Bulk Heterojunctions with Pure and Mixed Phases. *J. Am. Chem. Soc.* **136**, 14078–14088 (2014).

37. Acevedo-Peña, P., Baray-Calderón, A., Hu, H., González, I. & Ugalde-Saldivar, V. M. Measurements of HOMO-LUMO levels of poly(3-hexylthiophene) thin films by a simple electrochemical method. *J. Solid State Electrochem.* **21**, 2407–2414 (2017).

38. Gasiorowski, J., Mardare, A. I., Sariciftci, N. S. & Hassel, A. W. Electrochemical characterization of sub-micro-gram amounts of organic semiconductors using scanning droplet cell microscopy. *J. Electroanal. Chem.* **691**, 77–82 (2013).

39. Hamidi-Sakr, A. *et al.* A Versatile Method to Fabricate Highly In-Plane Aligned Conducting Polymer Films with Anisotropic Charge Transport and Thermoelectric Properties: The Key Role of Alkyl Side Chain Layers on the Doping Mechanism. *Adv. Funct. Mater.* **27**, 1700173 (2017).

40. Spano, F. C. Modeling disorder in polymer aggregates: The optical spectroscopy of regioregular poly(3-hexylthiophene) thin films. *J. Chem. Phys.* **122**, 234701 (2005).

41. Spano, F. C. Absorption in regio-regular poly(3-hexyl)thiophene thin films: Fermi resonances, interband coupling and disorder. *Chem. Phys.* **325**, 22–35 (2006).

42. Clark, J., Chang, J.-F., Spano, F. C., Friend, R. H. & Silva, C. Determining exciton bandwidth and film microstructure in polythiophene films using linear absorption spectroscopy. *Appl. Phys. Lett.* **94**, 163306 (2009).

43. Nightingale, J., Wade, J., Moia, D., Nelson, J. & Kim, J.-S. Impact of Molecular Order on Polaron Formation in Conjugated Polymers. *J. Phys. Chem. C* **122**, 29129–29140 (2018).

44. Carbone, P. & Troisi, A. Charge Diffusion in Semiconducting Polymers: Analytical Relation between Polymer Rigidity and Time Scales for Intrachain and Interchain Hopping. *J. Phys. Chem. Lett.* **5**, 2637–2641 (2014).

45. Fontana, M. T. *et al.* Evaporation vs Solution Sequential Doping of Conjugated Polymers: F 4 TCNQ Doping of Micrometer-Thick P3HT Films for Thermoelectrics. *J. Phys. Chem. C* **123**, 22711–22724 (2019).

46. Sharon, D. *et al.* Interrogation of Electrochemical Properties of Polymer Electrolyte Thin Films with Interdigitated Electrodes. *J. Electrochem. Soc.* **165**, H1028–H1039 (2018).

47. Jiang, Z. *et al.* The dedicated high-resolution grazing-incidence X-ray scattering beamline 8-ID-E at the Advanced Photon Source. *J. Synchrotron Radiat.* **19**, 627–636 (2012).

48. B. X. Dong, J. A. Amonoo, G. E. Purdum, Y.-L. Loo and P. F. Green, *ACS Appl. Mater. Interfaces*, 2016, **8**, 31144–31153.

49. S. Sweetnam, K. R. Graham, G. O. Ngongang Ndjawa, T. Heumüller, J. A. Bartelt, T. M. Burke, W. Li, W. You, A. Amassian and M. D. McGehee, J. Am. Chem. Soc., 2014, 136, 14078–14088.

50. J. Hynynen, D. Kiefer and C. Müller, RSC Adv., 2018, 8, 1593–1599.

Chapter 4: Control of amorphous and aggregate domains of P3MEEMT by addition of Li salt

4.1 Abstract

Simultaneously balancing ionic and electronic conduction in self-assembling conjugated polymers is challenging because of the insufficient understanding of the morphology-transport relationship. It is commonly believed that a well-ordered crystalline structure in a conjugated polymer is beneficial for electronic conduction while harmful for ionic conduction. Here we employ mixed ionic/electronic conducting [poly 2,5-dibromo-3-(methoxyethoxyethoxymethyl) thiophene] (P3MEEMT) as our model conjugated polymer and vary thermal processing conditions to control crystalline/amorphous domains in the polymer. P3MEEMT annealed at 180 °C shows stiffer aggregate domains, while P3MEEMT annealed at 135 °C shows stiffer amorphous domains compared to other thermal processed samples, as confirmed by resonance Raman spectroscopy. P3MEEMT annealed at 135 °C exhibits an edge-on orientation with largest coherence crystallite length and largest relative degree of crystallinity compared to other thermal processed P3MEEMT, as confirmed by grazing incidence wide angle X-ray scattering. Ionic conduction is enabled by blending P3MEEMT with lithium bis(trifluoromethanesulfonyl)-imide (LiTFSI) salts. The sample annealed at 135 °C shows the highest ionic conductivity among all other samples at all temperatures, while the quenched sample shows the lowest ionic conductivity at all temperatures. More specifically, the sample annealed at 135 °C has an ionic conductivity of 3.4×10^{-4} S/cm at 100 °C, which is 1.7 times higher than the sample annealed at 180 °C, 2.1 times higher than the as-cast sample, and 3.6 times higher than the quenched sample. These results have profound implications for the understanding, design, and processing of high performance mixed ionic/electronic conducting conjugated polymers for organic electronics.

4.2 Introduction

Conjugated polymers have been studied as candidates for organic electronic devices and energy applications, due to their mechanical flexibility, solution processability, and tunability of their electronic and optical properties via molecular design and synthesis.[1–8] One such design choice is to introduce polar groups into the conjugated polymer sidechains, in particular oligoethylene glycol. Conjugated polythiophenes with oligoethylene glycol sidechains have been studied more intently recently due to their enhanced processability and thermal stability,[9–14] but also have gotten attention as potential strong candidates for mixed ionic and electronic conductivity.[15] Some novel applications for simultaneous electronic and ionic conducting include mechanical actuators, biosensors, and batteries.[16–18]

Both ionic and electronic transport are strongly correlated to the morphology of the polymer. In conjugated polythiophenes, the polymer self-assembles into aggregate/crystalline domains, consisting of tightly packed conjugated backbones, surrounded by a disordered, amorphous matrix.[19] For electronic transport, charge carriers must travel both intra and interchain, with interchain hopping most likely within the aggregate domains, and require transport through the amorphous domains via tie-chains which bridge aggregate domains together.[19–22] Ionic transport in polythiophenes have only been reported on in a limited number of studies, but similarly focus on the polymer morphology as a crucial consideration. These studies focus on poly(3-(methoxyethoxyethoxy)thiophene (P3MEET), poly(3-(methoxyethoxyethoxymethyl)thiophene (P3MEEMT), and polymers like P3MEEMT with reduced oxygen content.[9,11,23] Ionic transport within polymers depends on the ability of the polymer to solvate the ion and transport it from solvation site to solvation site via segmental motion, which has been seen in polymers like polyethylene oxide to be more free within the

amorphous domains.[24,25] Dong *et al.* showed a preference of the solvated ion to reside within the amorphous domains of P3MEET and P3MEEMT at higher salt concentrations.[9] For Onorato *et al.*, their investigation into oligoethylene glycol sidechain permutations and their effects on mixed conduction showed that increasing the oxygen distance from the backbone, which through their simulations showed improved ionic conductivity, improved backbone crystallinity, in turn improving electronic conductivity.[23]

Polymer-based mixed conductors commonly come in a blended architecture where polymers individually with electronic and ionic conductivity are mixed.[26,27] Some effective structures involve block co-polymers, which allow for individual phases of electronic and ionic conductivity to form while existing on the same polymer backbone, and multiphase homopolymers, where the electronic and ionic conduction components are separately mixed together.[28–30] However, these blended architectures come with a highly complex phase-behavior, complicating the control of the morphology for best mixed conduction. Homopolymers with mixed ionic conduction, such as P3MEEMT, combine within themselves the rigid conjugated structure necessary for electronic conductivity and flexible sidechains that promote ionic conductivity, without losing simpler phase behavior. This simplicity allows for controlled thermal treatment of the polymer in order to promote more efficient charge mobility. For example, heating a conjugated polymer above the melting transition of their aggregate/crystalline domains and letting it cool down, or melt recrystallization, of the polymer can allow for better ordering of the conjugated polymer backbone, leading to a larger aggregate content.[31–34]

We want to utilize thermal processing to control the aggregate and amorphous domain structure in our polymer and optimize it to improve our electronic and ionic conductivity. To that end, in this work, we report on a series of thermal treatments of P3MEEMT, which shows multiple thermal

transitions. By adding lithium bis(trifluoromethanesulfonyl)imide (LiTFSI) to P3MEEMT thin films, we show via absorption measurements that this salt addition modifies the resulting polymer microstructure post-thermal treatment: the annealing processes resulted in more rigid and ordered films, whereas the quenched film further disordered the microstructure. Structural characterization of P3MEEMT thin film blended with LiTFSI gave further insight into how the ordered and amorphous domains separately were affected by the thermal treatments. Lastly, we measure ionic conductivity and electronic conductivity for the samples to provide context on how the amorphous and aggregate domain structure help or hinder the conduction of charge carriers. Surprisingly, increased ordering in both the amorphous and aggregate domains, along with long range aggregate-domain alignment, are beneficial for both types of conductivity. It is our belief that this study highlights how careful thermal treatment of polymer films can open new, accessible methods to optimize mixed ionic and electronic conduction for conjugated polymers.

4.3 Results and Discussion

4.3.1 Differential scanning calorimetry reveals multiple thermal transitions

To rationally design thermal processing conditions, we employ differential scanning calorimetry (DSC) to investigate thermal behaviors of P3MEEMT. P3MEEMT was first heated to 220 °C to remove any residual thermal history and kept isothermal at 220 °C for 2 minutes. Then, P3MEEMT was cooled down to -50 °C at a cooling rate of 10 °C/min. **Figure 52** shows the 2nd heating scan of P3MEEMT and three thermal transition peaks are observed. The peak at 144 °C corresponds to the melting temperature (T_m) of polythiophene backbone. The peak at 65 °C is likely the glass transition temperature (T_g) of polythiophene backbone. Notably, the T_g for P3HT ranges from -14 °C to 140 °C depending on the factors such as molecular weight, regioregularity, and inherent limitations of the common T_g characterization techniques.[35] There is a thermal

transition at 121 °C and the assignment of the peak is very challenging. It might be the cold crystallization temperature (T_c) of P3MEEMT due to insufficient crystallization during the cooling scan. To understand the influence of different thermal processing on the formation of crystalline/amorphous domains, different post thermal processing conditions are used according to the thermal transition peaks. More specifically, as-cast, 100 °C annealed, 135 °C annealed, 180 °C annealed and 230 °C quenched P3MEEMT thin films are fabricated for later study.

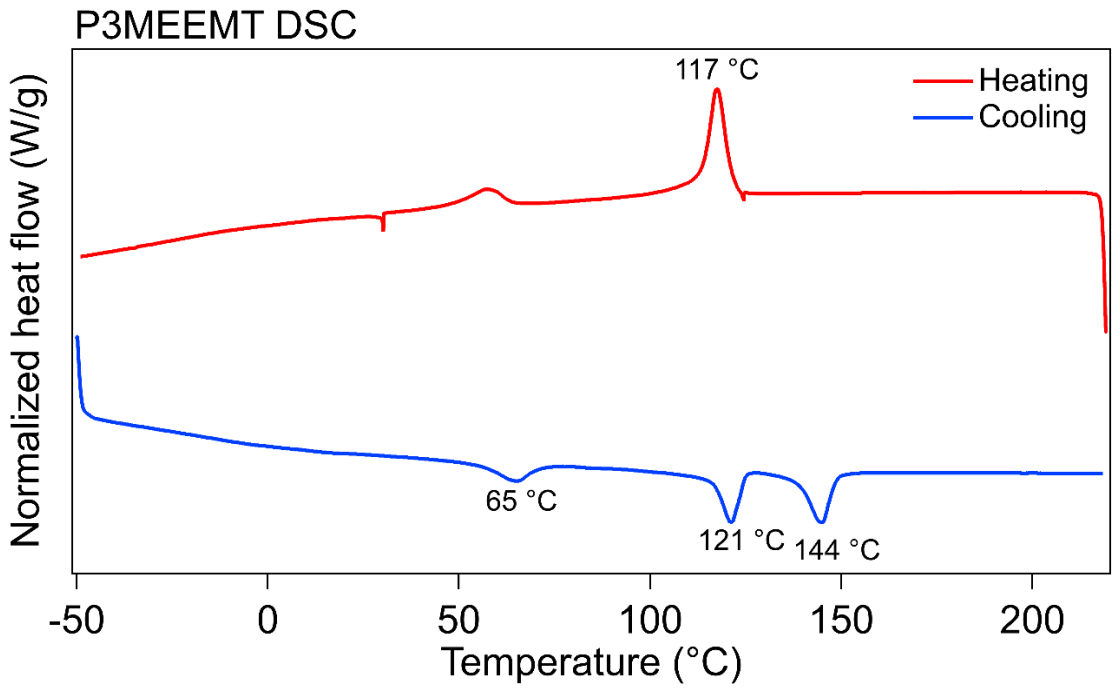

Figure 52. Differential scanning calorimetry (DSC) heating and cooling traces of P3MEEMT at a cooling rate of 10 °C/min.

4.3.2 P3MEEMT absorption measurements show control of microstructure via addition of Li salt

In order to give some context as to how these thermal transitions were affecting the polymer film structure, we conducted UV-Vis-NIR absorption measurements on thin films of P3MEEMT processed to probe each transition, namely an as-cast film, annealed at 100 °C, annealed at 135

°C, annealed at 180 °C, and quenched at 230 °C. Our methodology for spinning these films onto substrates and thermally processing them can be found in the experimental methods section. We also made these films both without salt (r = 0) and with the presence of LiTFSI (r = 0.075, or at a ratio of 1 LiTFSI to 13.3 oxygen atoms), in order to probe how the film structure was affected by the presence of salt. These spectra can be seen within **Figure 53**.

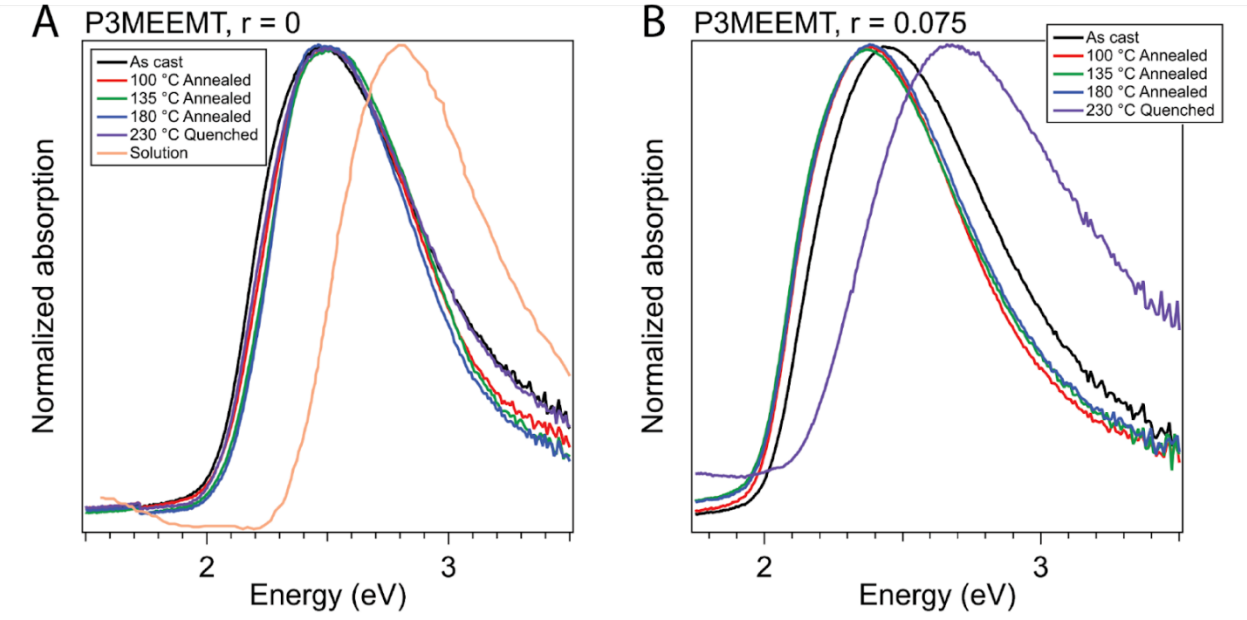

Figure 53. Optical absorption spectra of P3MEEMT.
(A) P3MEEMT with r = 0, both for thin films as-cast, processed by heat via annealing and quenching, as well as in solution. (B) P3MEEMT with r = 0.075 for thin films as-cast and processed via annealing and quenching.

Our main analysis tool for the absorption spectra is the peak value of the main neutral polymer peak around 2.47 eV, and how that peak shifts as the polymer is processed. A shift to higher energy is indicative of worse aggregation and more amorphous character of the polymer film, whereas a red-shift reveals better aggregation and ordering.[36] The P3MEEMT in solution, as expected, shows very little aggregation, and is a good reference point for a P3MEEMT absorption spectra at the amorphous extreme, with a main absorption peak at 2.80 eV. Relative to the film as-cast, films

annealed at 100 °C and 135 °C show very slight blue-shifts, from 2.47 eV to 2.50 eV. The film annealed at 180 °C shows a similar peak location (around 2.47 eV) but has a low-energy shoulder that indicates a higher population of aggregate domains. Lastly, the quenched film shows a similar peak location, but a broader peak, indicating that quenching the film results in some domains that are more aggregate, but also disordering in others.

The polymer films cast with r = 0.075 demonstrate larger shifts in spectra, indicating that the salt plays a role in ordering or disordering the polymer. The film as-cast shows a slight shift down to 2.46 eV, indicating that the presence of Li in the film without any thermal processing helps aggregate the film. All three films that were annealed, 100 °C, 135 °C, and 180 °C annealed, show a more dramatic red-shift to 2.38 eV, indicating that the presence of salt during the annealing process helps promote aggregation. The quenched sample shows the opposite trend, blue-shifting to a much more amorphous 2.69 eV.

The mechanism by which LiTFSI causes the film to become more amorphous during our quenching procedure is well established. The Li ion from LiTFSI is coordinated by five to six ether oxygens, which in our material's case, is present on the polymer sidechains. A single sidechain is incapable of fully solvating the Li ion, so a likely case in our polymer is that sidechains from two neighboring polymer backbones work together to solvate.[9] This, in effect, crosslinks the sidechains together.[37] This crosslinking increases the relaxation time for linked polymer backbones.[38] When we then quench the polymer after increasing its temperature to 230 °C, the increased relaxation time prevents the polymer from ordering and aggregating in time before recrystallizing, resulting in a more amorphous film. From the absorption spectra alone, however, it is less clear how the LiTFSI is causing the annealed P3MEEMT films to order.

4.3.3 Resonance Raman spectroscopy of P3MEEMT demonstrates ordering effects of thermal processing in amorphous and ordered domains.

To give more insight on how the Li ion is inducing chain conformation during our thermal processing, we turn to a technique that allows for individual probing of change in structure in both the amorphous and aggregate domains. As stated in the previous section, the primary peak in the absorption spectra can be broken up into two separate contributions: the low energy peak is attributed to the aggregate domains, whereas the higher energy peak is due the amorphous domains. Resonance Raman spectroscopy, dependent on which features in the absorption spectra match the selected excitation wavelength, can probe specific features in the sample preferentially. For this study, we selected excitation wavelengths of 473 nm, 633 nm, and 785 nm. The 473 nm excitation (2.62 eV) lines up over the amorphous part of our main absorption peak, and so these spectra preferentially probed the amorphous domains. The 633 nm excitation (1.96 eV) aligns with the very rigid, aggregate domains on the low end of the main absorption peak, and thus reflect the changes in the aggregate domains of the polymer film. Lastly, the 785 nm (1.58 eV) is not resonant with any part of the main absorption peak, and thus these measurements reflect the film as a whole with no preference. These excitation wavelengths can be seen overlaid on the absorption spectra in **Figure 54A.**

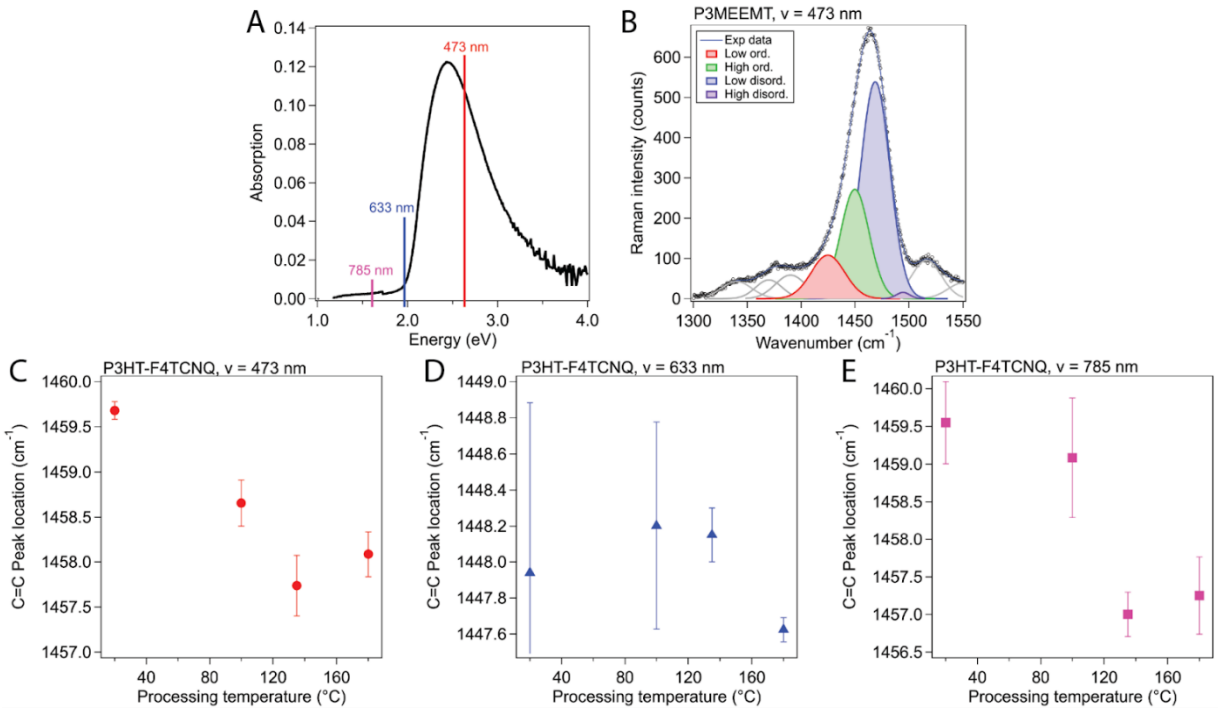

Figure 54. Resonance Raman spectroscopy of P3MEEMT with r = 0.075.
(A) Absorption spectra of thin film P3MEEMT as-cast, along with the excitation wavelengths used for Resonance Raman spectroscopy. (B) Peak fitting schema for P3MEEMT. (C,D,E) Symmetric intraring C=C vibrational mode peak location with 473 nm, 633 nm, and 785 nm excitation wavelength, respectively.

Normalized spectra for as-cast P3MEEMT, as well as annealed at 100 °C, 135 °C, 180 °C, and quenched at 230 °C, can be seen in the appendix in **Figure 63.** To account for differences in thermal treatment methods and film quality, two samples were made for each thermal processing and three spots were used on each sample for spectra. Our main focus was on the intraring symmetric C=C vibrational mode, which shifted between 1447 and 1460 cm^{-1} depending on the excitation wavelength. As reported for P3HT, which shares its backbone chemistry with P3MEEMT, a lower wavenumber for the C=C mode corresponds with an increase in conformational order, *i.e.*, stiffer or more planar chains.

Our main focus with this technique was to track the peak location of the intraring symmetric C=C vibration mode as an indicator of how each thermal treatment ordered or disordered the feature being probed. Our method for quantifying this was by fitting the C=C mode similar to what Nightingale *et al.* do for their P3HT analysis.[39] In the case of P3HT, neutral (*i.e.* uncharged, since this analysis was used for an *in situ* Raman with CV) polymer was split into ordered and disordered peaks. For P3MEEMT, we fit four peaks to the C=C mode for the purpose of taking a weighted average of the peak location with respect to peak area. This fitting, which includes other peaks from 1300 cm^{-1} to 1575 cm^{-1}, can be seen in **Figure 64B**. The C=C mode peak location was calculated with this method for both samples and all three spots and was averaged together. Due to the low number of counts and high amount of noise seen in the spectra from the quenched samples, we were not capable of accurately fitting the spectra from the quenched samples. However, from the normalized spectra seen in the appendix, we can qualitatively state that the peak location for the C=C mode is at a higher wavenumber than for the other four thermal treatments, showing that quenching P3MEEMT with r = 0.075 resulted in more disorder in both the amorphous and aggregate domains of the polymer film.

The result of this C=C peak location analysis can be seen in **Figure 54C, D, and E** for excitation wavelengths of 473 nm, 633 nm, and 785 nm respectively. For the 473 nm excitation wavelength spectra, the C=C peak location appeared within a range of 1457 to 1460 cm^{-1}, indicative of the amorphous nature of the chains preferentially being probed. The as-cast P3MEEMT film showed the most disordered amorphous domain. The 100 °C annealed film shows a slight amount of ordering, with the 135 °C and 180 °C showing the most ordering within the amorphous domain, with a C=C peak location around 1458 cm^{-1}. This appears to indicate that the transition seen in the DSC measurements at 121 °C orders the amorphous phase. The 633 nm

excitation wavelength spectra, which resonates with the very stiff aggregate domains, showed a much lower range of peak locations (1448.2 to 1447.6 cm^{-1}) as expected. Although the as-cast, 100 °C annealed, and the 135 °C annealed show a similar spread of peak locations, the 180 °C annealed sample shows a small variance of peak locations around 1447.6 cm^{-1}. This result serves to confirm our suspicion that the transition seen at 144 °C in the DSC and above 140 °C in our WAXS experiments is affecting our ordered domains, and our films annealed at 180 °C show higher order than those processed at lower temperatures. However, it is worth noting that the ordered domains appear to change less than the amorphous domains, indicating that the change in rigidity is much larger for the amorphous domain when thermally treated above 121 °C than for the aggregate domain above 144 °C. Lastly, for the 785 nm excitation, which is non-resonant and probes the whole film equally, we see a similar trend to that of 473 nm; both films annealed at 135 and 180 °C are stiffer than that of the as-cast film or annealed at 100 °C.

4.3.4 Scattering experiments reveal texturing and grain size change upon thermal processing

To understand how the aggregate domains of P3MEEMT changed with different thermal treatments, grazing incidence wide angle X-ray scattering (GIWAXS) was employed. **Figure 55A-D** show the GIWAXS patterns for neat P3MEEMT and **Figure 55E-H** show the GIWAXS patterns for P3MEEMT at r=0.075. For as-cast P3MEEMT (both r = 0 and r = 0.075), the π-π stacking peak (010) is dominant in the out-of-plane direction and the side chain stacking peak (100) is dominant in the in-plane direction, indicating a face-on orientation (seen in **Figure 55A & E**). For P3MEEMT samples annealed at 100 °C and 180 °C, both (010) and (100) peaks are observed in out-of-plane and in-plane directions, indicating a mixed orientation of both face-on and edge-on (**Figure 55B, D, F, & H**). Interestingly, samples annealed at 135 °C show predominantly edge-on

orientation (**see Figure 55C & G**), where the π-π stacking peak (010) is in the in-plane direction and side chain stacking in the out-of-plane direction. With the addition of LiTFSI salts, the intensities of (010) and (h00) peaks decrease but the featured packing orientation for each sample retains. With thermal processing, higher order side chain peaks are observed. At r = 0, higher order peaks up to (300) are observed in P3MEEMT samples annealed at 100 °C and 180 °C, and higher order peaks up to (400) are observed in P3MEEMT samples annealed at 135 °C. At r = 0.075, although the peak signal decreases, the higher order peaks up to (500) are observed for P3MEEMT samples annealed at 135 °C, indicating a more ordered crystal structure is formed in the 135 °C sample with addition of salt.

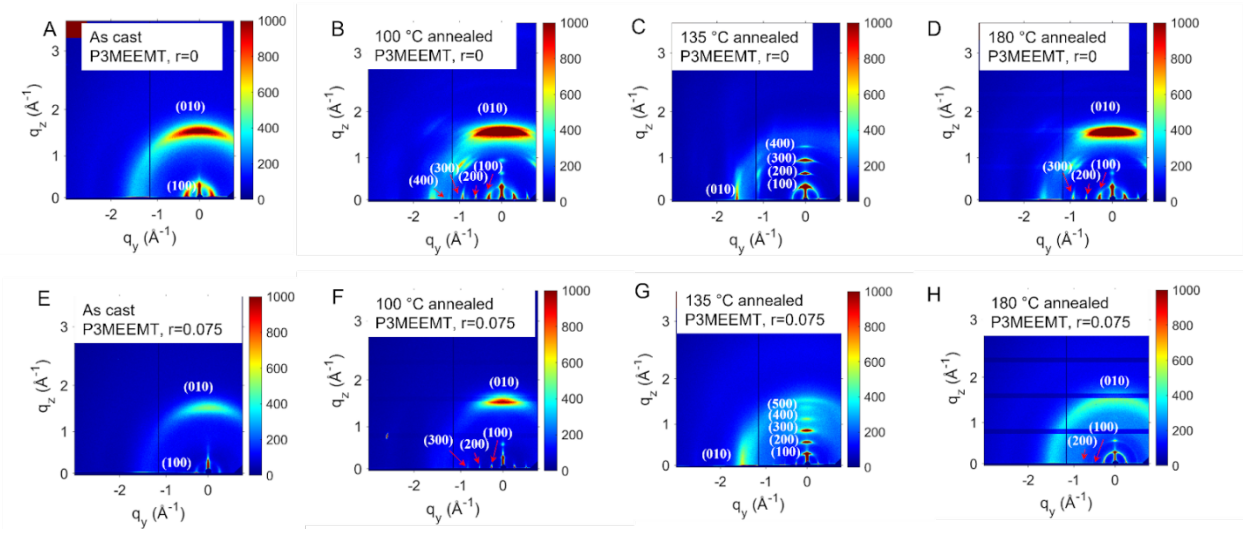

Figure 55. GIWAXS of P3MEEMT.

GIWAXS patterns for (A) as-cast P3MEEMT at r = 0, (B) 100 °C annealed P3MEEMT at r = 0, (C) 135 °C annealed P3MEEMT at r = 0, (D) 180 °C annealed P3MEEMT at r = 0, (E) as-cast P3MEEMT at r = 0.075, (F) 100 °C annealed P3MEEMT at r = 0.075, (G) 135 °C annealed P3MEEMT at r = 0.075, (H) 180 °C annealed P3MEEMT at r = 0.075.

To show how the addition of LiTFSI salts affected the polymer structure, linecuts were performed for P3MEEMT with different thermal treatments. **Figure 65** shows the linecuts for

P3MEEMT at r = 0 and r = 0.075. Since side chain stacking is dominant in the in-plane direction for as-cast P3MEEMT, P3MEEMT annealed at 100 °C and 180 °C, in-plane linecuts are selected, and for P3MEEMT annealed at 135 °C, an out-of-plane linecut is selected. P3MEEMT samples annealed at 135 °C show higher order peaks up to (400) at r = 0 and (500) at r = 0.075, more than compared to other samples. In general, the more higher order peaks are observed, the more ordered crystal structure is formed in P3MEEMT films. The side-chain stacking distances for P3MEEMT samples is shown in **Figure 66**. The side-chain stacking distance for as-cast, 100 °C annealed, 180 °C annealed P3MEEMT is 1.998 nm at r = 0, while for 135 °C annealed sample, the side-chain stacking distance is 1.921 nm. With the addition of LiTFSI salt, LiTFSI infiltrates the side chain and the side-chain stacking expands to 2.234 nm for as-cast and 100 °C annealed samples, 2.302 nm for 180 °C annealed samples, and 2.138 nm for 135 °C annealed samples. P3MEEMT annealed at 135 °C shows shorter side-chain stacking distances compared to other samples.

Since P3MEEMT annealed at 100 °C and 180 °C show a mixed face-on and edge-on orientations, overall linecuts that integrate peak intensity from 85 ° to 2 ° were conducted to better quantify the crystallite length for P3MEEMT samples with different thermal processing. **Figure 56** shows the overall linecuts for P3MEEMT at r = 0 and at r = 0.075. The information about the size of the crystallite is contained in the width of the diffraction peaks. In general, P3MEEMT samples with smaller peak widths and more periodical peaks contain longer crystallites. When the peak widths of periodical diffraction peaks are different, crystallite size in P3MEEMT cannot be calculated only from the full width half maximum (FWHM) of the primary peak using Scherrer equation. Due to the effect of cumulative disorder inside the crystal gains, crystallite size should be calculated by fitting Williamson-Hall plot with FWHM from all periodical peaks.[40] **Figure 67** shows the Williamson-Hall plot and coherence crystallite length (CCL) is calculated using the

following equation: $L_C = \frac{2\pi}{FWHM}$. The resulting CCL for 100 °C annealed P3MEEMT, 135 °C annealed P3MEEMT, and 180 °C annealed P3MEEMT at r = 0 are 39.9 nm, 61.6nm, and 29.9 nm. The resulting CCL for 100 °C annealed P3MEEMT and 135 °C annealed P3MEEMT at r = 0.075 are 41.9 nm and 56.7 nm. CCL for samples with insufficient periodical peaks cannot be calculated. P3MEEMT annealed at 135 °C shows the largest CCL and the CCL is inhibited by the addition of LiTFSI salts.

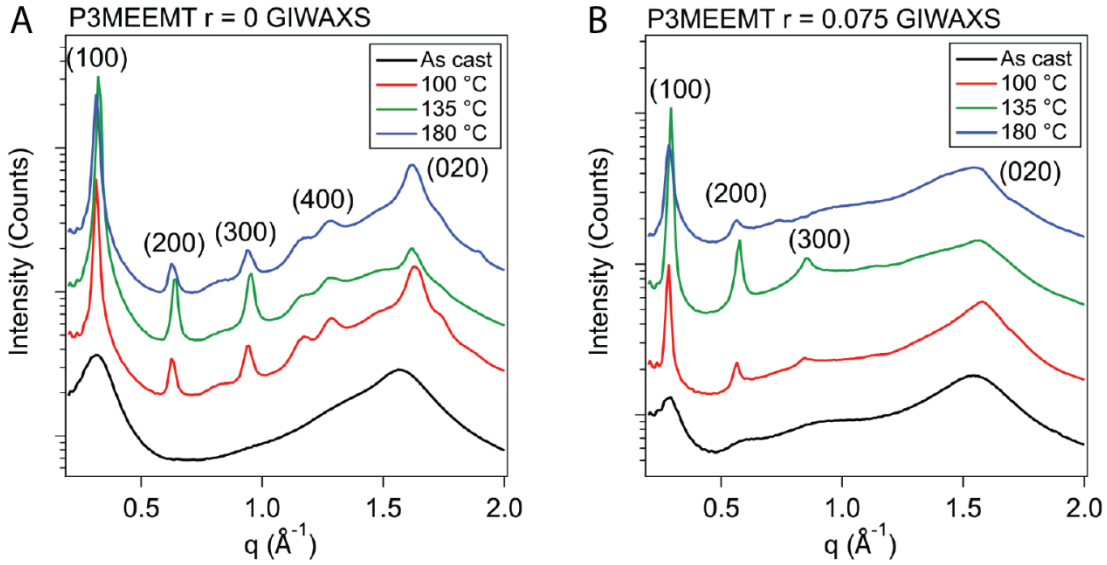

Figure 56. Linecuts for (A) P3MEEMT at r = 0 and (B) P3MEEMT at r = 0.075.

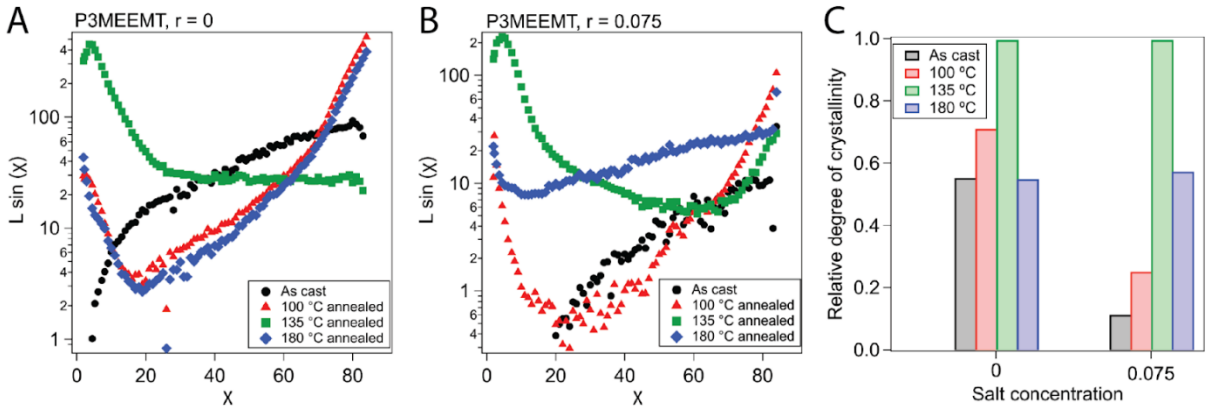

Figure 57. Texture and relative crystallinity of P3MEEMT films.

(Figure 57. Texture and relative crystallinity continued) Partial pole figures of (100) reflection in P3MEEMT at r = 0 (A) and at r = 0.075 (B). (C) The calculated relative degree of crystallinity of P3MEEMT at r = 0 and r = 0.075 with different thermal processing.

To calculate relative degree of crystallinity (rDoC) of P3MEEMT with different thermal processing, partial pole figures of (100) diffraction peaks as a function of the polar angle χ is shown in **Figure 57A & B**. Partial pole figures confirm the edge-on orientation of 135 °C annealed sample and mixed face-on and edge-on orientations for 100 °C and 180 °C annealed samples. As-cast sample only exhibits peak intensity at high polar angle χ, indicating a face-on orientation. RDoC is calculated by integrating the partial pole figures and then normalized by the volume of polymer in polymer-LiTFSI mixtures.[9] Samples annealed at 135 °C show a higher rDOC compared to other thermal processing samples. The rDOC results are consistent with the CCL results. In summary, P3MEEMT samples that are annealed at 135 °C contain preferentially edge-on orientation and they contain the largest CCL and rDOC compared to other samples. **Figure 58** collects the results of our Resonance Raman spectroscopy and GIWAXS analyses for r = 0.075.

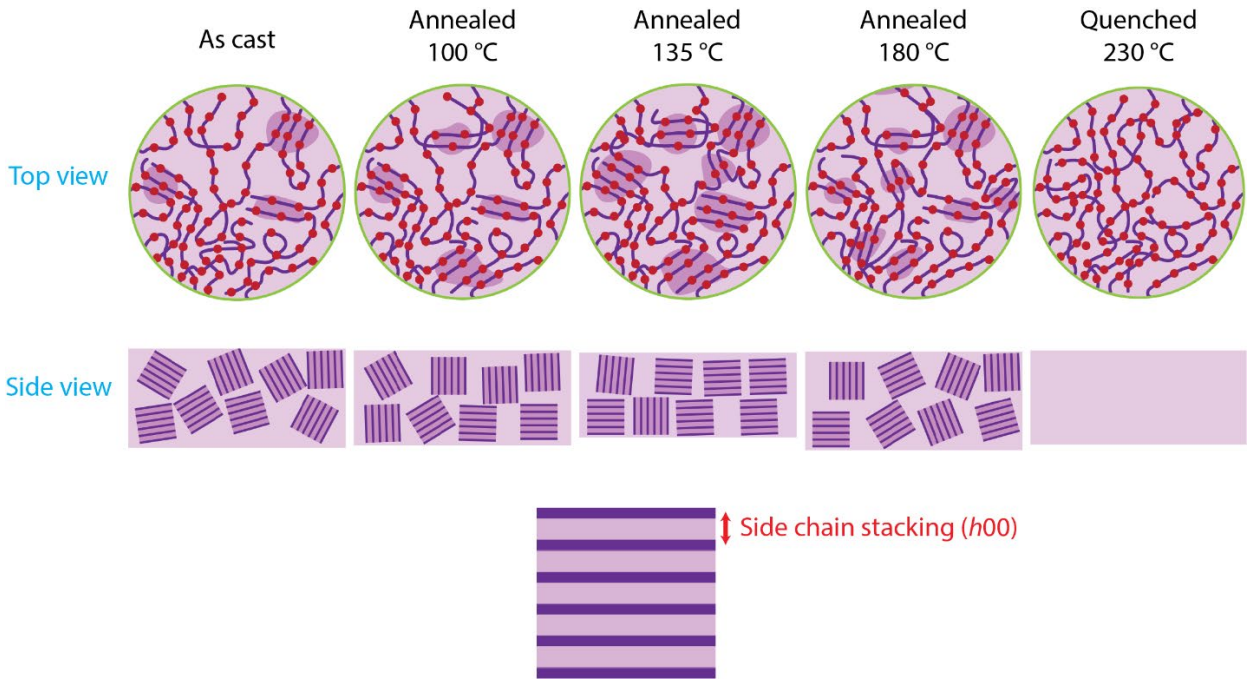

Figure 58. Structural characterization of P3MEEMT with r = 0.075.

Resonance Raman spectroscopy and GIWAXS characterized the order, grain size, and grain alignment of P3MEEMT with r = 0.075 with five different thermal treatments. Compared to the as cast film, all annealed films showed larger aggregate character, but only films annealed at 100 °C and 135 °C and aggregate grain alignment; 100 °C annealed showed stronger face-on and 135 °C showed stronger edge-on. The aggregate grain sizes for 100 °C annealed and 135 °C annealed were larger than as cast, but 180 °C had a smaller grain size, leading to many, smaller misaligned grains. Lastly, 230 °C showed strong amorphous character with low aggregate content.

4.3.5 Ionic conductivity reveals aggregate character beneficial to ionic transport

To probe ionic conductivities of P3MEEMT, polymer samples were spin-coated on top of interdigitated electrode arrays (IDEs) to enable electrochemical impedance spectroscopy (EIS) measurements with high signal-to-noise ratio. The process for fabricating IDEs can be found in our previous report.[40] During the measurement, a small sinusoidal (AC) voltage of known amplitude and frequency was imposed to our polymer film. The ratio and phase relation of the AC voltage and current signal response is the complex impedance Z(jw). In our case, the result of an

impedance spectroscopy experiment is a data set in which ionic conductivity can be extracted via application of a physically-reasonable equivalent circuit. Exemplary Nyquist plots with inserted equivalent circuit are shown in **Figure 59A**. For as-cast P3MEEMT at r=0.075, the Nyquist plots consist of one semicircle and a diffusive tail, indicating only ion conduction in P3MEEMT films. The diameter for the semicircle corresponds to the ionic resistance (R_{ion}). For example, as-cast P3MEET sample measured at 40 °C has a larger diameter than the sample measured at 60 °C. The equivalent circuit used to fit the Nyquist plot includes a resistor (R_s) in series with a resistor (R_{ion}) and a capacitor (C_{sub}) in parallel. R_s refers to resistance from the experimental set up, R_{ion} describes the resistive response from the film, and C_{sub} describes the capacitance of the silicon dioxide substrate. Constant phase elements (CPEs) are added in the equivalent circuit model in place of a capacitor to compensate for non-homogeneity in the system. CPE_f corresponds to the non-uniform transport behavior of the polymer film, and CPE_{int} corresponds to the behavior of the double-layer capacitance near the blocking electrodes.

ElS measurements were performed at 10 °C intervals from 30 °C to 100 °C to avoid the thermal transitions at 121 °C and 144 °C. **Figure 59B** shows the ionic conductivities of P3MEEMT with different thermal treatments. Overall, the annealed samples show higher conductivities than as-cast and quenched samples. The sample annealed at 135 °C shows the highest ionic conductivity among all other samples at all temperatures, while the quenched sample shows the lowest ionic conductivity at all temperatures. More specifically, the sample annealed at 135 °C has an ionic conductivity of 3.4×10^{-4} S/cm at 100 °C, which is 1.7 times higher than the sample annealed at 180 °C, 2.1 times higher than the as-cast sample, and 3.6 times higher than the quenched sample. Given the results from UV-Vis-NIR, Raman, and GIWAXS, the sample annealed at 135 °C exhibits edge-on orientation with the largest crystallite size compared to other annealed samples.

In addition, the amorphous domain in the sample annealed at 135 °C is more rigid and ordered (as evidenced by a low C=C mode peak location with 473 nm excitation wavelength) than other samples, which helps Li^+ better traverse between different grains.

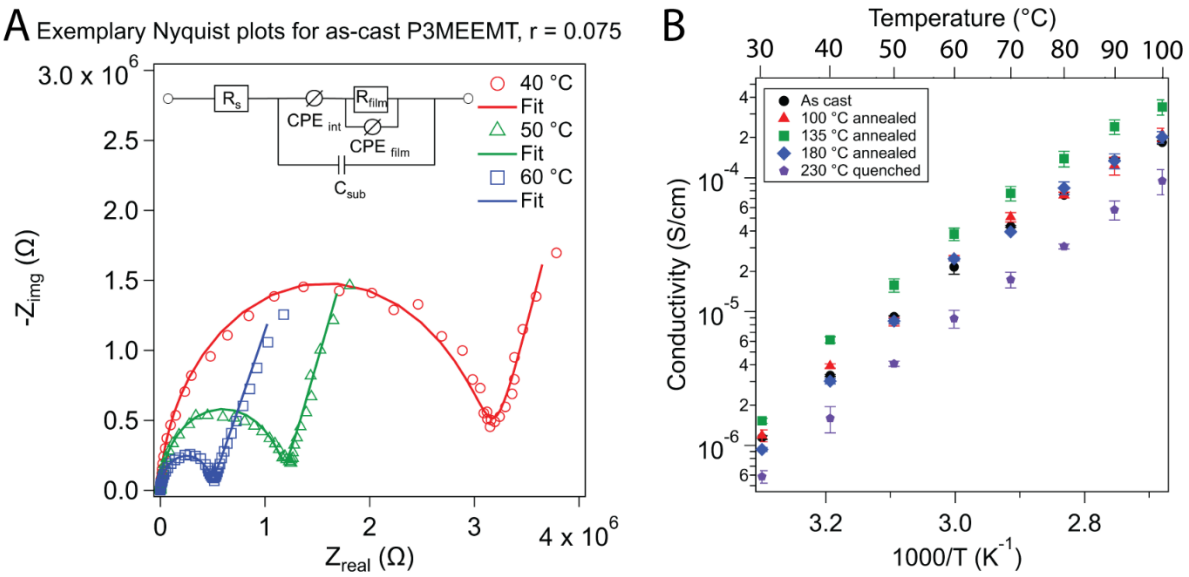

Figure 59. Ionic conductivity of P3MEEMT with r = 0.075.

(A) Exemplary Nyquist plots with an inserted equivalent circuit used for extracting relevant conductivity data for as-cast P3MEEMT at r=0.075. (B) Ionic conductivities of P3MEEMT with different thermal processing. Note: error bars are obtained with n = 3 samples.

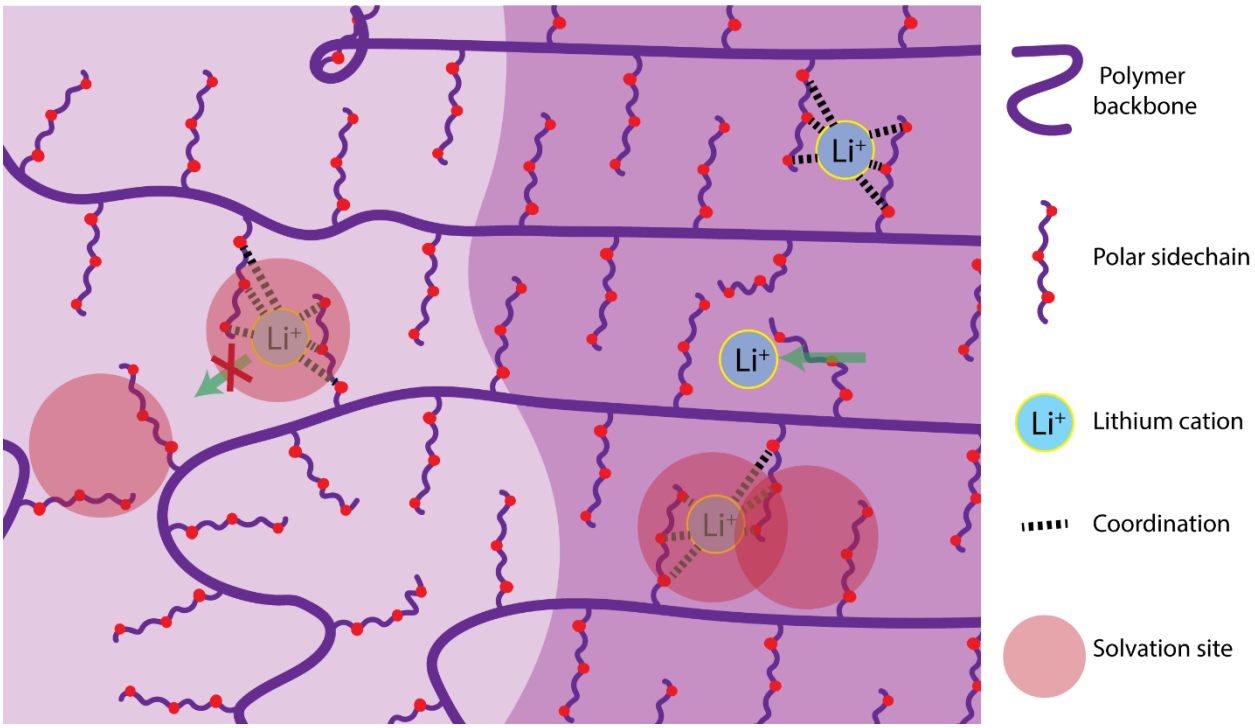

Figure 60. Connectivity of solvation sites within aggregate and amorphous domains. Transport of lithium cations is dependent on connection of the solvation sites, examples of which are highlighted as red circles. These solvation sites overlap well in the aggregate domains, allowing for efficient transport, but are further apart in the amorphous domain, leading to poor ionic mobility.

Counter-intuitively, well-ordered P3MEEMT transports Li^+ faster than amorphous P3MEEMT. For poly (ethylene oxide)-based polymer electrolytes, extensive efforts were made to disrupt the crystallinity and lower the glass transition temperature (T_g) to enhance Li^+ diffusion. Normally, it takes five to six oxygen atoms to coordinate Li^+ from its counter ions such as $TFSI^-$, and Li^+ will transport through three different mechanisms: intrachain hopping, interchain hopping, and co-diffusion with polymer chains. In our case, P3MEEMT only has 3 oxygen atoms on each side chain and Li^+ can only transport through an interchain hopping mechanism, which requires two or more polar side chains. In crystalline domains, polar side chains sit closer to each other than in amorphous domain due to the π-π interaction from polythiophene backbones. Though the side

chain mobility is inhibited in crystalline domains, the solvation shell of Li^+ overlaps with each other and thus, the solvation connectivity is higher than that in amorphous domains. This relation between solvation site connectivity and the aggregate and amorphous domains is depicted in **Figure 60**. The solvation site connectivity has already been proven to play a prominent role in overall ion conductivities in (ethylene oxide)-based polymer electrolytes.[42] It is still poorly understood in conjugated polymer electrolytes. Lastly, it is important to note that the alignment of the aggregate domains is key to good conduction in our EIS experiments. The 135 °C annealed P3MEEMT showed high edge-on alignment. This places the channel of transport, through the polar sidechains of the aggregate domains, parallel to the direction of transport on our interdigitated electrode arrays. Due to this alignment, the 135 °C treated samples showed the highest ionic conductivity. This phenomenon is demonstrated in **Figure 61**. To our best knowledge, this is the first study to show the relationship between crystallinity, alignment of aggregate domains, and Li+ transport for mixed ionic/electronic conductors.

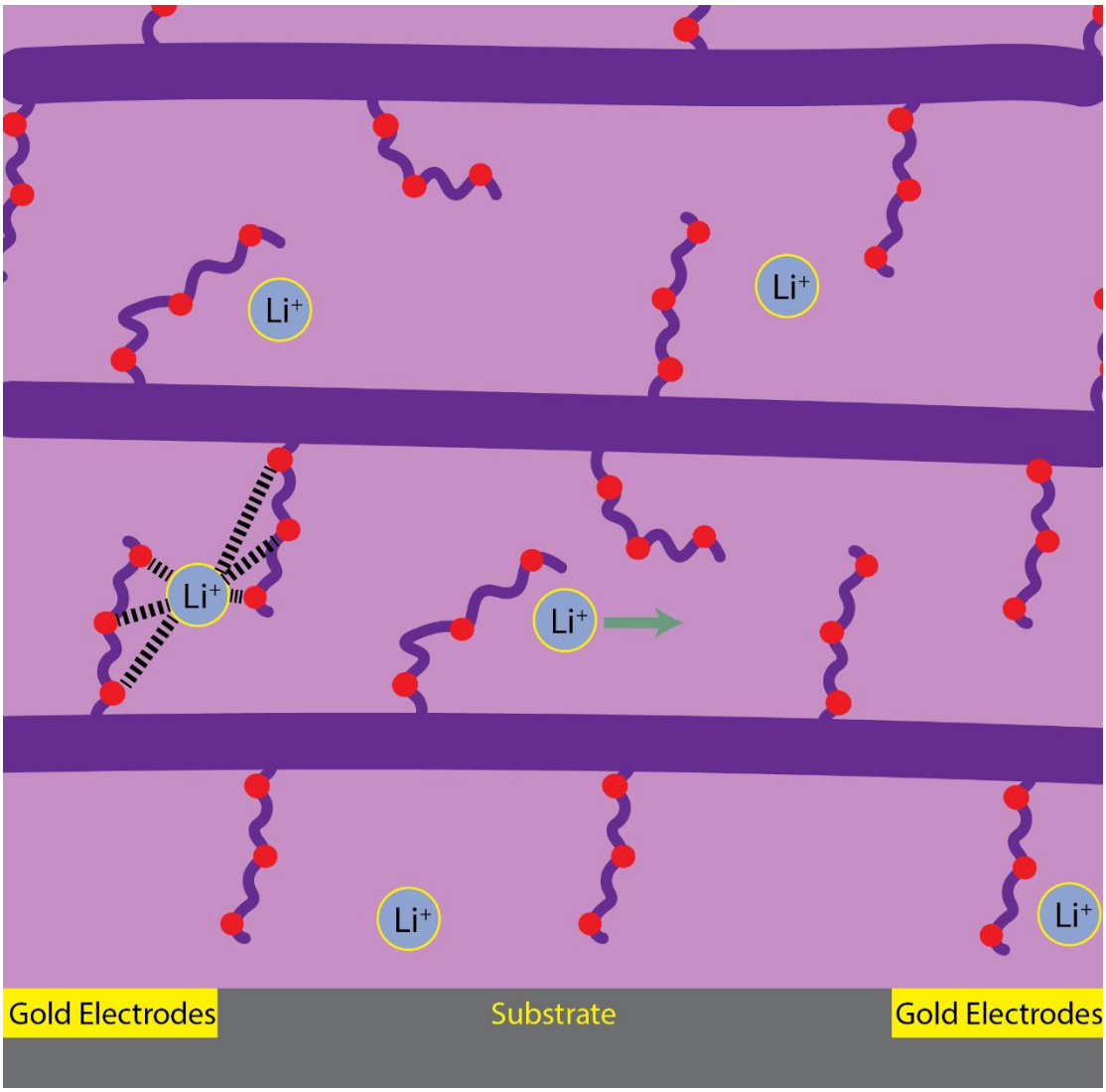

Figure 61. Transport of Li cation during ionic conductivity measurement.

The transport of the Li cation is more facile for edge-on aligned aggregate domains due to the direction of travel being parallel to the interdigitated electrode arrays.

4.3.6 Electronic conductivity shows improvement in annealed P3MEEMT

P3MEEMT films with r = 0.075 as cast, annealed at 135 °C, and quenched at 230 °C were tested via *in situ* electronic conductivity experiments to determine the viability of mixed electronic and ionic conduction were in P3MEEMT with different thermal treatments. Electronic conductivity in conjugated polythiophenes like P3MEEMT are known to have a preference for

highly aggregate polymers, since the rate-limiting step for electronic charge transport is interchain, which occurs most quickly within the aggregate domains.[19] We hypothesized, due to ionic conductivity also preferring more ordered microstructure, that the annealed P3MEEMT with higher order would provide an intriguing candidate for mixed ionic and electronic conduction. These *in situ* electronic conductivity experiments were conducted within an apparatus that could measure the conductivity of the polymer film as it was being vapor doped. Our dopant of choice for these experiments was nitrosonium hexafluorophosphate (NOPF6), as its electron affinity is strong enough to reliably react and introduce a charge carrier with P3MEEMT.

Figure 62 shows the results of the *in situ* electronic conductivity experiments. All three samples showed a strong reaction to NOPF6, which increased its conductivity over six orders of magnitude in about fifty seconds of exposure. The highly amorphous film, 230 °C quenched, showed a lower conductivity than either other film, and the more aggregate 135 °C quenched film had the highest maximum conductivity. Both films of higher amorphous content (as cast, 230 °C quenched) showed high instability when doped past a maximum conductivity; the as cast film was taken off the dopant past this maximum, at which point it stabilized out. The 135 °C annealed film, by comparison, showed much more stability even at very high doping times. These *in situ* experiments demonstrate that the aggregate, annealed films are conducive to both high ionic and electronic conductivity.

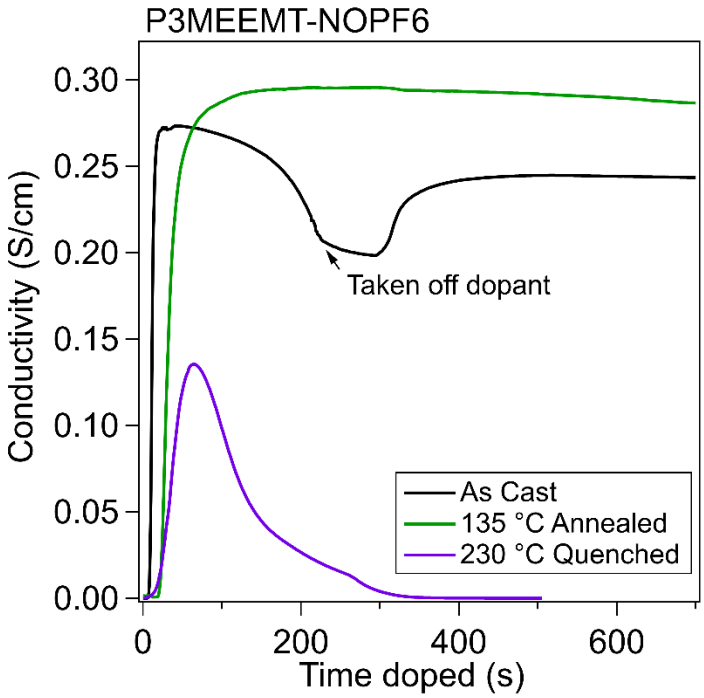

Figure 62. *In situ* conductivity of P3MEEMT-Nitrosonium Hexafluorophosphate.

The electronic conductivity of P3MEEMT with three different processings (as cast, annealed at 135 °C, quenched at 230 °C) was measured as it was being vapor doped by Nitrosonium Hexafluorophosphate.

4.4 Conclusion

This study investigated a conjugated polymer, P3MEEMT, which displayed multiple thermal transitions that, along with the usage of LiTFSI and thermal processing, allowed us to control the amorphous and aggregate domain structure. This was potentially significant, due to P3MEEMT's role as a candidate for mixed electronic and ionic conduction, which is highly affected by the microstructure and morphology of the material. Differential scanning calorimetry revealed thermal transitions at 64 °C, 121 °C and 144 °C, prompting creation of thin film samples annealed at 100 °C, 135 °C, and 180 °C, along with a sample quenched at 230 °C and an as-cast sample. Using UV-Vis-NIR spectroscopy, we expected to see that our annealed samples exhibit a higher degree of order, and our quenched sample to show more amorphous character. However, the absorption

spectra revealed that these samples' microstructure were rather similar to each other. After adding LiTFSI salt, which is necessary to promote ions for ion conduction, we found that at r = 0.075 that these thermal treatments prompted a much stronger reaction, ordering the annealed films and making the quenched film much more amorphous. The interaction of the Li cation with the polymer backbone appeared to be influencing how the thermal treatments changed the polymer film's structure.

Utilizing Resonance Raman spectroscopy, we were able to explore how the thermal treatments were affecting the polymer amorphous and aggregate regimes separately, as well as the film as a whole. The 135 °C thermal treatment and 180 °C treatment appeared to induce order in the amorphous domain, whereas the 180 °C treatment was required to order the aggregate domain. We further probed the aggregate domains of our film by using grazing incidence wide angle X-ray spectroscopy (GIWAXS), both with and without the presence of Li cations. We found that the 100 °C and 180 °C treatments at r = 0 induced a mix of edge-on and face-on textures, whereas the 135 °C treatment preferentially preferred edge-on orientation. For r = 0.075, the 180 °C appeared to have a more isotropic texture, the 100 °C more face-on, and 135 °C more edge-on with slightly more face-on than at r = 0. Analyzing these textures in the GIWAXS scattering showed that the treatment at 135 °C gave a higher relative degree of crystallinity at both r = 0 and r = 0.075. The 180 °C transition appeared to also induce smaller crystalline coherence lengths (*i.e.* the size of the aggregate domains) both with and without salt, whereas the 135 °C transition appeared to have the largest.

We then measured the ionic conductivity of the P3MEEMT samples with r = 0.075 using electrochemical impedance spectroscopy measurements. We found that, surprisingly, the most amorphous sample, which is usually thought to be conducive to the best ionic conduction,

demonstrated the lowest ionic conductivity. This measurement also differentiated between films annealed at 135 °C and 180 °C, which had similar aggregate/amorphous character. We have seen through previous experiments with P3MEEMT and other similar polythiophenes with polar sidechains that the solvation site connectivity within the aggregate domain was important for efficient ionic transport. The preferentially edge-on texture of 135 °C treated film appears to provide channels for ion conduction through the plane of the polar sidechains of the aggregate regime, as opposed to the isotropic as-cast and 180 °C treatment texture or the preferentially face-on 100 °C.

Our results have demonstrated that thermal processing can be effective for tuning aggregate/amorphous domains in P3MEEMT, and Li^+ transport is proven to be more efficient in crystalline domains than in amorphous domains mainly due to the solvation sites connectivity of the polar side chains. The edge-on orientation of P3MEEMT is also beneficial for facile Li^+ transport because it is coplanar with the electrical field. The morphology-transport property relationship shows that it is possible to optimize ionic and electronic conduction by controlling polymer structure on both a local and long-range scale. Our strategy of simultaneously promoting both ionic and electronic conduction in conjugated polymers provides new design principles for organic thermoelectrics, organic electrochemical transistors and other electrochemical conversion and storage devices.

4.5 Experimental methods

4.5.1 Materials and sample preparation

The procedure of synthesizing P3MEEMT can be found in our previous report. P3MEEMT solution used to prepare thin film samples was made by dissolving P3MEEMT in anhydrous acetonitrile at a concentration of 10 mg/mL and stirred overnight. The solution was then filtered

with a 0.45 μm filter. Bis(trifluoromethane)-sulfonimide lithium salt (LiTFSI) was dissolved in anhydrous acetonitrile at a concentration of 10 mg/mL. The solutions of P3MEEMT and LiTFSI were then mixed to reach r=$[Li^+]$/[EO] =0.075. The mixed solution was then stirred for two hours. Before depositing polymer materials, all substrates used in the experiments were cleaned by ultrasonication in acetonitrile and 2-propanol for ten minutes. The mixed solution was then used for spin-coating different substrates at 2000 rpm for two minutes under argon atmosphere. The thickness of the coated film is *ca.* 48 nm as confirmed by the ellipsometer. UV-vis and resonance Raman spectroscopy measurements were performed on P3MEEMT thin films deposited on glass substrates. Grazing incidence wide-angle X-ray scattering and spectroscopic ellipsometry measurements were performed on P3MEEMT thin films deposited on Si substrates with 1.5 nm SiO_2 layer. Electrochemical impedance spectroscopy measurements were performed on interdigitated electrode arrays with 1 μm SiO_2 supporting layer.

4.5.2 Ellipsometry

J.A. Woollam alpha-SE spectroscopic ellipsometer was used to measure P3MEEMT film thicknesses. A Cauchy layer model was used to derive the thicknesses and optical properties of polymer thin films. Thickness of P3MEEMT was measured to be *ca.* 48 nm.

4.5.3 Differential scanning calorimetry

DSC measurements were conducted on a TA Instruments Discovery 2500 at a scanning rate of 10 °C/min within the temperature range from -50 °C to 230 °C. Second heating scan was recorded and the thermal transition temperatures were determined by the peak positions in the DSC trace. The sample was kept under a nitrogen environment during the experiment.

4.5.4 UV-Vis-NIR absorption spectroscopy

UV-VIS-NIR spectra of neat P3HT and vapor-doped thin films on quartz substrates were obtained using the Shimadzu UV-3600 Plus UV-VIS-NIR Dual Beam Spectrophotometer housed in the Soft Matter Characterization Facility (SMCF) (Pritzker School of Molecular Engineering, University of Chicago). Measurements were taken within a wavelength range of 250 to 2480 nm.

4.5.5 Resonance Raman spectroscopy

Raman spectroscopy experiments were performed under ambient conditions using the Horiba LabRAM HR Evolution NIR confocal Raman microscope housed in the Chicago Materials Research Center. Raman spectra of neat and doped P3HT thin films was collected using a 100× objective and 473 nm, 633 nm, and 785 nm wavelength lasers. Laser power and was set to 1% for 473 nm, 1% for 633 nm, and 10 % for 785 nm wavelength to minimize local heating and material degradation. Spectra were taken between a wavenumber range of 1149 to 1746 cm^{-1} for 473 nm excitation, 894 to 1975 cm^{-1} for 633 nm excitation laser, 1116 to 1771 cm^{-1} for 785 nm excitation laser.

4.5.6 Grazing incidence wide angle X-ray scattering

GIWAXS experiments were conducted at the Advanced Photon Source (Argonne National Laboratory) at beamline 8-ID-E. The energy of the incident beam was at 10.91 keV, and a Pilatus 1MF pixel array detector (pixel size = 172 mm) was used. The measurement time for one image was 10 seconds. All samples were placed and measured in a low vacuum chamber (10^{-3} mbar) to reduce the air scattering as well as to minimize beam radiation damage. There are multiple rows of inactive pixels between the detector modules when the images were collected at one position. To fill these inactive gaps, the detector was moved down to a pre-set new position along the vertical direction after each measurement. After the image was collected at the new spot, the data from these two detector positions were combined using the GIXSGUI package for MATLAB to fill the

inactive gaps. The absence of artifacts in the combined image demonstrates that the scattering from the sample does not change during the exposure. The GIXSGUI package was also used to output the GIWAXS signals as intensity maps in (q_r, q_z) space, and take the linecuts along out-of-plane (q_z) and in-plane directions (q_r). GIWAXS images of thin films were taken at a grazing incident x-ray angle of 0.14°, which is above the critical angle of the polymer film and below the critical angle of the silicon substrate.

To construct the pole figure of the (100) reflection in each sample, wedge cuts with an angular breadth of 1° were extracted from GIWAXS images, performed using the GIXSGUI. Each wedge cut was first fit to an empirical baseline function to enable the background intensity and amorphous scattering to be subtracted. Full width half maximum (FWHM) of periodic peaks are extracted by fitting the peaks with a Gaussian function. The Williamson-Hall plot was made by linearly fitting the FWHM values with periodical numbers (m). Additional information can be found elsewhere.[43]

4.5.7 Electrochemical impedance spectroscopy (EIS)

Electrochemical impedance spectroscopy measurements were performed on top of interdigitated electrode arrays (IDEs) with 1 μm SiO_2 supporting layer using Gamry 600+ potentiostat inside an argon-filled glove box. The fabrication details can be found in our previous report.[41] The EIS was measured from 1 MHz to 0.1 Hz at different temperatures. The ionic resistance (R_i) data were then extracted from the impedance spectrum by fitting an equivalent circuit shown in the discussion section. The ionic conductivity σ_i of the thin film sample was calculated using the following equation:

$$\sigma_i = \frac{1}{R_i} * \frac{d}{l(N-1)h}$$

R_i = ionic resistance

d = spacing between adjacent electrode teeth, 8 µm

l = length of the electrode, 1000 µm

N = number of electrodes, 160

h = thickness of the film

4.5.8 *In situ* electronic conductivity

For the *in situ* conductivity measurements, a specialized setup was fabricated for control and precision of measurement. A steady-state temperature is achieved using a thermoelectric module. For these experiments, the temperature of the polymer film was held at 0 °C, and the dopant nitrosonium hexafluorophosphate was held at 35 °C. The sample was held in place by two electrode probes, which allows for electrical contact with the sample during vapor doping. A more detailed description and visuals can be found in chapter 2.

4.6 Appendix

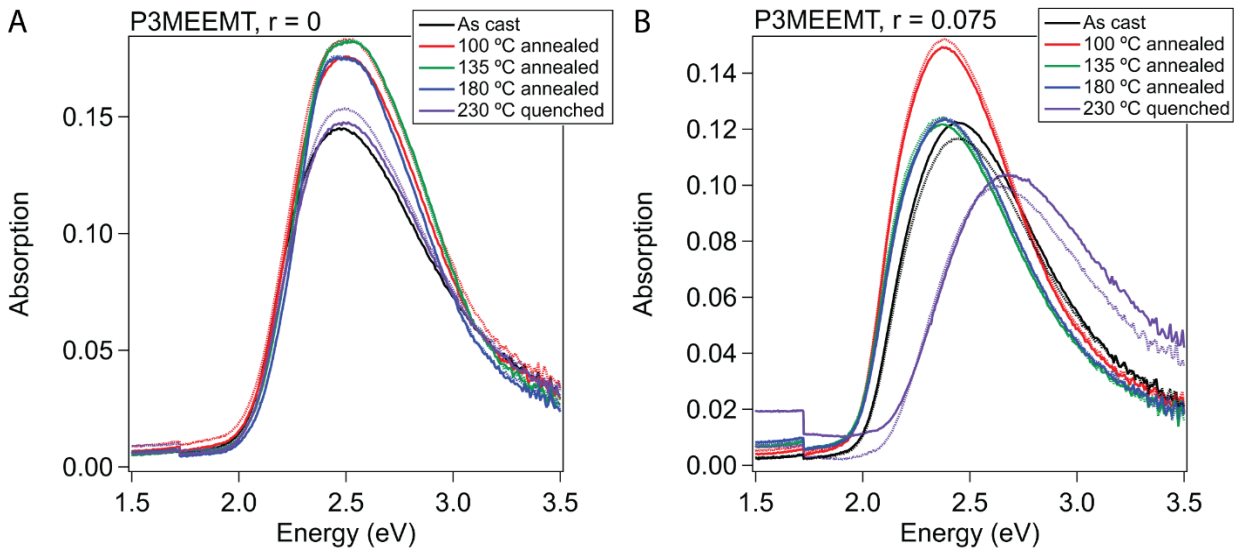

Figure 63. Raw spectra from UV-Vis-NIR spectroscopy of P3MEEMT as cast and thermally treated (100 °C, 135 °C, 180 °C annealed, and 230 quenched).
(A) P3MEEMT with r = 0, (B) P3MEEMT r = 0.075.

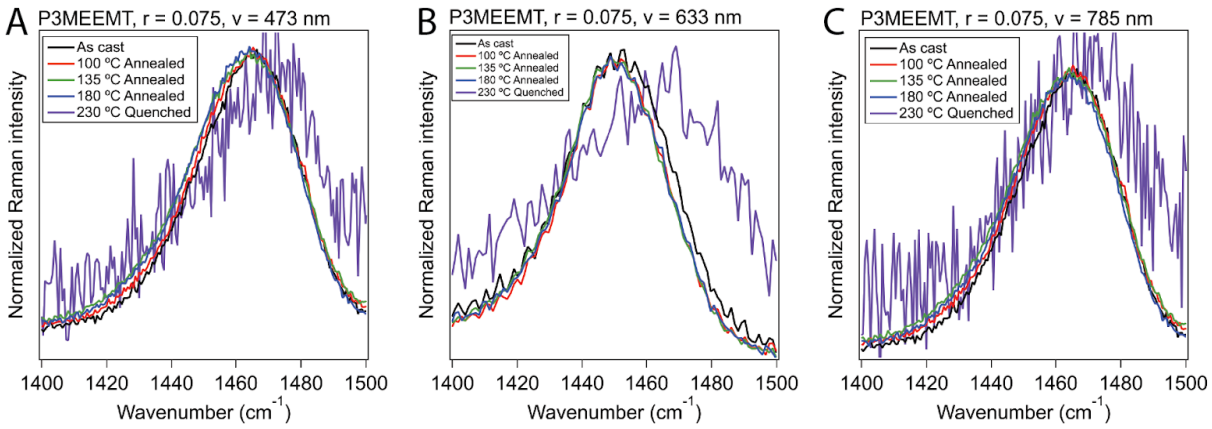

Figure 64. Normalized Raman spectra of P3MEEMT with r = 0.075.

Spectra are taken for as cast, 100 °C annealed, 135 °C annealed, 180 °C annealed, and 230 °C quenched for (A) 473 nm excitation wavelength, (B) 633 nm excitation wavelength, and (C) 785 nm excitation wavelength.

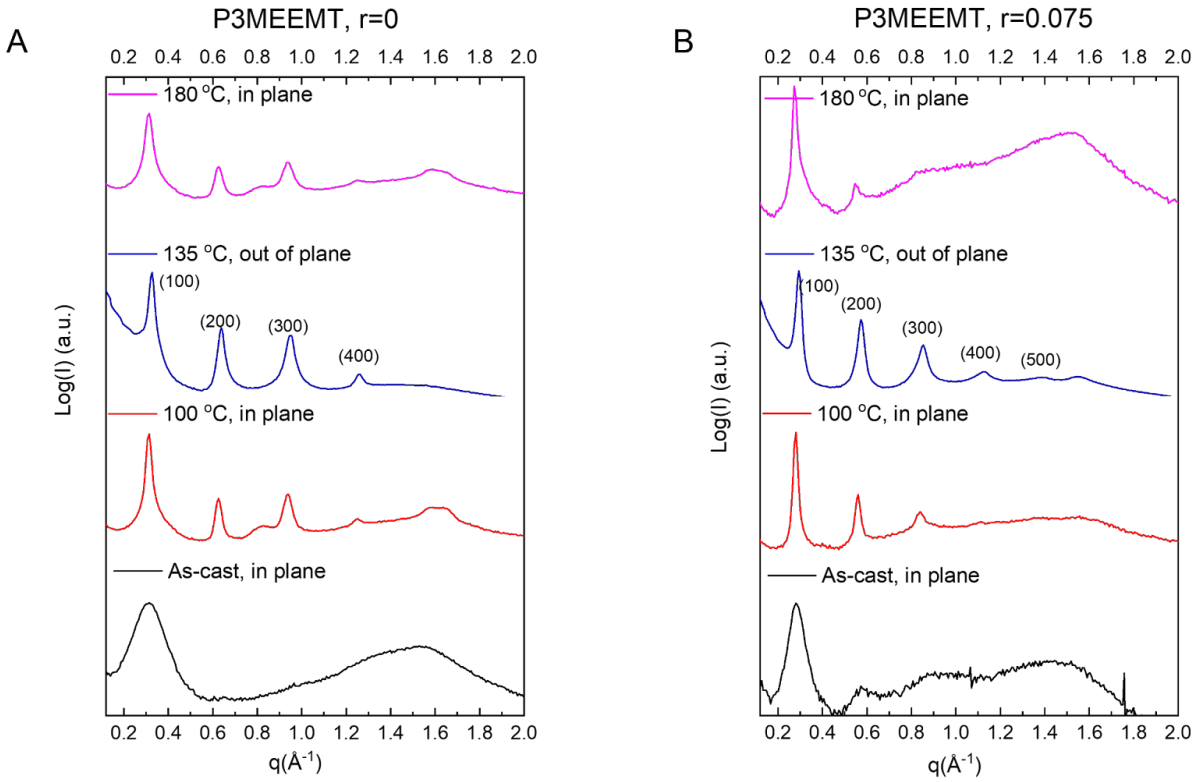

Figure 65. Linecuts for (A) P3MEEMT at r = 0 and (B) P3MEEMT at r = 0.075.

Linecuts for different samples were chosen based on the intensity of side chain stacking. For example, 135 °C annealed sample shows edge-on orientation so the intensity of side chain stacking

(Figure 65. Linecuts for P3MEEMT continued) is higher in out-of-plane direction than in-plane direction. Thus, the linecut was made from the GIWAXS pattern in out-of-plane direction to amplify the side chain stacking.

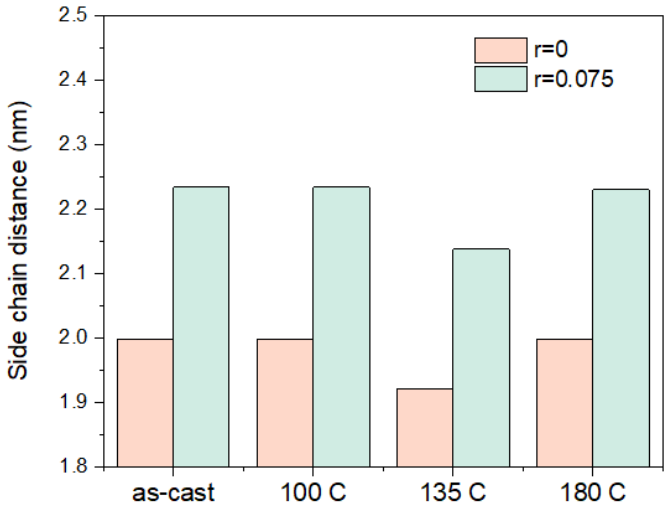

Figure 66. (100) side-chain stacking distance of P3MEEMT with different thermal processing.

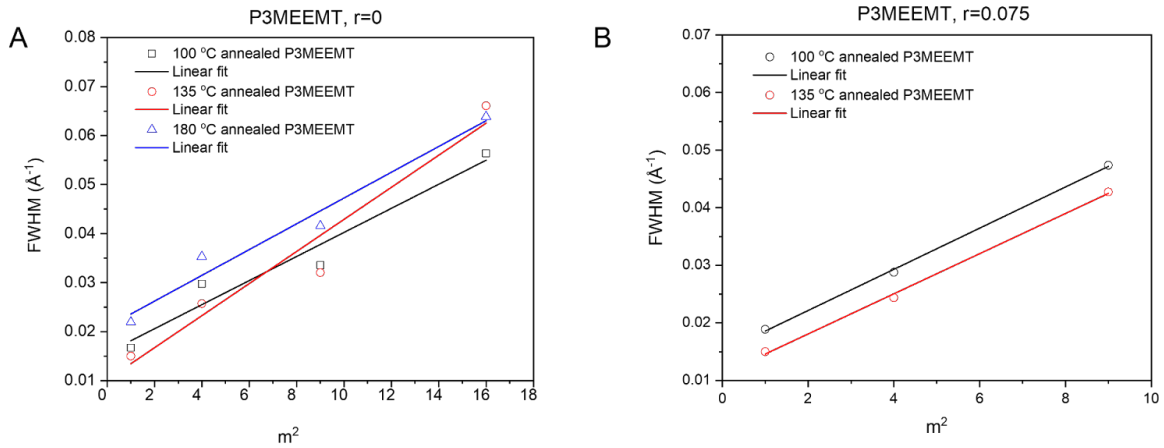

Figure 67. Williamson-Hall plot for P3MEEMT at (A) r = 0 and at (B) r = 0.075

4.7 Acknowledgements

This work was funded in part through NSF DMREF award number 1922259. M.D. acknowledges support from the National Science Foundation through the National Science Foundation Graduate Research Fellowship under grant no. DGE-1746045. This research used resources of the Advanced Photon Source, an Office of Science User Facility operated for the U.S. Department of Energy (DOE) by Argonne National Laboratory under Contract No. DE-AC02-06CH11357. Part of this work was performed at the Soft Matter Characterization Facility of the University of Chicago. This work made use of the Pritzker Nanofabrication Facility of the Pritzker School of Molecular Engineering at the University of Chicago, which receives support from Soft and Hybrid Nanotechnology Experimental (SHyNE) Resource (NSF ECCS-1542205), anode of the National Science Foundation's National Nanotechnology Coordinated Infrastructure. This work made use of the shared facilities at the University of Chicago Materials Research Science and Engineering Center, supported by National Science Foundation under award number DMR-2011854.

4.8 References

1. M. Goel and M. Thelakkat, *Macromolecules*, 2020, **53**, 3632–3642.
2. T. L. D. Tam and J. Xu, *J. Mater. Chem. A*, 2021, **9**, 5149–5163.
3. S. N. Patel, A. E. Javier, G. M. Stone, S. A. Mullin and N. P. Balsara, *ACS Nano*, 2012, **6**, 1589–1600.
4. H. Dong, X. Fu, J. Liu, Z. Wang and W. Hu, *Adv. Mater.*, 2013, **25**, 6158–6183.
5. H. Sirringhaus, *Adv. Mater.*, 2014, **26**, 1319–1335.
6. C. N. Hoth, P. Schilinsky, S. A. Choulis and C. J. Brabec, *Nano Lett.*, 2008, **8**, 2806–2813.
7. T. Sekitani, U. Zschieschang, H. Klauk and T. Someya, *Nat. Mater.*, 2010, **9**, 1015–1022.
8. J.-H. Bahk, H. Fang, K. Yazawa and A. Shakouri, *J. Mater. Chem. C*, 2015, **3**, 10362–10374.
9. B. X. Dong, C. Nowak, J. W. Onorato, J. Strzalka, F. A. Escobedo, C. K. Luscombe, P. F. Nealey and S. N. Patel, *Chem. Mater.*, , DOI:10.1021/acs.chemmater.8b05257.

10. T. Ma, B. X. Dong, J. W. Onorato, J. Niklas, O. Poluektov, C. K. Luscombe and S. N. Patel, *J. Polym. Sci.*, 2021, **59**, 2797–2808.

11. B. X. Dong, C. Nowak, J. W. Onorato, T. Ma, J. Niklas, O. G. Poluektov, G. Grocke, M. F. DiTusa, F. A. Escobedo, C. K. Luscombe, P. F. Nealey and S. N. Patel, *Chem. Mater.*, 2021, **33**, 741–753.

12. D. Kiefer, R. Kroon, A. I. Hofmann, H. Sun, X. Liu, A. Giovannitti, D. Stegerer, A. Cano, J. Hynynen, L. Yu, Y. Zhang, D. Nai, T. F. Harrelson, M. Sommer, A. J. Moulé, M. Kemerink, S. R. Marder, I. McCulloch, M. Fahlman, S. Fabiano and C. Müller, *Nat. Mater.*, 2019, **18**, 149–155.

13. P. Schmode, A. Savva, R. Kahl, D. Ohayon, F. Meichsner, O. Dolynchuk, T. Thurn-Albrecht, S. Inal and M. Thelakkat, *ACS Appl. Mater. Interfaces*, 2020, **12**, 13029–13039.

14. L. Q. Flagg, C. G. Bischak, J. W. Onorato, R. B. Rashid, C. K. Luscombe and D. S. Ginger, *J. Am. Chem. Soc.*, 2019, **141**, 4345–4354.

15. J. W. Onorato, Z. Wang, Y. Sun, C. Nowak, L. Q. Flagg, R. Li, B. X. Dong, L. J. Richter, F. A. Escobedo, P. F. Nealey, S. N. Patel and C. K. Luscombe, *J. Mater. Chem. A*, 2021, **9**, 21410–21423.

16. C. S. Haines, M. D. Lima, N. Li, G. M. Spinks, J. Foroughi, J. D. W. Madden, S. H. Kim, S. Fang, M. Jung de Andrade, F. Göktepe, Ö. Göktepe, S. M. Mirvakili, S. Naficy, X. Lepró, J. Oh, M. E. Kozlov, S. J. Kim, X. Xu, B. J. Swedlove, G. G. Wallace and R. H. Baughman, *Science*, 2014, **343**, 868–872.

17. S. T. Keene, C. Lubrano, S. Kazemzadeh, A. Melianas, Y. Tuchman, G. Polino, P. Scognamiglio, L. Cinà, A. Salleo, Y. van de Burgt and F. Santoro, *Nat. Mater.*, 2020, **19**, 969–973.

18. A. E. Javier, S. N. Patel, D. T. Hallinan, V. Srinivasan and N. P. Balsara, *Angew. Chemie Int. Ed.*, 2011, **50**, 9848–9851.

19. R. Noriega, J. Rivnay, K. Vandewal, F. P. V. Koch, N. Stingelin, P. Smith, M. F. Toney and A. Salleo, *Nat. Mater.*, 2013, **12**, 1038–1044.

20. S. A. Mollinger, B. A. Krajina, R. Noriega, A. Salleo and A. J. Spakowitz, *ACS Macro Lett.*, 2015, **4**, 708–712.

21. D. T. Duong, V. Ho, Z. Shang, S. Mollinger, S. C. B. Mannsfeld, J. Dacuña, M. F. Toney, R. Segalman and A. Salleo, *Adv. Funct. Mater.*, 2014, **24**, 4515–4521.

22. S. D. Kang and G. J. Snyder, *Nat. Mater.*, 2017, **16**, 252–257.

23. J. W. Onorato, Z. Wang, Y. Sun, C. Nowak, L. Q. Flagg, R. Li, B. X. Dong, L. J. Richter, F. A. Escobedo, P. F. Nealey, S. N. Patel and C. K. Luscombe, *J. Mater. Chem. A*, 2021, **9**, 21410–21423.

24. Z. Xue, D. He and X. Xie, *J. Mater. Chem. A*, 2015, **3**, 19218–19253.

25. K. Xu, *Chem. Rev.*, 2004, **104**, 4303–4418.

26. Y. Fu and A. Manthiram, *Chem. Mater.*, 2012, **24**, 3081–3087.

27. E. Zeglio, M. M. Schmidt, M. Thelakkat, R. Gabrielsson, N. Solin and O. Inganäs, *Chem. Mater.*, 2017, **29**, 4293–4300.

28. S. N. Patel, A. E. Javier, G. M. Stone, S. A. Mullin and N. P. Balsara, *ACS Nano*, 2012, **6**, 1589–1600.

29. A. E. Javier, S. N. Patel, D. T. Hallinan, V. Srinivasan and N. P. Balsara, *Angew. Chemie Int. Ed.*, 2011, **50**, 9848–9851.

30. C. Deslouis, T. El Moustafid, M. M. Musiani and B. Tribollet, *Electrochim. Acta*, 1996, **41**, 1343–1349.

31. E. D. Gomez, K. P. Barteau, H. Wang, M. F. Toney and Y. L. Loo, *Chem. Commun.*, 2011, **47**, 436–438.

32. G. Li, V. Shrotriya, Y. Yao and Y. Yang, *J. Appl. Phys.*, 2005, **98**, 1–6.

33. X. Yang, J. Loos, S. C. Veenstra, W. J. H. Verhees, M. M. Wienk, J. M. Kroon, M. A. J. Michels and R. A. J. Janssen, *Nano Lett.*, 2005, **5**, 579–583.

34. G. Dennler, M. C. Scharber and C. J. Brabec, *Adv. Mater.*, 2009, **21**, 1323–1338.

35. R. Xie, Y. Lee, M. P. Aplan, N. J. Caggiano, C. Müller, R. H. Colby and E. D. Gomez, *Macromolecules*, 2017, **50**, 5146–5154.

36. J. Clark, J.-F. Chang, F. C. Spano, R. H. Friend and C. Silva, *Appl. Phys. Lett.*, 2009, **94**, 163306.

37. C. Yang, Q. Wu, W. Xie, X. Zhang, A. Brozena, J. Zheng, M. N. Garaga, B. H. Ko, Y. Mao, S. He, Y. Gao, P. Wang, M. Tyagi, F. Jiao, R. Briber, P. Albertus, C. Wang, S. Greenbaum, Y. Y. Hu, A. Isogai, M. Winter, K. Xu, Y. Qi and L. Hu, *Nature*, 2021, **598**, 590–596.

38. H. Stutz, K.-H. Illers and J. Mertes, *J. Polym. Sci. Part B Polym. Phys.*, 1990, **28**, 1483–1498.

39. J. Nightingale, J. Wade, D. Moia, J. Nelson and J.-S. Kim, *J. Phys. Chem. C*, 2018, **122**, 29129–29140.

40. H. P. Klug and L. E. Alexander, *X-Ray Diffraction Procedures: For Polycrystalline and Amorphous Materials*, Wiley-VCH, 2nd edn., 1974.

41. D. Sharon, P. Bennington, C. Liu, Y. Kambe, B. X. Dong, V. F. Burnett, M. Dolejsi, G. Grocke, S. N. Patel and P. F. Nealey, *J. Electrochem. Soc.*, 2018, **165**, H1028–H1039.

42. C. Deng, M. A. Webb, P. Bennington, D. Sharon, P. F. Nealey, S. N. Patel and J. J. de Pablo, *Macromolecules*, 2021, **54**, 2266–2276.

43. B. X. Dong, J. Strzalka, Z. Jiang, H. Li, G. E. Stein and P. F. Green, *ACS Appl. Mater. Interfaces*, 2017, **9**, 44799–44810.